NanoSQUIDs for Studies on the Magnetization Reversal of Individual Magnetic Nanoparticles

Dissertation

der Mathematisch-Naturwissenschaftlichen Fakultät
der Eberhard Karls Universität Tübingen
zur Erlangung des Grades eines
Doktors der Naturwissenschaften
(Dr. rer. nat.)

vorgelegt von
Roman Wölbing
aus Leipzig

Tübingen
2015

Tag der mündlichen Prüfung:	21. April 2015
Dekan:	Prof. Dr. W. Rosenstiel
1. Berichterstatter:	Prof. Dr. R. Kleiner
2. Berichterstatter:	Prof. Dr. D. Kölle

Abstract

The subject of this thesis is the development, characterization and optimization of nanometer-sized superconducting quantum interference devices (nanoSQUIDs) for operation at cryogenic temperatures ($\sim 4\,\mathrm{K}$). This task is motivated by the need for convenient detectors for the investigation of individual magnetic nanoparticles, nanotubes, nanowires or molecular magnets. For this purpose the detectors need to withstand rather high magnetic fields, which are typically necessary to alter the magnetization of small spin systems. At the same time, the SQUIDs should feature ultra-high sensitivity with respect to magnetic flux with the ultimate goal of being able to detect the flipping of the spin of a single electron. These requirements can be satisfied by shrinking down the physical dimensions of the SQUID towards the nanoscale. On the one hand, the reduced loop size results in a much lower inductance and as a consequence thereof in an increased sensitivity. On the other hand, nanopatterning the SQUID minimizes the parasitic effects of the applied magnetic field. Two types of devices are considered in this thesis: (a) nanoSQUIDs based on Nb as a superconductor with Josephson junctions (JJs) having normal metal HfTi barriers and (b) nanoSQUIDs based on $YBa_2Cu_3O_7$ (YBCO) with grain boundary (GB) JJs.

Different designs of Nb nanoSQUIDs have been investigated in the past with remarkable success. In the first part of this work, an improved layout has been developed and studied with regard to high-field suitability and spin sensitivity. In this context it has been demonstrated that the Nb devices can be reliably operated in intermediate magnetic fields (around $100\,\mathrm{mT}$) with ultra-high spin sensitivity. With these findings, the Nb nanoSQUIDs could be even further improved and were successfully combined with cantilever torque magnetometry. This system allowed for detailed examinations on magnetic nanotubes, proving the huge potential of this kind of devices for the investigation of small spin systems.

Likewise, the YBCO nanoSQUIDs were investigated, showing flux and spin sensitivity comparable to conventional SQUIDs but in huge magnetic fields up to $1\,\mathrm{T}$.

In order to enhance the sensitivity, an optimization study was performed using numerical simulations based on London and Maxwell equations. It was shown that by choosing proper geometrical parameters, the YBCO nanoSQUIDs are indeed capable of detecting magnetic signals arising from a few Bohr magnetons. The corresponding devices were fabricated and the predicted properties could be confirmed. Finally, first magnetization reversal measurements on a Fe nanowire, encapsulated in a carbon nanotube, were performed.

Kurzfassung

Thema dieser Dissertation ist die Entwicklung, Charakterisierung und Optimierung von supraleitenden Quanteninterferometern mit Dimensionen auf der sub-μm Skala (nanoSQUIDs) für den Betrieb bei kryogenen Temperaturen ($\sim 4\,\mathrm{K}$). Die Arbeit ist motiviert durch den Mangel an geeigneten Detektoren für die Untersuchungen von individuellen magnetischen Nanopartikeln, Nanoröhrchen, Nanodrähten oder molekularen Magneten. Hierfür müssen die Detektoren recht hohen Magnetfeldern standhalten, die typischerweise nötig sind, um die Magnetisierung kleiner Spinsysteme zu beeinflussen. Gleichzeitig sollten die SQUIDs über eine enorme Empfindlichkeit hinsichtlich magnetischem Fluss verfügen, mit dem ultimativen Ziel, die Magnetisierungsumkehr eines einzelnen Elektronenspins zu detektieren. Durch Reduzierung der Abmessungen des SQUIDs auf die Nanometer-Skala können diese Anforderungen erfüllt werden. Zum Einen führt eine kleine Lochgröße zu einer kleinen Induktivität und damit auch zu einer erhöhten Empfindlichkeit, andererseits minimiert eine Nanostrukturierung der SQUIDs parasitäre Effekte durch ein angelegtes Magnetfeld. In dieser Dissertationsarbeit werden zwei Arten von Interferometern behandelt: (a) auf dem Supraleiter Nb basierende nanoSQUIDs mit Josephson Kontakten (JKs) mit normalleitenden Barrieren aus HfTi und (b) nanoSQUIDs aus $YBa_2Cu_3O_7$ (YBCO) mit Korngrenzenkontakten.

In der Vergangenheit wurden verschiedenen Entwürfe von Nb nanoSQUIDs mit großem Erfolg untersucht. Im ersten Teil dieser Arbeit wurde ein verbessertes Design hinsichtlich Hochfeldverträglichkeit und Spinempfindlichkeit entwickelt und analysiert. In diesem Zusammenhang konnte demonstriert werden, dass die Nb-Interferometer in mittelhohen Magnetfeldern (um $100\,\mathrm{mT}$) mit enorm hoher Spinempfindlichkeit stabil betrieben werden können. Aufbauend auf diesen Resultaten konnten die nanoSQUIDs noch einmal verbessert und erfolgreich mit cantilever torque Magnetometrie kombiniert werden. Dieses System ermöglicht detailierte Untersuchungen an magnetischen Nanoröhrchen, was das große Potential dieser Detektoren unterstreicht.

Gleichermaßen wurden YBCO nanoSQUIDs studiert, die selbst in sehr hohen Magnetfeldern bis hin zu 1 T eine Fluss- und Spinempfindlichkeit vergleichbar mit konventionellen SQUIDs zeigten. Um die Empfindlichkeit zu verbessern, wurde eine Optimierung mit Hilfe numerischer Methoden basierend auf London und Maxwell Gleichungen durchgeführt. Es konnte gezeigt werden, dass durch geeignete Wahl der geometrischen Parameter die YBCO nanoSQUIDs in der Tat in der Lage sind, magnetische Signale von einigen wenigen Bohr'schen Magneton aufzulösen. Die entsprechenden Interferometer wurden hergestellt und ihre vorhergesagten Eigenschaften konnten bestätigt werden. Abschließend wurden erste Messungen der Magnetisierungsumkehr eines mit einer Kohlenstoffnanoröhre ummantelten Eisen Nanodrahts durchgeführt.

List of publications

This is a cumulative thesis which is based on the publications listed below. The publications are attached at the very end of the thesis.

Appended Publications

.

Publication 1 **R. Wölbing**, J. Nagel, T. Schwarz, O. Kieler, T. Weimann, J. Kohlmann, A. B. Zorin, M. Kemmler, R. Kleiner and D. Koelle

Nb Nano Superconducting Quantum Interference Devices with High Spin Sensitivity for Operation in Magnetic Fields up to 0.5 T

Appl. Phys. Lett. **102**, 192601 (2013)

Publication 2 T. Schwarz, J. Nagel, **R. Wölbing**, M. Kemmler, R. Kleiner and D. Koelle

Low-Noise Nano Superconducting Quantum Interference Device Operating in Tesla Magnetic Fields

ACS Nano **7**, 844-850 (2013)

Publication 3 **R. Wölbing**, T. Schwarz, B. Müller, J. Nagel, M. Kemmler, R. Kleiner and D. Koelle

Optimizing the Spin Sensitivity of Grain Boundary Junction NanoSQUIDs - Towards Detection of Small Spin Systems with Single-Spin Resolution

Supercond. Sci. Technol. **27**, 125007 (2014)

Publication 4 T. Schwarz, **R. Wölbing**, C. F. Reiche, B. Müller, M. J. Martínez-Pérez, T. Mühl, B. Büchner, R. Kleiner and D. Koelle

Low-Noise $YBa_2Cu_3O_7$ Superconducting Quantum Interference Devices for Magnetization Reversal Measurements on Magnetic Nanoparticles

Phys. Rev. Applied **3**, 044011 (2014)

Publications not included in this thesis

Publication 5 J. Nagel, O. F. Kieler, T. Weimann, **R. Wölbing**, J. Kohlmann, A. B. Zorin, R. Kleiner, D. Koelle and M. Kemmler

Superconducting Quantum Interference Devices with Submicron Nb/HfTi/Nb Junctions for Investigation of Small Magnetic Particles

Appl. Phys. Lett. **90**, 032506 (2011)

Publication 6 D. Bothner, M. Knufinke, H. Hattermann, **R. Wölbing**, B. Ferdinand, P. Weiss, S. Bernon, J. Forágh, D. Koelle and R. Kleiner

Inductively Coupled Superconducting Half Wavelength Resonators as Persistent Current Traps for Ultracold Atoms

New J. Phys. **15**, 093024 (2013)

Contents

Chapter 1

Introduction

The fundamental interest in submicron magnetic systems, such as magnetic nanoparticles (NPs) [1], nanowires (NWs) [2], nanotubes (NTs) [3] or even single electrons [4], is driven by the desire to understand magnetism at the nanoscale and beyond [5–7]. In contrast to the well-known characteristics of macroscopic magnets, meso- and microscopic spin systems exhibit a whole range of novel features under convenient conditions [8, 9]. Fig. 1.1 schematically displays the situation. The hysteresis

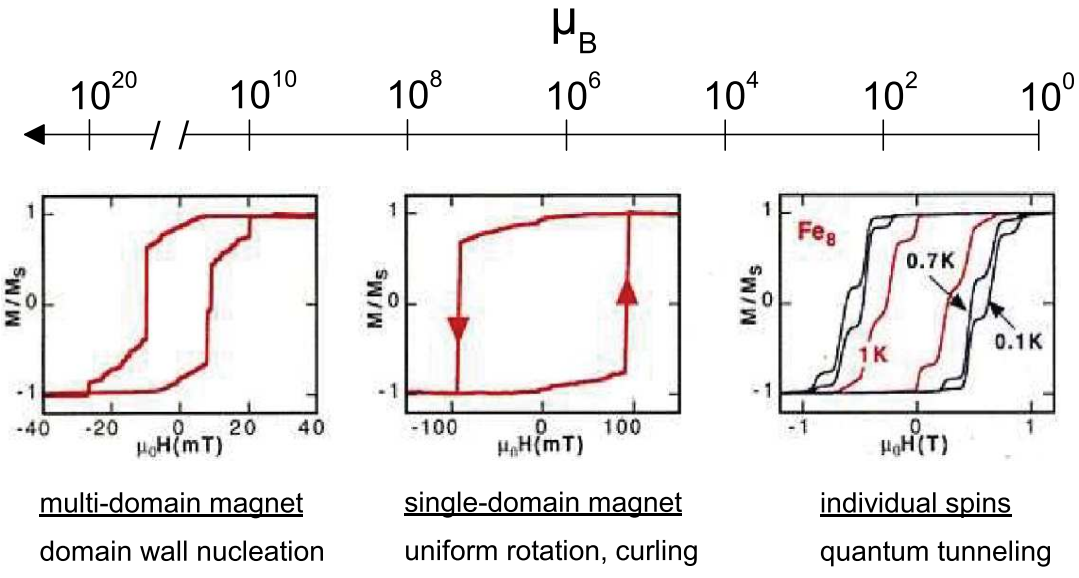

Figure 1.1: Illustration of macro-, meso and microscopic magnetic systems (from left to right). The scale represents the number of magnetic moments in units of Bohr magnetons. The hysteresis loops are characteristic for the respective size of the magnet. Figure adapted from [9].

loop to the left corresponds to a macroscopic magnet and shows the typical features of a system consisting of multiple magnetic domains separated by domain walls. If the size of the particle is reduced, the nucleation of domains becomes energetically unfavourable and the magnetization remains in a single-domain state; cf. hysteresis loop in the second graph of Fig. 1.1. In this regime, the magnetization reversal is dominated by rotation, curling or other more complex non uniform modes, depending e.g. on the exact shape of the particle. For even smaller spin systems, here Fe_8 molecular clusters, quantum mechanical effects emerge, e.g. resonant tunneling between discrete magnetic energy levels (Fig. 1.1; hysteresis loop to the right).

Particularly interesting regarding applications is the existence of a superparamagnetic state for NPs in the single-domain state with a typical diameter of $10 - 20\,\mathrm{nm}$ [10, 11]. Since an NP generally exhibits a huge (shape-)anisotropy, its magnetic moment is forced to align (anti-)parallel to the so called easy axis. The two states are separated by an energy barrier, which can be overcome by thermal excitation, resulting in a magnetization flip of the NP. For relatively high temperatures, the thermally induced flipping happens faster than the sampling rate of the measurement, which means that the NP has no net (average) magnetization and acts as a paramagnet. However, it retains the high saturation magnetization of a ferromagnet, thus giving rise to the designation "superparamagnetic". Below the blocking temperature T_B, the thermal flipping becomes much slower than the measurement time and the magnetization of the NP is "frozen". Fluids containing superparamagnetic NPs find different applications, e.g. as contrast agents in the field of medicine [12–18] or as shape shifting magnetic mirrors for earth-based telescopes [19, 20]. Furthermore, magnetic NPs are highly suitable for applications in the field of spintronics [21] and as high-density storage devices [22].

Several methods have been developed to examine the properties of magnetic NPs, e.g. magnetic resonance force microscopy [23], magneto-optic spin detection [24, 25] or scanning tunneling microscopy assisted electron spin resonance [26], since conventional methods are lacking of sensitivity. Compared to these techniques, the use of Superconducting Quantum Interference Devices (SQUIDs) [27] offers the advantage of directly detecting changes in magnetization by measuring the stray field of a single NP penetrating the SQUID loop. Also, SQUIDs constitute the most sensitive detectors for magnetic flux, which is why Wernsdorfer *et al.* proposed to use micrometer SQUIDs [9, 28] as detectors for small spin systems. In fact, it was predicted that by nanoscaling the devices, it is possible to detect single electron spin flips [29].

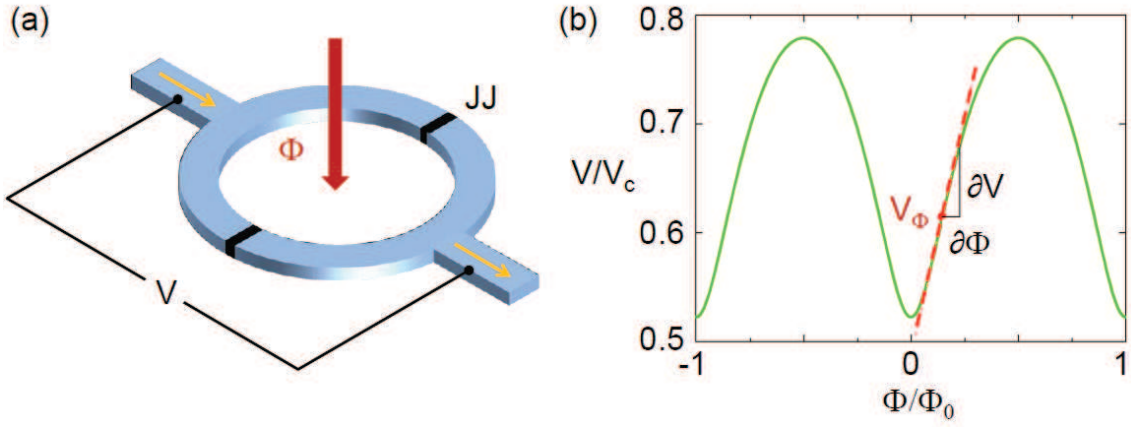

Figure 1.2: (a) Sketch of a dc SQUID. Josephson junctions (JJs) are indicated in black, superconductor in blue. (b) $V(\Phi)$-characteristic of a dc SQUID. The dotted red line marks the point of the steepest slope where the SQUID is usually operated.

In general, there are two types of SQUIDs: the direct durrent (dc) [30] and the radio frequency (rf) SQUID [31]. This thesis deals exclusively with the former one, which is sketched in Fig. 1.2 (a). The dc SQUID consists of a superconducting ring in which two Jospehson junctions (JJs) [32] are incorporated. For optimum performance, the device is usually biased at a current I_b slightly above the critical current I_c. Coupling magnetic flux Φ into the loop leads to a periodic modulation of the voltage drop V across the SQUID (Fig. 1.2 (b)). Here, voltage is normalized to the characteristic voltage $V_\mathrm{c} = I_\mathrm{c}R_\mathrm{N}$, with the normal resistance R_N of the device, and flux is normalized to the flux quantum Φ_0. Bias current and applied flux are adjusted to values where the slope of the $V(\Phi)$-characteristic is maximum, defined by the transfer function $V_\Phi = (\partial V/\partial\Phi)_\mathrm{max}$. In this way, the SQUID is operated at its resolution limit given by the spectral density of root mean square (rms) flux noise $S_\Phi^{1/2} = S_\mathrm{V}^{1/2}/|V_\Phi|$, where $S_\mathrm{V}^{1/2}$ is the spectral density of rms voltage noise. Typical values for conventional SQUIDs are around a few $\mu\Phi_0/\mathrm{Hz}^{1/2}$.

For investigations of small spin systems, SQUIDs need to be tailored to specific conditions [33–38]. We consider the scenario sketched in Fig. 1.3: A magnetic NP is placed near the SQUID loop and a magnetic bias field B is applied to alter its magnetization. Obviously, SQUID loop and bias field need to be parallel to each other, since one is only interested in signals arising from the stray field of the NP and not from the applied field. Nanoscaling the device minimizes the flux penetrating the SQUID and its JJs by a possible misalignment of B. At the same time, tailoring the linewidth w of the SQUID ring to submicron dimensions prevents the occurrence of Abrikosov vortices in the superconducting structures at high magnetic fields as

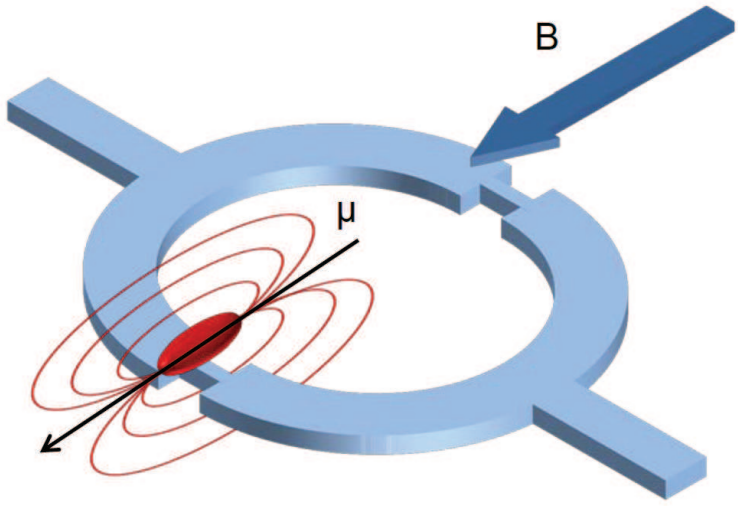

Figure 1.3: Sketch of a nanoSQUID with an attached magnetic NP. The loop contains a constriction where ϕ_μ is maximum for this specific orientation of $\vec{\mu}$.

a source of transients [39]. Furthermore, a reduced linewidth helps to achieve a sufficient coupling between NP and SQUID, described by the coupling factor $\phi_\mu = \Phi/|\vec{\mu}|$ [40]. Here, Φ is the flux coupled into the SQUID loop by the magnetic NP with magnetic moment $\vec{\mu}$. ϕ_μ strongly depends on the position of the NP with respect to the SQUID, the orientation of $\vec{\mu}$ and the SQUID layout. Considering Fig. 1.3, ϕ_μ decreases significantly if the magnetic moment of the NP is oriented perpendicular to the plane of the loop, for example. However, tailoring the device to the nanoscale is not just limited by technological constraints, but also by the kinetic inductance $L_{\mathrm{kin}} \propto 1/wd$ of the used superconducting material, with film thickness d [41]. If w and/or d drop well below the London penetration depth λ_{L}, the rise in kinetic inductance will lead to a reduced flux sensitivity, since $S_\Phi^{1/2} \propto \sqrt{L_{\mathrm{kin}}}$. At the end of the day, we can define a new figure of merit, the spin sensitivity $S_\mu^{1/2} = S_\Phi^{1/2}/\phi_\mu$, which gives the smallest amount of Bohr magnetons μ_{B} detectable for a given device and orientation of $\vec{\mu}$. While minimizing $S_\Phi \approx f(\beta_{\mathrm{L}}) k_{\mathrm{B}} T L \Phi_0 / V_{\mathrm{c}}$ [27], with Boltzmann constant k_{B} and screening parameter $\beta_{\mathrm{L}} = I_{\mathrm{c}} L/\Phi_0$, poses no basic difficulties, maximizing ϕ_μ is not straight forward, because it is rather hard to get experimental access to this quantity. By properly designing the SQUID geometry, inductances of only a few pH are achievable, and the use of high quality JJs yields characteristic voltages in the range of mV. By this means, the spectral density of rms flux noise can be reduced to well below $S_\Phi^{1/2} \leq 100\,\mathrm{n}\Phi_0/\mathrm{Hz}^{1/2}$ at $T = 4.2\,\mathrm{K}$. To optimize ϕ_μ, numerical methods have to be developed and applied to the specific SQUID layout, with the ultimate goal of achieving $S_\mu^{1/2} \approx 1\,\mu_{\mathrm{B}}/\mathrm{Hz}^{1/2}$.

In order to overcome the above mentioned obstacles, much effort has been invested in fabrication technology and nanoSQUID design over the last few years [28, 42, 44–57, 59–61]. Most groups back on constriction type JJs (cJJs) nanoSQUIDs, and although impressive results have been achieved with respect to flux noise, this design implicates several complications, see e.g. [45, 49, 54, 57]. First of all, cJJs often exhibit hysteretic current-voltage-characteristics (IVCs) which hampers a continuous operation of the device, being unfavorable for dynamic measurements of magnetization changes. Secondly, noise properties of cJJs are not well understood, making an optimization of $S_\Phi^{1/2}$ difficult. And finally, the cJJ is often denoted as the position of choice for a magnetic NP, however, in this way an optimization of ϕ_μ is impossible without affecting the junction properties and consequently $S_\Phi^{1/2}$. In one approach, it was demonstrated that nanoSQUIDs with extremely low film thickness of only a few nm can be operated in magnetic fields up to several Tesla [58]. The associated rise in kinetic inductance though leads to considerably less flux sensitivity. One of the most promising designs is the SQUID-on-tip (SOT), which was the first to achieve single electron spin flip sensitivity [59–61]. Here, the devices are fabricated by shadow evaporation on a quartz tip with apex diameters down to 50 nm. Spin sensitivities below $1\,\mu_\mathrm{B}/\mathrm{Hz}^{1/2}$ were calculated, even in fields up to 1 T. The major drawback to this design is that the nanoSQUIDs can not be feedbacked to retain the optimum working point of the $V(\Phi)$-characteristic.

Subject to this thesis is the development and optimization of nanoSQUIDs based on alternative JJ types as well as their application to investigate small spin systems. The focus is on suitable designs, high spin sensitivity and stable operation in rather high magnetic fields. To meet these challenges, two types of nanoSQUIDs based on different superconductors and JJs were utilized.

Fig. 1.4 (a) shows a sketch of the nanoSQUIDs based on Nb/HfTi/Nb superconductor/normal metal/superconductor (SNS) JJs [62–65], which were fabricated by the Physikalisch Technische Bundesanstalt (PTB) in Braunschweig [66, 67]. By applying electron beam lithography, devices with loop sizes down to $600 \times 220\,\mathrm{nm}^2$ and linewidths of 250 nm could be realized. The JJs (indicated in yellow in Fig. 1.4 (a)) are square shaped with an area of $200 \times 200\,\mathrm{nm}^2$ and HfTi thickness of ≈ 25 nm. The main advantage of the usage of normal metal barriers is a high critical current density of $j_0 \approx 10^5\,\mathrm{kA/cm}^2$ which yields sufficiently large values of I_c even for submicron JJs. At the same time, the JJs are intrinsically shunted, i.e. show non-hysteretic IVCs even without bulky shunt-resistors. Implemented within the nanoSQUID is a "coil-on-chip" to avoid a possible noise source by an external

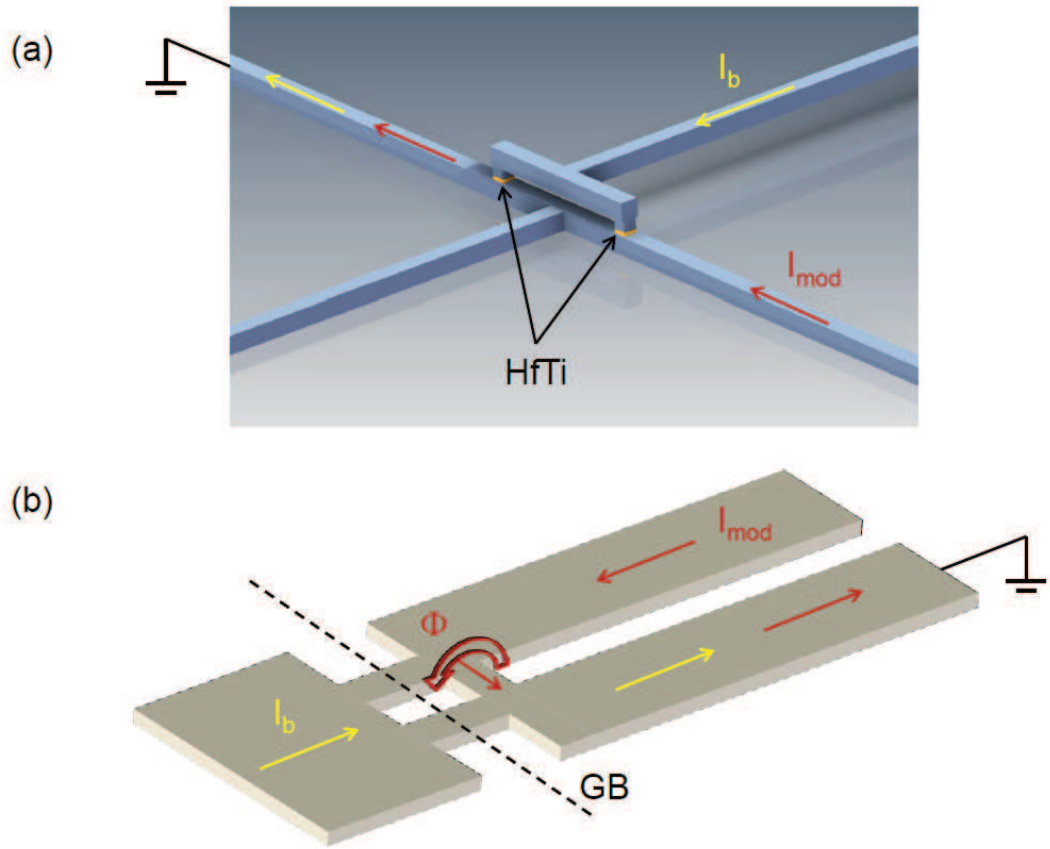

Figure 1.4: (a) Layout of Nb nanoSQUID (not so scale). Blue areas indicate Nb and yellow areas JJs with HfTi barriers. Arrows show paths for bias current I_b (yellow) and modulation current I_{mod} (red). (b) Layout of the YBCO nanoSQUID (not to scale). The black dashed line denotes the grain boundary. Intersections with the YBCO film (grey) give positions of the JJs.

coil. Passing a modulation current I_{mod} through the bottom electrode results in magnetic flux Φ coupling into the loop. Also, this feature enables flux locked loop (FLL) operation, to keep the device at the optimum working point during measurements. Due to the sandwich geometry, a magnetic bias field can be applied parallel to the loop (perpendicular to the HfTi layer) without coupling any flux into the SQUID or the JJs.

Fig. 1.4 (b) schematically sketches the layout of the $YB_2Cu_3O_7$ (YBCO) nanoSQUIDs [68], which are nanopatterned by focused ion beam (FIB) milling [69–71]. In contrast to the Nb nanoSQUIDs, these devices are based on a planar geometry, which involves only a single superconducting layer. The black dashed line in Fig. 1.4 (b) indicates a grain boundary (GB) intersecting the (grey) YBCO bridges to form two GBJJs. Since the weak links tend to have a hysteretic IVC at

$T = 4.2\,\mathrm{K}$, an Au film is evaporated on top of the YBCO, acting as a resistive shunt and as a protective layer. As for the Nb devices, the YBCO nanoSQUIDs feature a coil-on-chip for flux-biasing. A magnetic bias field can be applied parallel to the surface perpendicular to the GB without inducing any signals in the SQUID. Regarding the physical dimensions of the YBCO devices, loop sizes of down to $350 \times 190\,\mathrm{nm}^2$ and linewidths down to $\approx 80\,\mathrm{nm}$ were achieved.

Table 1.1 summarizes a few important properties for both types of nanoSQUIDs.

properties			Nb	YBCO
barrier type			normal metal	insulator
geometry			trilayer	monolayer
durability			stable	degrading
critical temperature	T_c	[K]	9.2	92
upper critical field	B_{c2}	[T]	1	30
critical current density	j_0	[A/cm^2]	10^5	10^5

Table 1.1: Properties of the Nb and YBCO nanoSQUIDs. T_c and B_{c2} is the temperature and magnetic field, respectively, above which the superconductive state collapses. Values for j_0 are for $T = 4.2\,\mathrm{K}$.

In the following chapter 2 publications regarding Nb and YBCO nanoSQUIDs are summarized. Publication 1 deals with the characterization of Nb nanoSQUIDs as well as with their noise properties in shielded and unshielded high-field environments. In Publication 2 we discuss the same issues with respect to the YBCO nanoSQUIDs. An optimization study for the YBCO nanoSQUIDs with the goal of single electron spin flip sensitivity is presented in Publication 3. In Publication 4, we use these results to fabricate the according devices and demonstrate first measurements on small spin systems.

In chapter 3 we present measurements on magnetic NTs performed simultaneously with nanoSQUID and cantilever torque magnetometry.

Chapter 2

Summary of Publications

2.1 Summary of Publication 1:

Nb Nano Superconducting Quantum Interference Devices with High Spin Sensitivity for Operation in Magnetic fields up to 0.5 T

Subject of the presented study are two Nb nanoSQUIDs which were investigated at $T = 4.2\,\mathrm{K}$ with respect to noise and high-field suitability. The devices were fabricated by the PTB in Braunschweig by using electron beam lithography and argon ion milling [66, 67]. The layout is schematically depicted in Fig. 2.1 (a); (b) shows a scanning electron microscopy (SEM) image. The samples are based on a trilayer geometry with Nb/HfTi/Nb SNS type JJs. In contrast to conventional $\mathrm{Nb/Al-AlO_x/Nb}$ [72] or constriction type weak links, these junctions are intrinsically shunted and have very high critical current densities. Compared to early works [62], the SQUIDs have a microstrip-like geometry, i.e. the plane of the SQUID loop is perpendicular to the plane of the substrate. In this configuration, a magnetic bias field can be applied parallel to the SQUID loop without suppressing the critical current of the junctions. Furthermore, the bottom electrode can be used to apply a modulation current I_{mod} to flux bias the device at its optimum working point without the need of an external coil.

All data were taken at $T = 4.2\,\mathrm{K}$. Electrical transport measurements exhibit non-hysteretic IVCs and characteristic voltages of $V_{\mathrm{c}} = 50\,\mu\mathrm{V}$. By applying magnetic flux to the SQUID loop via the modulation current I_{mod}, we recorded the critical

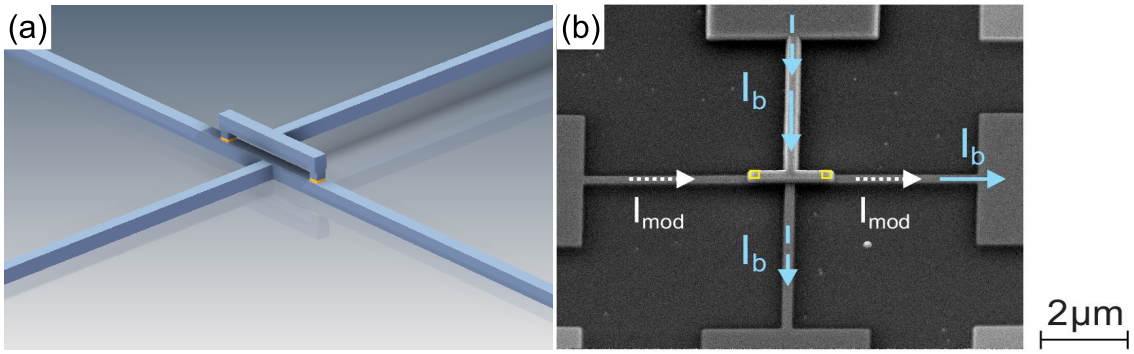

Figure 2.1: (a) Sketch of the Nb nanoSQUID. Blue areas indicate the Nb strips and yellow areas JJs with HfTi barriers (not to scale). (b) SEM image of the Nb nanoSQUID. Yellow rectangles indicate size and positions of the JJs. Arrows indicate current paths for the bias current I_b (dashed: symmetric bias; solid: asymmetric bias) and for the modulation current I_mod. Figure adapted from appended Publication 1. © American Physical Society.

current I_c as a function of $\Phi \propto I_\mathrm{mod}$. From the I_c modulation depth we derived a screening parameter of $\beta_\mathrm{L} \approx 0.2$, equivalent to a very low inductance of $L \approx 2.5\,\mathrm{pH}$. Since $S_\Phi^{1/2} \propto \sqrt{L/V_\mathrm{c}}$, we therefore expected extremely low values of the spectral density of rms flux noise for both devices. To verify this assumption we conducted noise measurement in an electrically and magnetically shielded environment using a cryogenic amplifier in a two stage configuration [73] instead of a room-temperature amplifier as for the transport measurements. The nanoSQUIDs were flux-biased in the voltage state at the optimum working point, i.e. at $V_\Phi = (\partial V/\partial\Phi)_\mathrm{max}$. The obtained spectra show a distinctive $1/f$-like noise right up to the cut-off frequency of the electronics, which hampers to make a statement about $S_\Phi^{1/2}$ in the white (frequency independent) noise limit. By fitting the experimental data to $S_\Phi^{1/2}(f) \propto S_{\Phi,\mathrm{w}}^{1/2} + 1/f^{1/2}$, we find $S_{\Phi,\mathrm{w}}^{1/2} = 200\,\mathrm{n}\Phi_0/\mathrm{Hz}^{1/2}$.

To determine the spin sensitivity for the Nb nanoSQUIDs we use a numerical procedure which is described in detail in Publication 2, see also [69, 71, 74]. For a point-like magnetic particle with its magnetic moment $\vec{\mu}$ oriented perpendicular to the plane of the substrate with a distance of 10 nm to the SQUID loop, we find a coupling factor of $\phi_\mu = 8.6\,\mathrm{n}\Phi_0/\mu_\mathrm{B}$. This corresponds to a spin sensitivity of $S_\mu^{1/2} = S_{\Phi,\mathrm{w}}^{1/2}/\phi_\mu = 23\,\mu_\mathrm{B}/\mathrm{Hz}^{1/2}$.

For measurements on magnetic NPs, the nanoSQUIDs should withstand an applied bias field which alters the magnetization of such a small spin system. Therefore, in the second part of Publication 1, we investigate the nanoSQUIDs in an unshielded high-field environment. The setup is equipped with a superconducting split coil

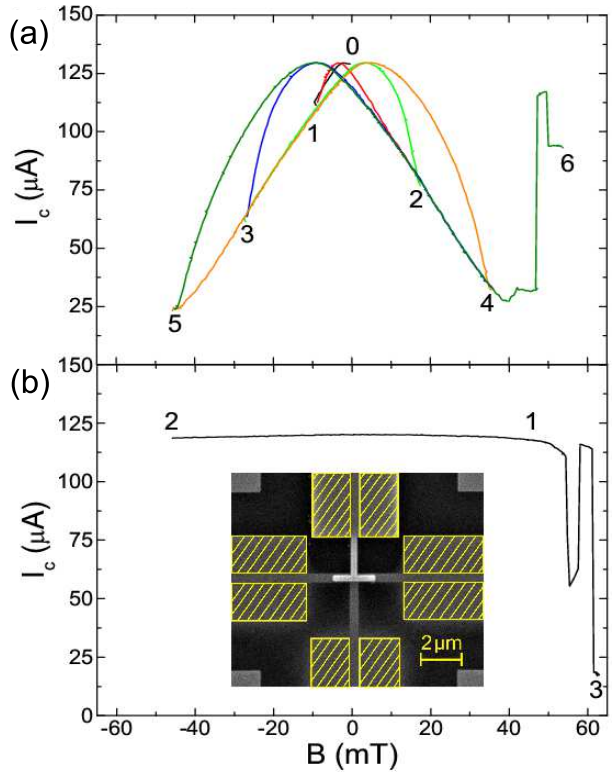

Figure 2.2:
(a) Critical current I_c vs applied field B measurement for field sweep sequence 0 mT → −9 mT → 18 mT → −27 mT → 36 mT → −45 mT → 54 mT (0-6). The steep jump at $B \approx 45$ mT can be assigned to an Abrikosov vortex entering the Nb leads close to the SQUID loop.
(b) $I_c(B)$ measurement for field sweep sequence 46 mT → −46 mT → 64 mT (1-3) after removing Nb areas by FIB milling as indicated by the yellow hatched rectangles in the SEM image in the inset. The steep jumps at $B \geq 50$ mT signal vortex(-motion) in the Nb leads. Figure from appended Pulication 1. © American Physical Society.

magnet and an alignment system for the SQUID consisting of a rotator and two goniometers with perpendicular tilt axes. By aligning the bias field parallel to the plane of the SQUID loop, no flux should penetrate either the loop nor the JJs. Measurements of the critical current I_c as a function of the applied bias field B exhibit a hysteresis-like behaviour (Fig. 2.2 (a)), which can be assigned to the penetration of Abrikosov vortices in the wider superconducting structures. The effect is eliminated by reducing the linewidth of the connection lines of the SQUID by FIB milling (Fig. 2.2 (b)).

These findings were implemented into the second generation Nb nanoSQUIDs, i.e. the linewidth of the connection lines were significantly reduced in the fabrication process. By repeating the measurements (Fig. 2.3 (a)), we demonstrate a stable operation in a field interval of ±50 mT with minor decrease of I_c. For larger magnetic fields, vortices enter the narrow connection lines close to the SQUID loop, as confirmed in [64]. Noise measurements for different applied fields show only a slight increase in rms flux noise in the white noise limit ($S_{\Phi,\mathrm{w}}^{1/2} \approx 240\,\mathrm{n}\Phi_0/\mathrm{Hz}^{1/2}$) (inset of Fig. 2.3 (a)). Furthermore, we show that even for fields much larger than 50 mT the nanoSQUIDs can still be operated with remarkable sensitivity of $S_{\Phi,\mathrm{w}}^{1/2} \approx 680\,\mathrm{n}\Phi_0/\mathrm{Hz}^{1/2}$ (Fig. 2.3 (b)). Assuming that ϕ_μ is independent of the applied field, we calculate spin sensitivities of $S_\mu^{1/2}(B \leq |50\,\mathrm{mT}|) \leq 29\,\mu_\mathrm{B}/\mathrm{Hz}^{1/2}$ and

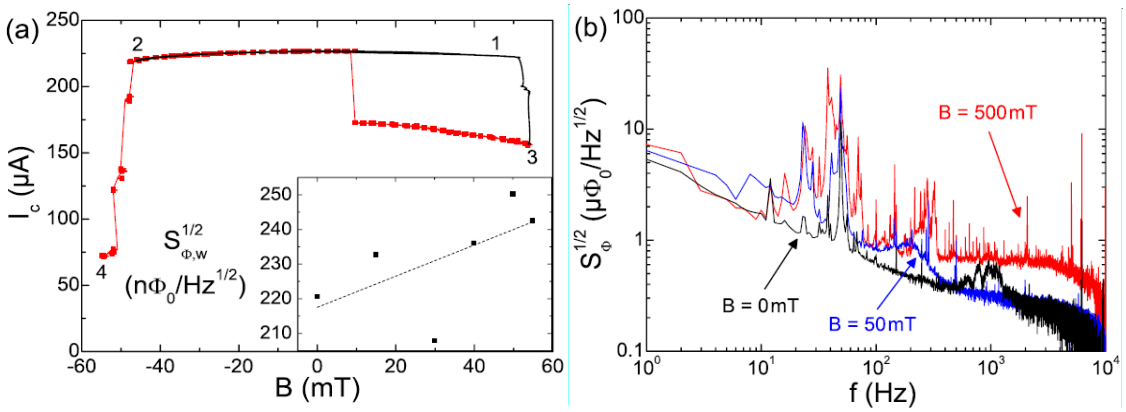

Figure 2.3: (a) Critical current I_c vs applied field B measurement for field sweep sequence 46 mT $\rightarrow$ -46 mT $\rightarrow$ 55 mT (1-3; black solid line) and 55 mT $\rightarrow$ -55 mT (3-4; red dotted line). Steep jumps at field values $B = \pm 50$ mT indicate Abrikosov vortices in the superconducting structures. The jump at $B \approx 10$ mT can be assigned to a vortex escape. Inset shows spectral density of rms flux noise in the white noise regime $S^{1/2}_{\Phi,\mathrm{w}}$ for different field values; dashed line is a linear fit. (b) Spectral density of rms flux noise $S^{1/2}_{\Phi}(f)$ for $B = 0\,\mathrm{mT}, 50\,\mathrm{mT}, 500\,\mathrm{mT}$. Figure from appended Publication 1. © American Physical Society.

$S^{1/2}_{\mu}(B = 0.5\,\mathrm{T}) \approx 79\,\mu_\mathrm{B}/\mathrm{Hz}^{1/2}$.

In summary we could demonstrate that Nb nanoSQUIDs based on SNS type JJs are suitable for the detection and investigation of small spin systems. The devices show a very high flux and spin sensitivity in shielded low-field environments as well as in relatively high magnetic fields up to 0.5 T.

Contributions

Publication 1 was done in collaboration with the group of J. Kohlmann and A. W. Zorin of the PTB in Braunschweig. The samples were fabricated by O. Kieler and T. Weimann. For this work I conducted the transport characterization of the nanoSQUIDs, as well as the low- and high-field measurements. T. Schwarz did the FIB milling procedure to reduce the linewidth of the connection lines of the nanoSQUIDs to achieve an improved high-field performance. J. Nagel assisted with the measurements and developed the sample design, while M. Kemmler supported the interpretation of the results.

2.2 Summary of Publication 2:

Low-Noise Nano Superconducting Quantum Interference Device Operating in Tesla Magnetic Fields

The nanoSQUID presented in Publication 2 is based on the superconductor YBCO. The fabrication was done as described in [69] in Tübingen. A YBCO film of thickness $d_{\mathrm{YBCO}} = 50\,\mathrm{nm}$ is grown epitaxially on an $SrTiO_3$ (STO) bicrystal substrate with a 24° misorientation GB. In this way the misorientation of the substrate is transferred to the YBCO film forming a GBJJ. To provide a non-hysteretic behaviour of the weak link, a $d_{\mathrm{Au}} = 60\,\mathrm{nm}$ gold layer is evaporated on top of the YBCO film, serving as a shunt resistor. In addition, the Au acts as a protective layer against the following fabrication processes. $7\,\mu$m wide bridges were patterned across the GBJJ by optical lithography and Ar ion milling. In the final process step, the nanoSQUID was patterned by FIB milling as depicted in Fig. 2.4.

The two junctions have a width of $w_{\mathrm{J}} = 130\,\mathrm{nm}$ and the SQUID loop has dimensions of $300\,\mathrm{nm} \times 400\,\mathrm{nm}$. Additionally, a constriction close to the SQUID loop was patterned, which allows to apply a modulation current I_{mod} coupling magnetic flux into the loop. In this way it is possible to flux bias the device without the need of an external coil, similar to the Nb nanoSQUIDs in Publication 1. Also, numerical simulations of the coupling factor ϕ_μ have shown that the constriction constitutes

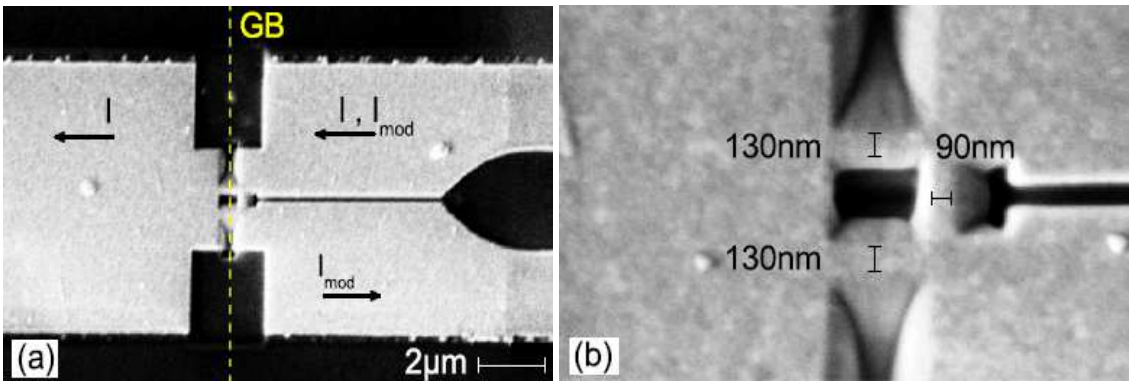

Figure 2.4: SEM images of the YBCO nanoSQUID. (a) Overall view with the directions of bias (I_{b}) and modulation current (I_{mod}) shown as arrows. The GB is indicated by the yellow dashed line. In (b), the physical dimensions of the most narrow sections are shown. Figure from appended Publication 2. © American Chemical Society.

the optimum position for a magnetic NP [71]. Since JJs and place of optimum coupling are separated from each other, this design allows for the optimization of junction properties and ϕ_μ independently.

The characterization of the YBCO SQUID is done at $T = 4.2\,\mathrm{K}$. Low field transport measurements conducted in a electrically and magnetically shielded environment yield a characteristic voltage $V_\mathrm{c} = 130\,\mu\mathrm{V}$. From the modulation depth of the $I_\mathrm{c}(I_\mathrm{mod})$-measurement, we calculate the inductance of the nanoSQUID to $L = 36\,\mathrm{pH}$. This quite large value for L, as compared to the Nb nanoSQUIDs presented in Publication 1, can be explained by the kinetic inductance L_kin contribution. Since $\lambda_\mathrm{L} \approx 250\,\mathrm{nm}$ for YBCO is significantly larger than $d_\mathrm{YBCO} = 50\,\mathrm{nm}$ and $w_\mathrm{J} = 130\,\mathrm{nm}$, we expect L_kin to be the dominant contribution to L instead of the geometric inductance.

To demonstrate the high-field suitability of the YBCO SQUID, the device was mounted in the high-field setup, as described in the summary of Publication 1. In contrast to the Nb nanoSQUIDs, now the applied field needs to be oriented along the plane of the substrate perpendicular to the JJs to avoid suppression of I_c. Even in magnetic fields up to $B = 3\,\mathrm{T}$ the sample can be operated with only a slight reduction of I_c. Noise measurements are conducted in the high-field setup using a cryogenic amplifier. Fig. 2.5 shows the obtained spectra for zero field and in an

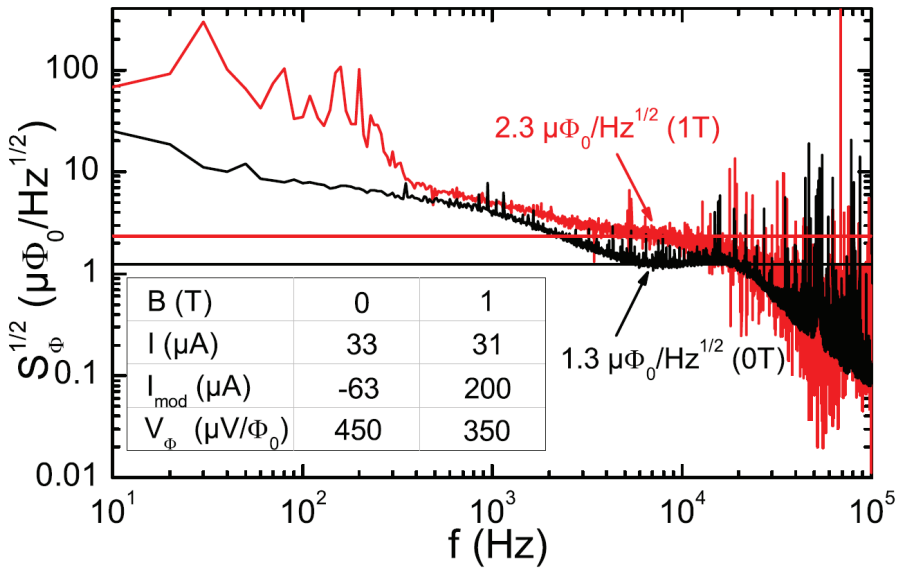

Figure 2.5: Rms spectral density of flux noise $S_\Phi^{1/2}(f)$ in $B = 0$ (black) and $B = 1\,\mathrm{T}$ (red) for the YBCO nanoSQUID. Table gives characteristic parameters. Figure from appended Publication 2. © American Chemical Society.

applied field of $B = 1\,\mathrm{T}$.

For $B = 0$ we find an rms spectral density of flux noise in the white noise limit of $S_{\Phi,\mathrm{w}}^{1/2} = 1.3\,\mu\Phi_0/\mathrm{Hz}^{1/2}$. Also, we find a distinctive $1/f$-like noise for low frequencies, which we attribute to critical current fluctuations in the grain boundary junctions [75]. The relatively high flux noise values can partially be explained by the large kinetic inductance of the device. At fields of $B = 1\,\mathrm{T}$ we find $S_{\Phi,\mathrm{w}}^{1/2} = 2.3\,\mu\Phi_0/\mathrm{Hz}^{1/2}$ and also an increase of the $1/f$-noise. This rise in flux noise can be associated to a minor misalignment inducing vortices in the superconducting structures.

Calculations of the coupling factor are shown in Fig. 2.6 and were performed as in [63]. For a point-like magnetic particle with its magnetic moment oriented along the x-axis positioned 10 nm above the constriction (disregarding the Au layer; cf.

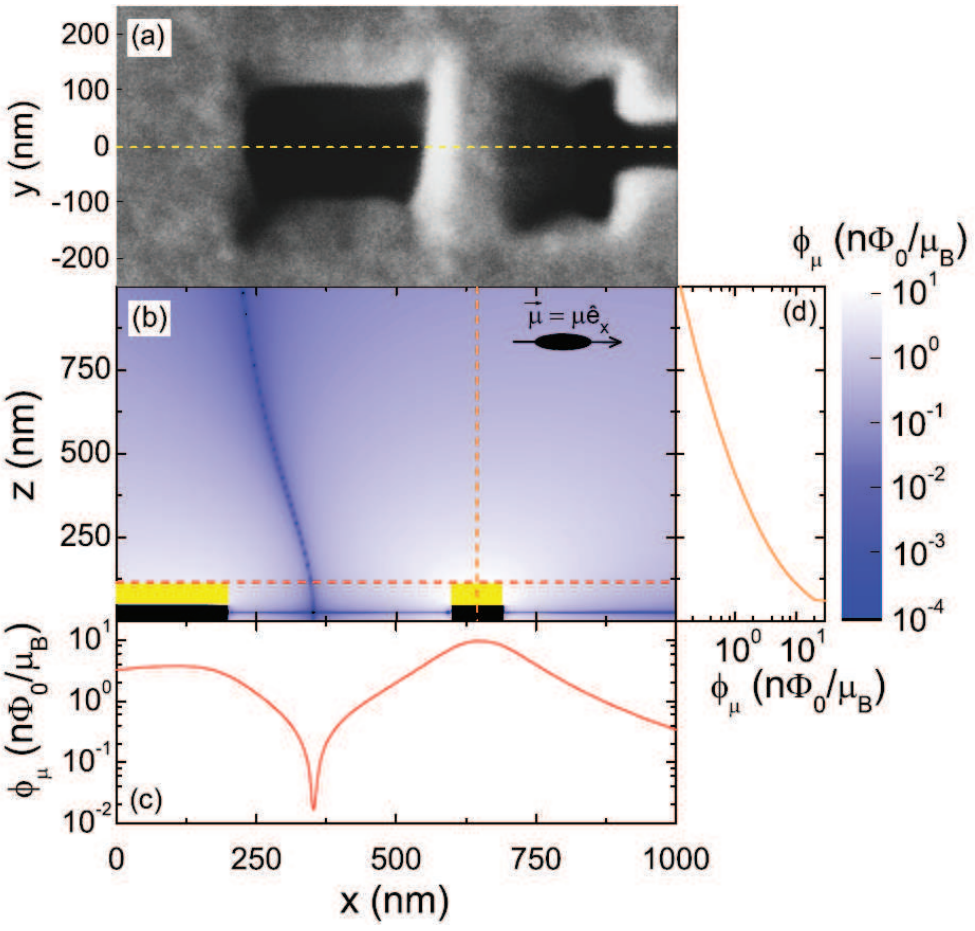

Figure 2.6: Numerical simulation of ϕ_μ. (a) SEM image of the YBCO nanoSQUID. (b) Contourplot $\phi_\mu(x, z)$ for $y = 0$ as indicated by the yellow dashed line in (a). Black areas indicate YBCO and yellow areas Au. (c) and (d) show $\phi_\mu(x)$ and $\phi_\mu(z)$ linescans, respectively, for the red dashed lines in (b). Figure from appended Publication 2. © American Chemical Society.

Fig. 2.6 (b)), we find $\phi_\mu = 21\,\mathrm{n}\Phi_0/\mu_\mathrm{B}$ which corresponds to a spin sensitivity of $S_\mu^{1/2} = S_{\Phi,\mathrm{w}}^{1/2}/\phi_\mu = 62\,\mu_\mathrm{B}/\mathrm{Hz}^{1/2}$ in zero field and $S_\mu^{1/2} = 121\,\mu_\mathrm{B}/\mathrm{Hz}^{1/2}$ at $B = 1\,\mathrm{T}$. As can be seen from Fig. 2.6 (c), the very narrow constriction provides a much higher coupling factor as compared to the area on the left side of the SQUID loop. Fig. 2.6 (d) displays $\phi_\mu(z)$. Here, the main finding is that indeed ϕ_μ can be increased by a factor of 2 by removing the Au layer above the constriction. However, it remains to be shown whether or not this affects the electrical properties of the nanoSQUID.

In summary, we demonstrated that our YBCO nanoSQUIDs have a very high sensitivity regarding flux and spin and can reliably be operated in huge magnetic fields up to at least $B = 1\,\mathrm{T}$. Therefore, the devices are the first choice for the detection of very small magnetic NPs.

Contributions

T. Schwarz fabricated the nanoSQUID and performed the measurements and data analysis. J. Nagel built the high-field setup, developed the sample design and assisted with the measurements. M. Kemmler also assisted with the measurements. I did the numerical simulations of the coupling factor and helped optimizing the high-field setup.

2.3 Summary of Publication 3:

Optimizing the Spin Sensitivity of Grain Boundary Junction NanoSQUIDs - Towards Detection of Small Spin Systems with Single-Spin Resolution

To further improve the performance of the YBCO nanoSQUIDs as designed in Publication 2, we conducted an optimization study with the goal of significantly enhancing the spin sensitivity $S_\mu^{1/2} = S_\Phi^{1/2}/\phi_\mu$. Obviously, this can be done via reducing the spectral density of flux noise $S_\Phi^{1/2}$ and via increasing the coupling factor ϕ_μ. Since $S_\Phi^{1/2} \propto \sqrt{L}$, the spin sensitivity can be improved by further minimizing the SQUID loop and linewidths. However, this reduction is not only limited by technological constraints but also by the kinetic inductance L_{kin} of the used superconducting material, which scales inversely with film thickness d and linewidth w. To achieve a high value of ϕ_μ, i.e. a sufficient coupling between nanoSQUID and a particle with magnetic moment $\vec{\mu}$, the nanomagnet needs to be placed on a narrow constriction inserted in the SQUID loop. For the design of the YBCO nanoSQUIDs, the position of ideal coupling is separated from the grain boundary junctions, allowing for an independent optimization for $S_\Phi^{1/2}$ and ϕ_μ.

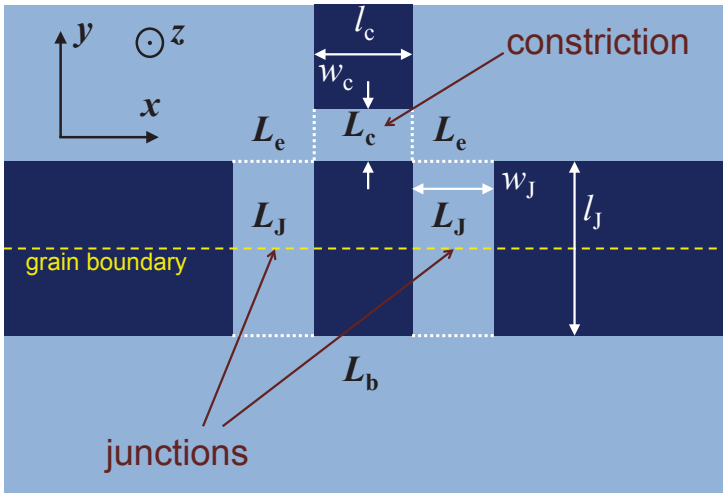

Figure 2.7: Sketch of the YBCO nanoSQUID. Lower-case characters indicate geometric parameters: constriction length l_c and width w_c and junction length l_J and width w_J. Capital L indicates inductance of: constriction L_c, junction L_J, edge L_e and bottom part of the SQUID L_b. Yellow dashed line shows position of the grain boundary. Figure from appended Publication 3. © Institute of Physics and IOP Publishing.

First, we numerically calculate the coupling factor between the nanoSQUID and a magnetic moment $\vec{\mu}$ using three different methods within the software package 3D-MLSI [74]. A detailed description is given in Appendix A of this thesis. The program is based on Maxwell and London equations and takes into account the geometry of the SQUID (Fig. 2.7). For all methods we consider a magnetic particle positioned 10 nm above the center of the constriction, i.e. at $w_c/2$ and $l_c/2$. Method 1 is similar as in [69]: we consider a virtual point-like magnetic moment $\vec{\mu} = \mu\widehat{e}_\mu$ close to the SQUID geometry and calculate the magnetic field distribution $\vec{B}(\vec{r})$ arising from the screening currents J within the SQUID. The coupling factor is obtained by $\phi_\mu(\vec{r}, \widehat{e}_\mu) = \widehat{e}_\mu \cdot \vec{B}(\vec{r})/J$. In methods 2 and 3 we consider two superconducting strips imitating a magnetic dipole with one Bohr magneton. For the boundary condition in method 2 we demand the net current around the SQUID loop to be zero, i.e. we consider ideal flux focussing. By calculating the fluxoid Φ_{fluxoid} induced in the SQUID by the stray field of the particle, we obtain $\phi_\mu = \Phi_{\text{fluxoid}}/\mu_B$. In contrast, in method 3 we demand the fluxoid in the SQUID loop to be zero, i.e. we consider ideal flux screening. Here, we obtain the coupling factor $\phi_\mu = LJ/\mu_B$ by calculating the inductance L and the screening current J. All methods yield identical results $\phi_\mu(d, w_c)$, verifying the calculations of the coupling factor in previous works.

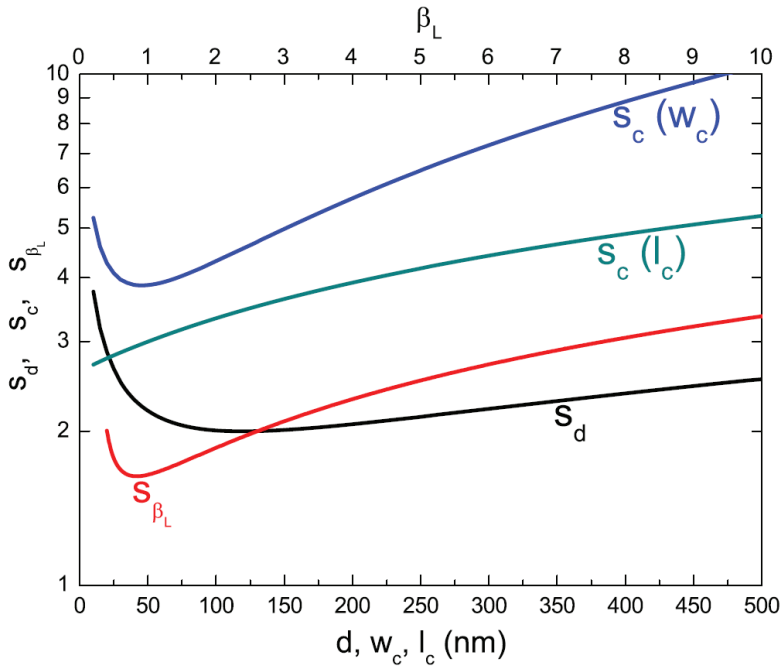

Figure 2.8: Contributions to calculated spin sensitivity $S_\mu^{1/2}$. $s_c(w_c)$ is plotted for $l_c = 200$ nm, $s_c(l_c)$ for $w_c = 60$ nm and $s_{\beta_L}(\beta_L)$ for $\kappa = 0.26$. Figure from appended Publication 3. © Institute of Physics and IOP Publishing.

In the next step, we optimize the spectral density of flux noise by using the relation $S_\Phi = f(\beta_\mathrm{L})\Phi_0 k_\mathrm{B} T L/I_0 R$ with $f(\beta_\mathrm{L}) = 4(1+\beta_\mathrm{L})$ and $\beta_\mathrm{L} = 2I_0 L/\Phi_0$. We fix the critical voltage to $I_0 R = 0.5\,\mathrm{mV}$ and calculate the inductance $L(d, w_\mathrm{c}, l_\mathrm{c}, w_\mathrm{J}, l_\mathrm{J})$ as a function of all relevant geometric parameters, which yields $S_\Phi^{1/2}(d, w_\mathrm{c}, \beta_\mathrm{L})$.

With the terms for $\phi_\mu(d, w_\mathrm{c})$ and $S_\Phi^{1/2}(d, w_\mathrm{c}, \beta_\mathrm{L})$, we now are able to give an analytical expression for $S_\mu^{1/2}$, which splits into three independent parts:

$$S_\mu^{1/2} = S_{\mu,0}^{1/2} s_\mathrm{d}(d) s_{\beta_\mathrm{L}}(\beta_\mathrm{L}) s_\mathrm{c}(w_\mathrm{c}, l_\mathrm{c})$$

The three contributions are plotted in Fig. 2.8, while $s_\mathrm{c}(w_\mathrm{c}, l_\mathrm{c})$ has been split into $s_\mathrm{c}(w_\mathrm{c})$ and $s_\mathrm{c}(l_\mathrm{c})$. $s_\mathrm{d}(d)$ shows a shallow minimum around $d \approx 120\,\mathrm{nm}$. For thicker films the decrease of the coupling factor seems to counterbalance the decrease in kinetic inductance. $s_{\beta_\mathrm{L}}(\beta_\mathrm{L})$ shows a clear minimum at $\beta_\mathrm{L,min} \approx 0.83$. However, it becomes apparent that $s_{\beta_\mathrm{L}}(\beta_\mathrm{L})$ is also a function of $\kappa \propto (l_\mathrm{J} + l_\mathrm{c}) j_0$. The evaluation of $s_{\beta_\mathrm{L}}(\beta_\mathrm{L})$ yields $\beta_\mathrm{L,opt} = 0.4$ for $\kappa \approx 0.09$, which gives a relation between the optimum junction length $l_\mathrm{J,opt}$ and constriction length l_c. Thus, the choice of l_c fixes $l_\mathrm{J,opt}$. Finally, the contributions $s_\mathrm{c}(l_\mathrm{c})$ and $s_\mathrm{c}(w_\mathrm{c})$ depend on each other. $s_\mathrm{c}(l_\mathrm{c})$ yields a monotonic decrease, while $s_\mathrm{c}(w_\mathrm{c})$ shows a clear minimum. Position and value depend on l_c; a detailed analysis shows that l_c should be as small as possible, which then determines the optimum choice for w_c.

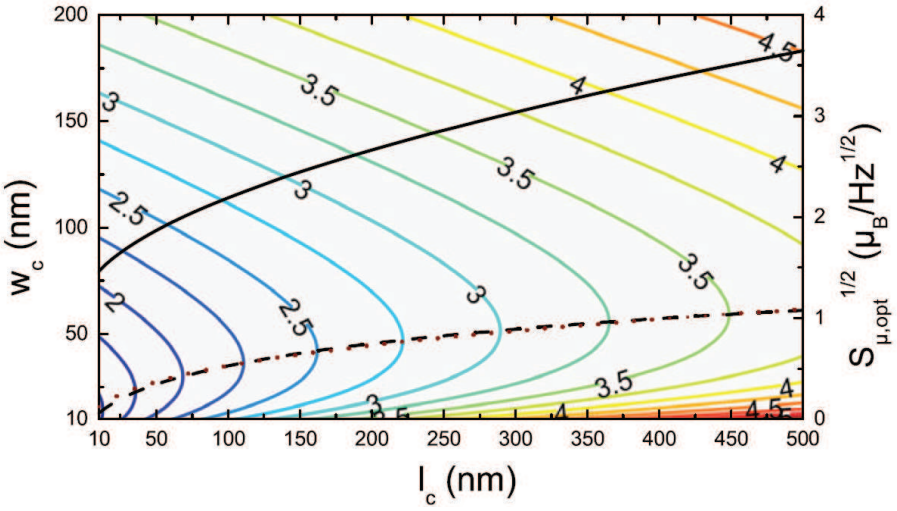

Figure 2.9: $S_{\mu,\mathrm{opt}}(w_\mathrm{c}, l_\mathrm{c})$ for optimum values $d_\mathrm{opt} = 120\,\mathrm{nm}$ and $\beta_\mathrm{L,opt} = 0.4$. The dotted and the dashed lines show $w_\mathrm{c,min}(l_\mathrm{c})$. The solid line indicates $S_{\mu,\mathrm{opt}}(l_\mathrm{c})$ for $w_\mathrm{c} = w_\mathrm{c,min}$. Figure from appended Publication 3.

Fig. 2.9 shows $S_{\mu,\mathrm{opt}}^{1/2}$ for optimum values of $\beta_{\mathrm{L,opt}} = 0.4$ and $d_{\mathrm{opt}} = 120\,\mathrm{nm}$. The coloured lines give $S_{\mu,\mathrm{opt}}^{1/2}(w_{\mathrm{c}}, l_{\mathrm{c}})$, the dashed and dotted lines show $w_{\mathrm{c,min}}(l_{\mathrm{c}})$ and the numbers within the plot give the according spin sensitivity in units of $\mu_{\mathrm{B}}/\mathrm{Hz}^{1/2}$. It becomes apparent, that by shrinking down l_{c}, $S_{\mu}^{1/2} \approx 1\,\mu_{\mathrm{B}}$ is achievable, however realizing $w_{\mathrm{c,min}}$ becomes impossible with current FIB technology. Still, if we assume more realistic values, e.g. $w_{\mathrm{c}} = 60\,\mathrm{nm}$, $l_{\mathrm{c}} = 100\,\mathrm{nm}$ and $l_{\mathrm{J}} = 200\,\mathrm{nm}$, spin sensitivities of down to $S_{\mu}^{1/2} = 2.4\,\mu_{\mathrm{B}}/\mathrm{Hz}^{1/2}$ are feasible.

In summary, we could achieve a significant improvement of the spin sensitivity $S_{\mu}^{1/2}$ in the thermal white noise limit for the specific design of our YBCO nanoSQUIDs. By applying numerical methods, we find optimum values for the crucial geometrical parameters d, w_{c}, l_{c}, w_{J} and l_{J} yielding $S_{\mu}^{1/2} \approx 1\,\mu_{\mathrm{B}}/\mathrm{Hz}^{1/2}$. While most of these conditions can be fulfilled with currently available fabrication technology, the extremely small size of the constriction demands for novel patterning techniques, e.g. the use of focused He/Ne ion beam milling [76]. By fabricating the corresponding devices, we find good agreement with the theoretical predictions.

Contributions

For the third publication I developed the methods for the determination of the coupling factor and did the main part of the numerical simulations. B. Müller assisted with the simulations and the data analysis. T. Schwarz underpinned the results by fabricating the corresponding nanoSQUIDs and wrote a C based program to automate the numerical simulations.

2.4 Summary of Publication 4:

Low-Noise $YBa_2Cu_3O_7$ Superconducting Quantum Interference Devices for Magnetization Reversal Measurements on Magnetic Particles

With regard to Publication 2, we learned that YBCO nanoSQUIDs are indeed suitable for the detection of nanoscale magnetic systems. However, the flux sensitivity of the presented device is far off from state-of-the-art nanoSQUIDs. Considering Publication 3, we were able to show that by choosing proper geometrical parameters it should be feasible to reach rms flux noise levels of $S_\Phi^{1/2} < 100\,\mathrm{n}\Phi_0/\mathrm{Hz}^{1/2}$, resulting in a spin sensitivity of a few Bohr magnetons. In the study at hand we present an optimized YBCO nanoSQUID with the aforementioned attributes and in addition show first measurements on a small spin system, namely an iron filled carbon nanotube.

The layout of the YBCO nanoSQUID is similar to the devices shown in previous works, cf. Fig. 2.10. Consequently, the physical dimensions were to the greatest possible extent adjusted to the optimum values discussed in the optimization study. Film thickness $d_{\mathrm{YBCO}} = 120\,\mathrm{nm}$ as well as junction width $w_\mathrm{J} \approx 200\,\mathrm{nm}$ are increased and the loop size is shrinked to $350 \times 190\,\mathrm{nm}^2$ to reduce the kinetic inductance contribution to the overall inductance of the device. Hence, we achieve a larger characteristic voltage $V_\mathrm{c} = 2\,\mathrm{mV}$ at $T = 4.2\,\mathrm{K}$ and a by a factor of 10 lower inductance

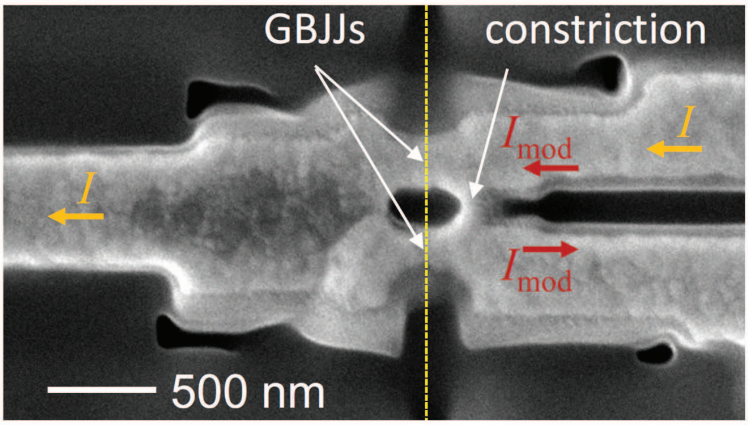

Figure 2.10: SEM image of the optimized YBCO nanoSQUID. Arrows indicate current paths for I_b (orange) and I_mod (red). Dashed yellow line represents the GB. Figure from appended Publication 4. © American Physical Society.

$L = 3.9\,\mathrm{pH}$, as compared to the previous device. The corresponding measurement of the spectral density of rms flux noise is shown in Fig. 2.11 (a). Since the spectrum is dominated by $1/f$-like noise up to the cut-off frequency of the electronics, we can only give an upper limit of the white noise flux level $S_{\Phi,\mathrm{w}}^{1/2} = 50\,\mathrm{n}\Phi_0/\mathrm{Hz}^{1/2}$ above $f = 7\,\mathrm{MHz}$. This extremely low value is on par with state-of-the-art nanoSQUIDs [60] and eventuates in a spin sensitivity of $S_\mu^{1/2} = 3.7\,\mu_\mathrm{B}/\mathrm{Hz}^{1/2}$. The obvious drawback regarding the spectrum in Fig. 2.11 (a) is a reduced flux sensitivity for low frequencies $f \leq 100\,\mathrm{Hz}$ which is problematic since magnetization reversal of e.g. magnetic nanoparticles typically occurs in this frequency range. To overcome this

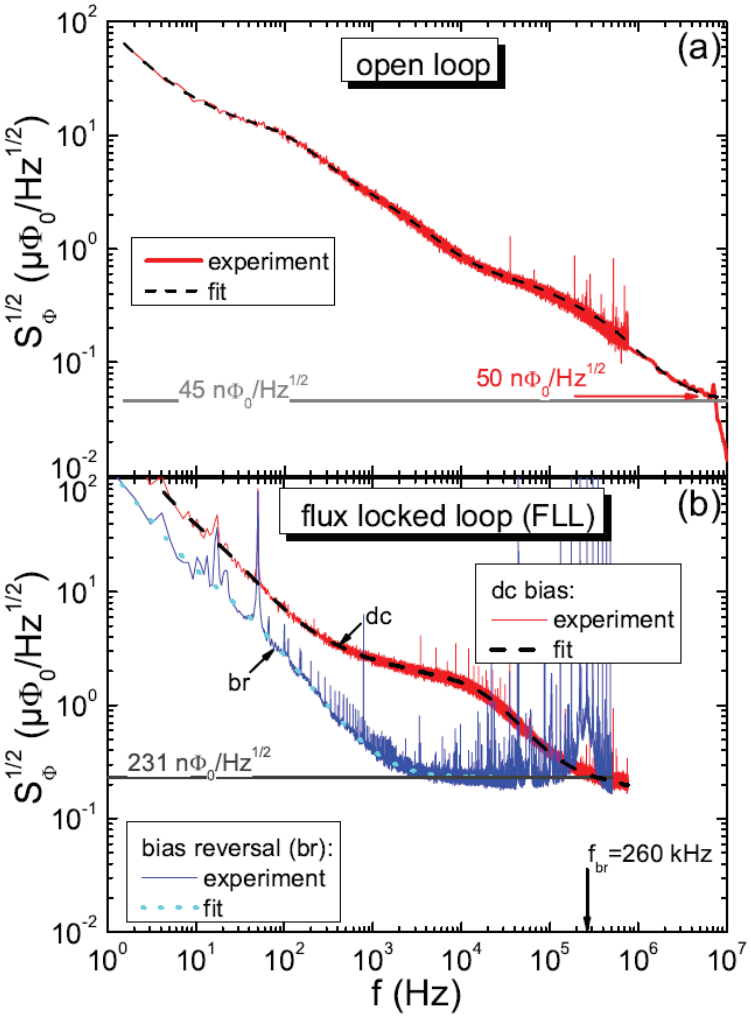

Figure 2.11: $S_\Phi^{1/2}(f)$ for the optimized YBCO nanoSQUID measured in at $T = 4.2\,\mathrm{K}$ (a) open loop and in (b) FLL (red) as well as with bias reversal (br) (blue). The dashed lines in both plots represent fits to the data. Horizontal lines indicate noise level in the white limit. Figure from appended Publication 4. © American Physical Society.

handicap, a bias reversal (br) readout scheme is applied to the nanoSQUID [73], which eliminates the noise contributions of in- and out-of-phase critical current fluctuations in the JJs (s. Fig. 2.11 (b)). The obtained spectra show that the $1/f$-like noise can not entirely be eliminated by the br technique, indicating that another process of fluctuation is involved. At the time of writing this thesis, the origin of this process is unknown, however, we can exclude the existence and motion of Abrikosov vortices in the superconductor since the linewidth of the device is very narrow and the measurements were conducted in a well shielded environment. A possible explanation for this effect are defects in the STO substrate caused by the FIB milling process [77]. Especially oxygen vacancies with magnetic moment come into question [78, 79].

The second part of the study deals with the measurement on an iron nanowire encapsulated in a multiwall carbon nanotube (FeCNT) [80–82]. For this purpose, another (not optimized) YBCO nanoSQUID was fabricated on which the nanoparticle was located (s. Fig. 2.12). The Fe nanowire has a diameter of 39 nm, a length of roughly 14 μm and was positioned near the SQUID loop opposite to the constriction. This position does not constitute the region of optimum coupling (cf. Publication 2 and 3), but prevented the fragile parts of the device from taking damage during the positioning.

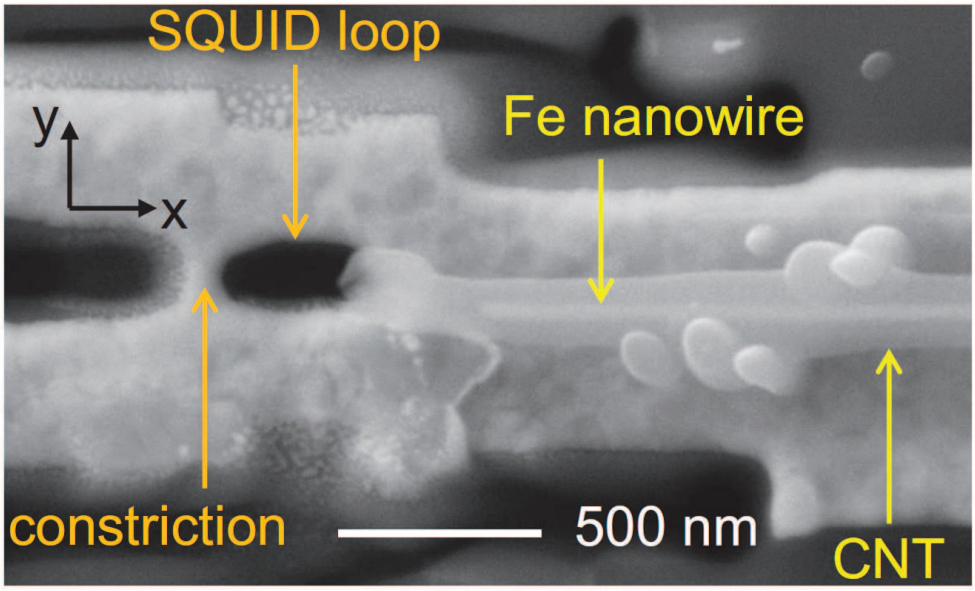

Figure 2.12: SEM image of the FeCNT attached to the nanoSQUID. The magnetic bias field is applied along the x-direction. Figure from appended Publication 4. © American Physical Society.

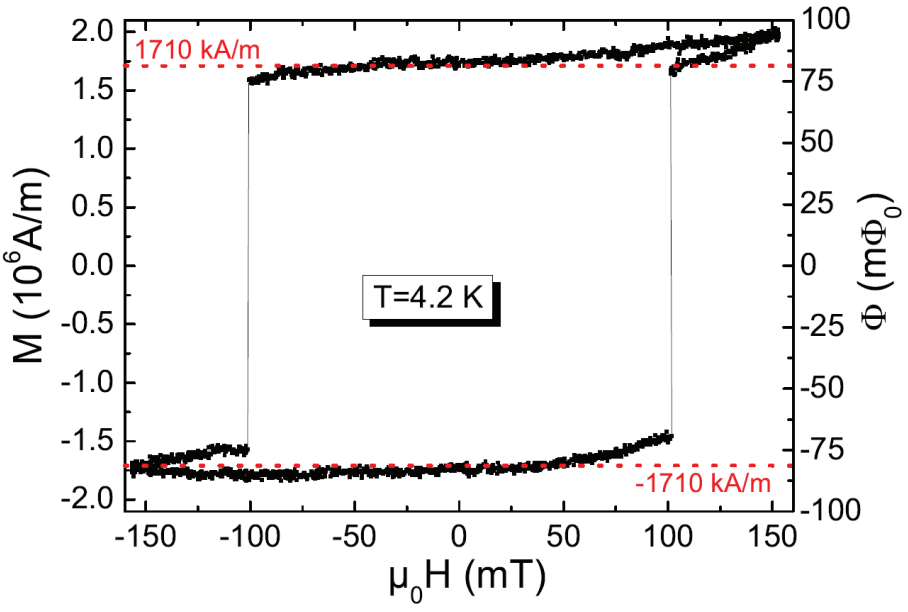

Figure 2.13: Hysteresis loop $\Phi(H)$ of the FeCNT measured with the not optimized YBCO nanoSQUID. Left axis shows corresponding magnetization $M(H)$; dashed red lines show the literature value for the saturation magnetization $\pm M_\mathrm{s}$. Figure from appended Publication 4. © American Physical Society.

By applying a magnetic field parallel to the wire axis, i.e. along the x-direction, we were able to trace out hysteresis curves of the Fe nanowire while running the YBCO nanoSQUID in FLL (s. Fig. 2.13). The nucleation field $H_\mathrm{n} \approx \pm 100\,\mathrm{mT}$ is in accordance with theoretical predictions and indicates a reversal process by curling of magnetization [83]. Furthermore, the hysteresis loop shows a very good signal-to-noise ratio as compared to measurements conducted on similar Fe nanowires by micro-Hall magnetometry [83]. By calculating and integrating the coupling factor over the entire volume of the particle, we are able to theoretically determine the total amount of flux coupled into the SQUID loop by the fully magnetized iron wire. The prediction is conform with the experiment, underpinning once more the validity of our numerical model.

In the supplemental data we investigate an additional YBCO nanoSQUID with respect to frequency-dependent excess noise [84] by numerical methods [85] as a function of temperature. However, we found no systematic dependence on T. Similar to the device in the main part of Publication 4, we find that the br technique can not entirely eliminate $1/f$-noise. Furthermore, the characteristics of the YBCO nanoSQUID used for the measurements on the iron nanowire are discussed in detail. Even though the device is by no means optimized with regard to flux and spin

sensitivity, we were able to investigate the NW, revealing the huge potential of YBCO based nanoSQUIDs for nanomagnetometry.

In conclusion, we fabricated an optimized YBCO nanoSQUID able to detect the flipping of the spin of only a few electrons under convenient conditions. We were able to at least reduce the low-frequency excess noise by applying a bias reversal readout technique. Finally, we demonstrated that even a non optimized device is able to detect the magnetization reversal of an iron nanowire with excellent signal-to-noise ratio.

Contributions

This study was done in collaboration with the group of B. Büchner at the Leibnitz-Institut für Festkörper- und Werkstoffforschung (IFW) in Dresden. The group provided the Fe nanowire and the positioning of the wire on the nanoSQUID was done by C. F. Reiche. The nanoSQUIDs were fabricated by T. Schwarz who also conducted the measurements at $T = 4.2\,\mathrm{K}$. B. Müller performed the measurements at variable temperatures. M. J. Martínez-Pérez assisted the measurements and supported the interpretation of the results. I determined the optimum SQUID parameters and the coupling factor for the nanoSQUID. Furthermore, T. Schwarz and me optimized the measurement setup and the readout electronics.

Chapter 3

Magnetic Nanotubes Studied by Torque and NanoSQUID Magnetometry

In the final chapter of this thesis, we discuss measurements conducted on different magnetic nanotubes with combined torque and nanoSQUID magnetometry [64, 65, 86]. The basic constituents of the setup are depicted in Fig. 3.1.

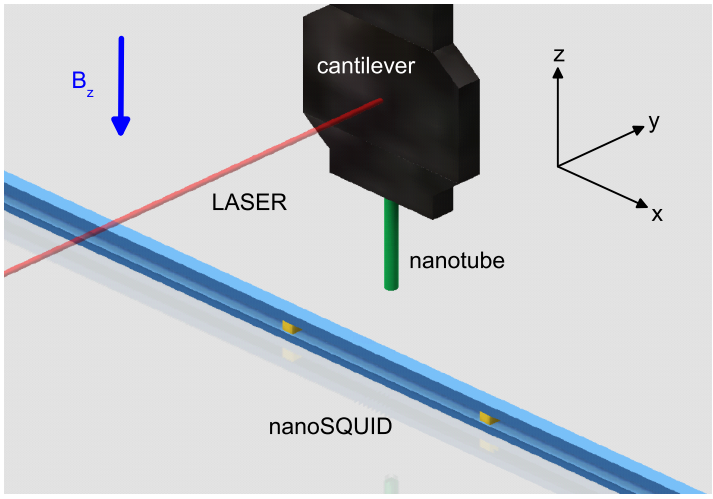

Figure 3.1: Sketch of the setup (not to scale) used for torque and nanoSQUID magnetometry. The cantilever is shown in black along with an attached magnetic NT in green. A Laser is focused on the wide paddle of the cantilever to read out its resonance frequency. The nanoSQUID is mounted below the NT. Blue areas indicate Nb and yellow areas JJs with HfTi barriers. A magnetic field can be applied in the z-direction, i.e. along the axis of the NT.

We use a Nb nanoSQUID with SNS type JJs, similar as in Publication 1, with the main difference being that the devices are not based on two T-shaped Nb arms lying on top of each other, but rather on two Nb strips separated by the two SNS JJs. The revised design allows for operation in larger magnetic fields, i.e. the threshold value at which Abrikosov vortices enter the Nb strips is raised to $\approx 90\,\mathrm{mT}$ at $T = 4.2\,\mathrm{K}$. Furthermore, by doubling the characteristic voltage V_c, we achieve $S_\Phi^{1/2} \approx 190\,\mathrm{n}\Phi_0/\mathrm{Hz}^{1/2}$ in the white noise regime, which corresponds to an improved spin sensitivity of $S_\mu^{1/2} \approx 18\,\mu_\mathrm{B}/\mathrm{Hz}^{1/2}$. It is worth noting here, that with the so far best Nb nanoSQUID with the revised design, we achieve $S_\Phi^{1/2} \approx 110\,\mathrm{n}\Phi_0/\mathrm{Hz}^{1/2}$ and $S_\mu^{1/2} \approx 9.7\,\mu_\mathrm{B}/\mathrm{Hz}^{1/2}$, however these devices have not yet been implemented into the setup.

The single-crystal Si cantilever is fabricated by selective Si epitaxy and patterned by optical lithography and plasma etching. An individual magnetic NP, in this case a magnetic NT, can be attached to the cantilever. Therefore, a drop of epoxy glue is located on the tip of the cantilever via an omniprobe needle and then the NT is placed on the tip by the help of a second needle. A magnetic field B_z can be created in z-direction by a superconducting coil, inducing torque on the cantilever due to the interaction of the applied field and the magnetic moment of the NT. The torque leads to a change in the resonance frequency f_res of the cantilever, which is read out by a Laser interferometer. To increase the signal-to-noise ratio of the frequency measurement, the cantilever is additionally exited via a piezo.

Recent works have shown that hollow tubular nanostructures can be synthesized reliably and are potentially helpful for applications in biotechnology [3, 87–89]. Also, in contrast to magnetic nanowires, NTs exhibit more controllable reversal processes due to the absence of magnetic vortex cores or Bloch points [90]. The relatively low coercive fields in the range of $\approx 10\,\mathrm{mT}$ predestine this type of magnetic system for magnetometry with the Nb nanoSQUIDs.

Two different NTs were investigated: (a) Permalloy (Py) and (b) a compound of Co and Fe (CoFeB) [91]. The basic geometry of both tubes is depicted in Fig. 3.2 (a). The core of the tubes is made of the semiconductor GaAs and has a radius of $r_\mathrm{i} \approx 80\,\mathrm{nm}$. The GaAs is coated with a thin shell of ferromagnetic (FM) material, defining the outer radius $r_\mathrm{o} \approx 110\,\mathrm{nm}$. Along with the length L of the tube and the magnetic exchange length λ_ex of the respective material, these parameters define the magnetic equilibrium state of the tube. Fig. 3.2 (b) shows the theoretically predicted phase diagram for the three possible magnetic states as a function of tube dimensions. We find that for very thin and long tubes, the magnetization will

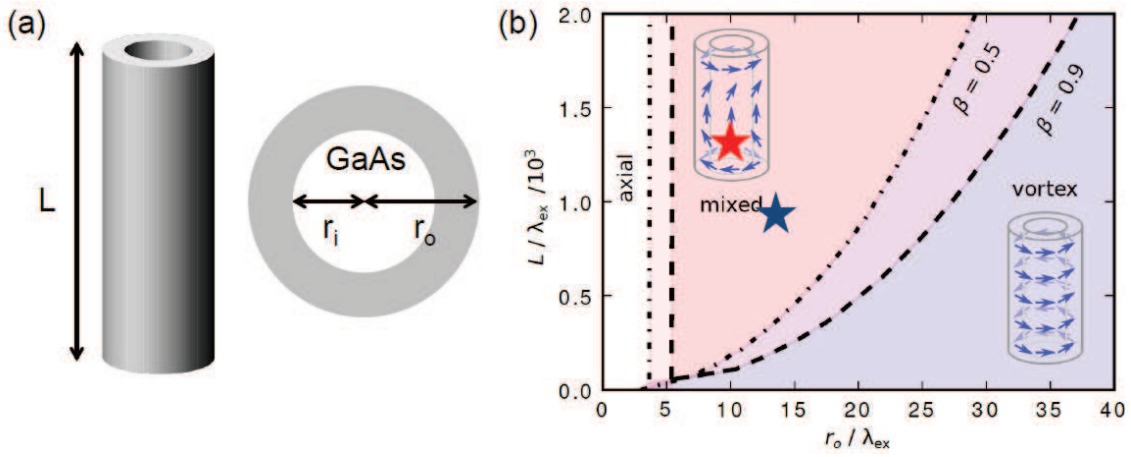

Figure 3.2: (a) Basic geometry of the magnetic NTs. Grey areas represent the magnetic shell. The inner core is GaAs. (b) Phase diagram for magnetic NTs: Normalized length L vs normalized outer radius r_o as a function of the possible equilibrium states, which are illustrated by the two insets, with arrows indicating the orientation of local magnetic moments. Dotted and dashed lines give phase transitions for $\beta = r_\mathrm{i}/r_\mathrm{o} = 0.5$ and $\beta = 0.9$, respectively. Red (blue) star indicates position of the investigated Py- (CoFeB-) NT in the phase diagram. Figure adapted from [91].

be uniform, i.e. all magnetic moments are oriented along the axis of the NT. For thick and short tubes, the magnetization configuration will prefer the vortex state, which features no magnetic stray field [92]. However, for the investigated Py- and CoFeB-NTs, it becomes apparent that the mixed state is favored, which in essence is a superposition of the former two. A similar phase diagram can be calculated for the reversal mechanism in magnetic NTs. Here, we find the propagation of a vortex domain wall to be the dominant magnetization reversal process for the studied samples.

An extract of the experimental results obtained from measurements on the CoFeB-NT is shown in Fig. 3.3. With the use of a three-stage piezo system for motion in x-, y- and z-direction, we can scan the nanoSQUID close to the NT, while operating the SQUID at the optimum working point in open loop mode. Prior to these measurements, the NT was magnetized at $B = 3\,\mathrm{T}$, while the scanning was performed in zero field. The obtained coupling scan $\Phi(x, y, z = 1\,\mu\mathrm{m})$ is shown in Fig. 3.3 (a). Bright (dark) areas represent positions where the NT couples positive (negative) flux into the SQUID loop, cf. colour bar to the right of the plot. The Φ-asymmetry in the contour plot can be attributed to a minor misalignment of the plane of the SQUID with respect to the y-direction. The long yellow rectangle indicates the position of the Nb

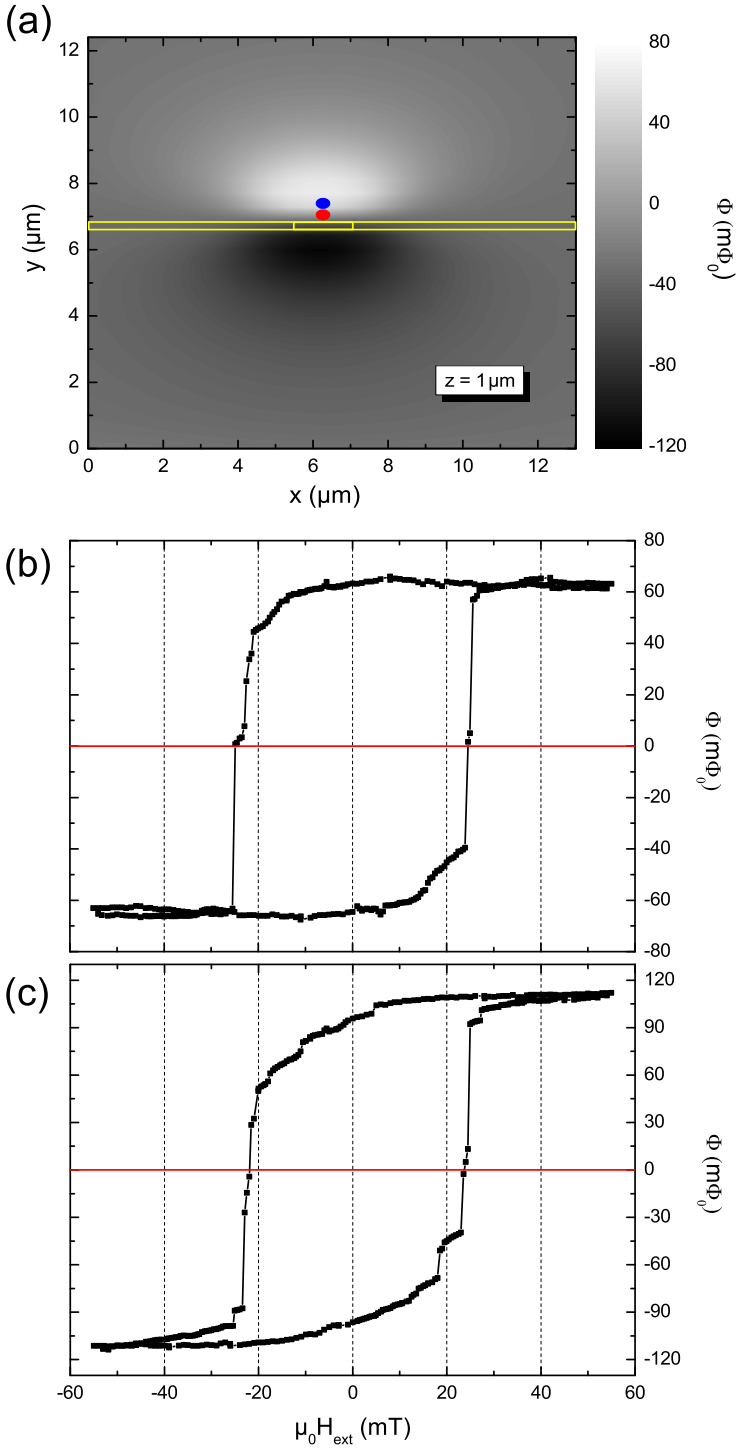

Figure 3.3: (a) Coupling map $\Phi(x, y, z = 1\,\mu\text{m})$. The yellow rectangles show position of the Nb strips and the nanoSQUID loop. (b) Hysteresis $\Phi(H_{\text{ext}})$ loop recorded with the CoFeB-NT positioned according to the blue point in (a). (c) Hysteresis loop with the NT located as indicated by the red point in (a).

strips and the smaller rectangle represents the nanoSQUID loop. The blue and the red point show the positions where the NT was located for the hysteresis measurements $\Phi(H_{\mathrm{ext}})$ in (b) and (c). For the measurement shown here, the voltage drop across the nanoSQUID is amplified by a second stage series SQUID array (SSA), to exploit the full sensitivity of the device. In addition, both stages are operated in FLL during the field sweeps. Fig. 3.3 (b) displays a quite rounded hysteresis loop with nucleation fields around $\mu_0 H_{\mathrm{n}} \approx \pm 25\,\mathrm{mT}$. Moreover, the CoFeB-NT seems to favor an intermediate magnetic state which produces almost no stray field coupling into the SQUID as indicated by the red horizontal line in Fig. 3.3 (b). A global vortex-like configuration of the magnetization, however, seems unlikely since theory predicts a mix of a uniform state and a vortex-like state for the NTs under investigation (cf. Fig. 3.2 (b)). Since the nanoSQUID is most sensitive to the bottom end of the NT [65], one can envision a reversal process involving the nucleation of a vortex wall in the lower portion of the NT which counterbalances the stray field of the vortex configuration at the bottom end. In this scenario, the SQUID would detect no magnetic flux, while net magnetization of the NT would remain finite, as it is seen by cantilever magnetometry.

Fig. 3.3 (c) shows the hysteresis loop as measured at a position which corresponds to the red point in Fig. 3.3 (a), i.e. roughly 200 nm closer (in y-direction) to the SQUID loop as compared to the blue point. Obviously, the peak-to-peak signal increases, but also the hysteresis becomes more rounded and additional steps occur, while some are more pronounced than before. We assign this behavior to the nucleation of a vortex wall at the bottom end of the NT, as discussed before, since the nanoSQUID is now more sensitive to signals arising from magnetization components in y-direction.

To reveal the true nature of the magnetization reversal process of the CoFeB-NT, micromagnetic simulations as in [65] will be applied in the near future.

Continuing with the Py-NT, we conducted similar measurements as for the CoFeB sample. Fig. 3.4 shows the first and second hysteresis measurement right after cooling the sample to $T = 4.2\,\mathrm{K}$ in zero field. Both curves are shifted to the left with respect to the field axis, indicating the involvement of an antiferromagnetic (AFM) constituent in the Py shell, leading to an exchange bias effect [93–95]. X-ray absorption spectroscopy (XAS) conducted on different Py-NT at the Paul-Scherrer-Institut (PSI) in Switzerland indeed revealed that the samples are coated with a thin AFM layer ($< 5\,\mathrm{nm}$) of FeO and presumably NiO. The shift in the hysteresis loops is described by the exchange bias field $H_{\mathrm{ex}} = \frac{1}{2}(|H_{\mathrm{l}} + |H_{\mathrm{r}}|)$, where H_{l} and H_{r} are the switching fields on the left and right side of the hysteresis curve, respectively.

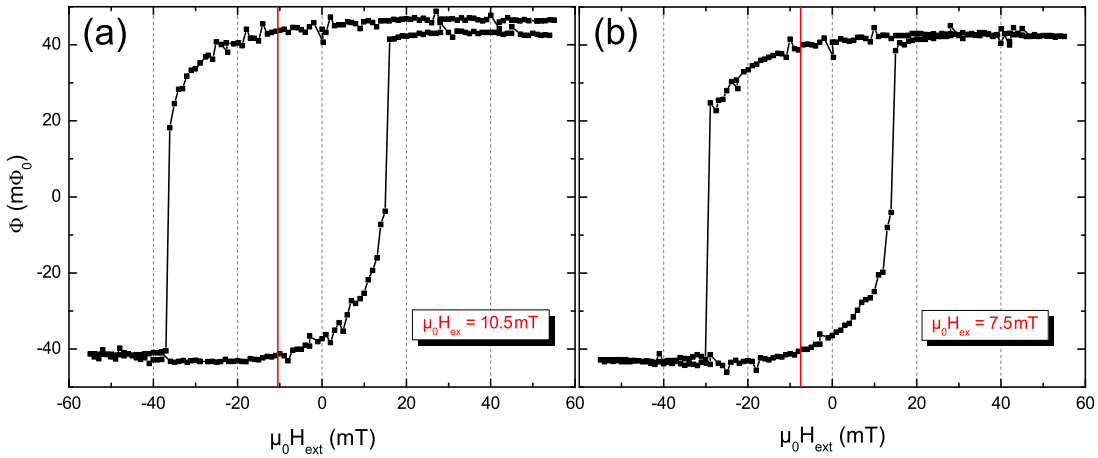

Figure 3.4: (a) First hysteresis loop and (b) second hysteresis loop of the Py-NT. The vertical red lines indicate the exchange bias field.

Fig. 3.4 (b) shows the second hysteresis loop recorded shortly after the first one. H_{ex} has slightly decreased, which is common for exchange bias systems, known as the training effect. Furthermore, the measurements show similar roundings as for the CoFeB samples, indicating that the nucleation and propagation of domain walls is the dominant reversal mechanism. The interaction between the FM and the AFM layer also seems to have an effect on the switching of the magnetization, since the reversal for positive fields appears to involve more domain walls than the reversal for negative fields.

Fig. 3.5 schematically depicts the exchange bias effect: (a) shows the characteristic hysteresis loop and (b) the configurations of the magnetization of the FM and AFM layer. We start at $T = 300\,\mathrm{K}$ which is in between of the Curie temperature for Py ($T_{\mathrm{C}} \approx 800\,\mathrm{K}$) and the Néel temperature of FeO ($T_{\mathrm{N}} \approx 200\,\mathrm{K}$). For the sake of simplicity, we assume the FM layer to be in a fully magnetized state. In the next step, the system is cooled down to below $T_{\mathrm{N}} \approx 200\,\mathrm{K}$ in an applied magnetic field H_{cool}, which is usually in the range of 100 mT. This leads to a magnetization of the AFM layer as depicted by picture 1 in Fig. 3.5 (b) which corresponds to point 1 in the hysteresis loop of Fig. 3.5 (a). By applying an external field H_{ext} opposite to H_{cool}, the switching of magnetization occurs at $-(H_{\mathrm{c}}+H_{\mathrm{ex}})$ (point 2 and 3), since H_{ext} has not only to overcome H_{c} but also the internal field arising from magnetization of the AFM which is closest to the FM layer. Reversing the applied field, leads to switching at lower field values, because now H_{ext} and the internal field add up (point 4). The result is a hysteresis loop which is shifted to the left, without

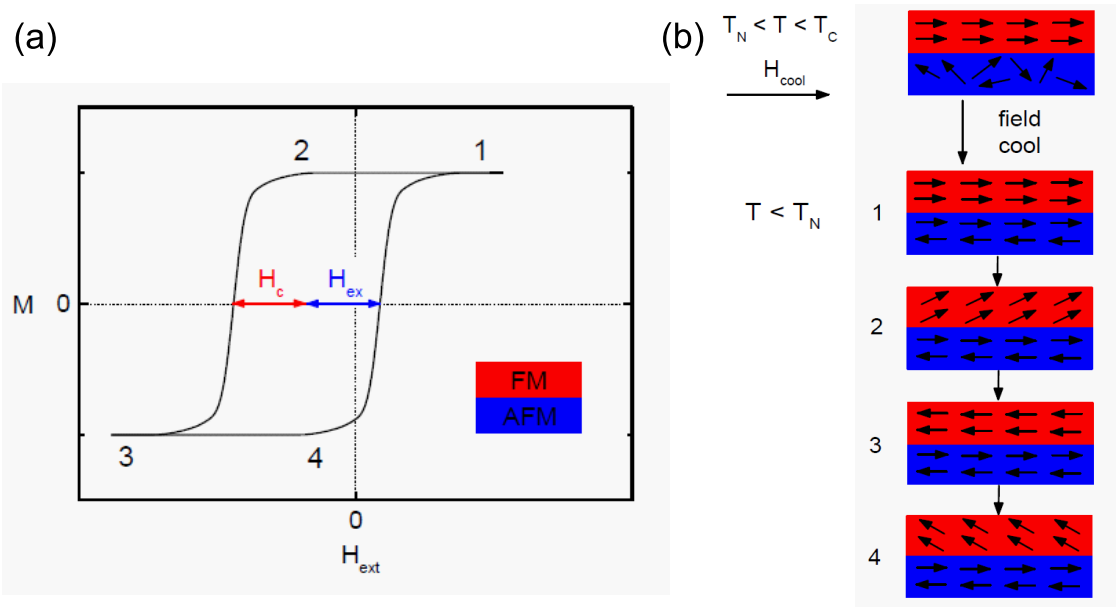

Figure 3.5: (a) Characteristic hysteresis loop for an exchange bias system. (b) Magnetization configurations for the FM and AFM layer. Here, T_N is the Néel temperature of the AFM and T_C is the Curie temperature of the FM.

loss of generality. Note that for the measurements shown in Fig. 3.4, the Py-NT was cooled in zero field. However, hysteresis loops performed after cooling in an applied field of $\mu_0 H_{\mathrm{cool}} = 200\,\mathrm{mT}$ showed no significant differences.

While the origin of the exchange bias effect is well understood, the nature of the training effect is not (see e.g. [96–98] and references therein). Fig. 3.6 displays the evolution of the exchange bias field with consecutive hysteresis loops $H_{\mathrm{ex}}(n)$. The red curve is a fit to the data according to $H_{\mathrm{ex}}(n) = H_{\mathrm{ex}}^{\mathrm{e}} + \kappa/\sqrt{n}$, with the exchange bias field in the limit of infinite loops $\mu_0 H_{\mathrm{ex}}^{\mathrm{e}} = 2.6\,\mathrm{mT}$ and a system dependent constant $\mu_0\kappa = 7.8\,\mathrm{mT}$. The obtained fit parameters are more or less in accordance with literature, but provide no further insight into the microscopic character of the training effect. To explain this effect, several models have been developed over the years, however the underlying mechanism remains controversial. To just take a single example, A. Hoffmann [99] assumes the existence of various anisotropy axes within the AFM layer that initially stabilize a non-collinear configuration of the AFM spins. With growing number of hysteresis loops n, this arrangement relaxes into a collinear configuration.

It is well known that exchange bias systems exhibit a critical temperature above

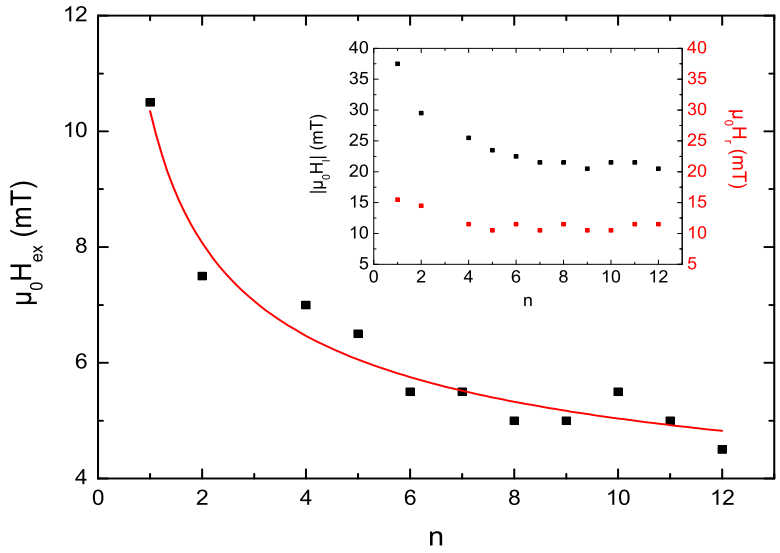

Figure 3.6: Exchange bias field as a function of loop number. Red line is a fit to the data points. Inset shows evolution of the switching fields $|H_\mathrm{l}|(n)$ (black points; left axis) and $H_\mathrm{r}(n)$ (red points; right axis).

which H_ex vanishes, known as the blocking temperature T_B [100–103]. For bulk size AFM, $T_\mathrm{B} = T_\mathrm{N}$, but with shrinking dimensions of the AFM, T_B should approach very low temperatures. Due to the limited range of operation temperature for the Nb nanoSQUID, below $T_\mathrm{c} \approx 9\,\mathrm{K}$, we conducted cantilever magnetometry to find T_B for the Py-NT, because the properties of the cantilever do not significantly change in the low temperature regime ($\leq 50\,\mathrm{K}$). We find that H_ex drops to zero for $T \approx 13\,\mathrm{K}$ and furthermore that the hysteresis loops become symmetric with respect to the nature of the reversal mechanism, unlike in Fig. 3.4. Just like the XAS measurements, the low T_B indicates a very thin AFM layer of just a few nm thickness.

In summary of chapter 3, we found that nanometer sized magnetic nanotubes feature a huge variety of interesting effects. Nb nanoSQUIDs are highly suitable for the exploration of these systems because of their relatively large magnetic field tolerance and extremely high flux and spin sensitivity. However, to gain a more detailed comprehension of nanomagnetism, numerical methods need to be applied to the specific geometries of the samples under investigation.

The measurements were preformed in a collaboration with A. Buchter, M. Wyss and M. Poggio at the Department of Physics of the University of Basel, Switzerland. The magnetic nanotubes were fabricated by D. Rüffer, E. Russo-Averchi, A. Fontcuberta I Morral of the Laboratoire des Matériaux Semiconducteurs EPF in

Lausanne, Switzerland and by R. Huber, P. Berberich, D. Grundler of the Physik-Department E10 of the Technische Universität München, Germany.

Appendix A: Numerical Simulations of the Coupling Factor

In this Appendix, the methods as used in Publication 3 for deriving the coupling factor ϕ_μ are discussed. For this purpose, we use the software package 3D-MLSI for numerical simulations of current distributions and inductances in superconducting thin films [74]. The central quantity is the thickness-integrated current density

$$\vec{J}(x,y) = \int dz \vec{j}(x,y,z) = (J_x, J_y), \tag{1}$$

called sheet current density [104]. Since $\nabla \cdot \vec{J} = 0$ in the thin film, $\vec{J}$ can be expressed by a scalar potential $g(x,y)$, called stream function, with the property

$$\vec{J} = -\hat{z} \times \nabla g = \nabla \times (\hat{z} g) = (\partial g/\partial y, -\partial g/\partial x). \tag{2}$$

In other words, the contour lines of $g(x,y)$ are the current stream lines and the difference $g(x_1,y_1) - g(x_2,y_2)$ is the current that crosses the line connecting the points (x_1,y_1) and (x_2,y_2) within the film. Furthermore, using stationary London and Maxwell equations

$$\lambda_\mathrm{L}^2 \nabla \times \vec{J} + \vec{H} = 0, \tag{3}$$

$$\nabla \times \vec{H} = \vec{J}, \tag{4}$$

external magnetic fields $\vec{H}$ can be included and fields arising from the current sheet can be calculated. Beyond that, the software package enables to determine the inductance matrix by calculating the full energy of a set of superconductors, as well as fluxoids for holes in superconductors. For details see [74, 104, 105] and references therein.

The numerical procedure of 3D-MLSI is based on the finite-element-method (FEM). The thin film superconductors are subdivided into smaller (finite) parts (triangles)

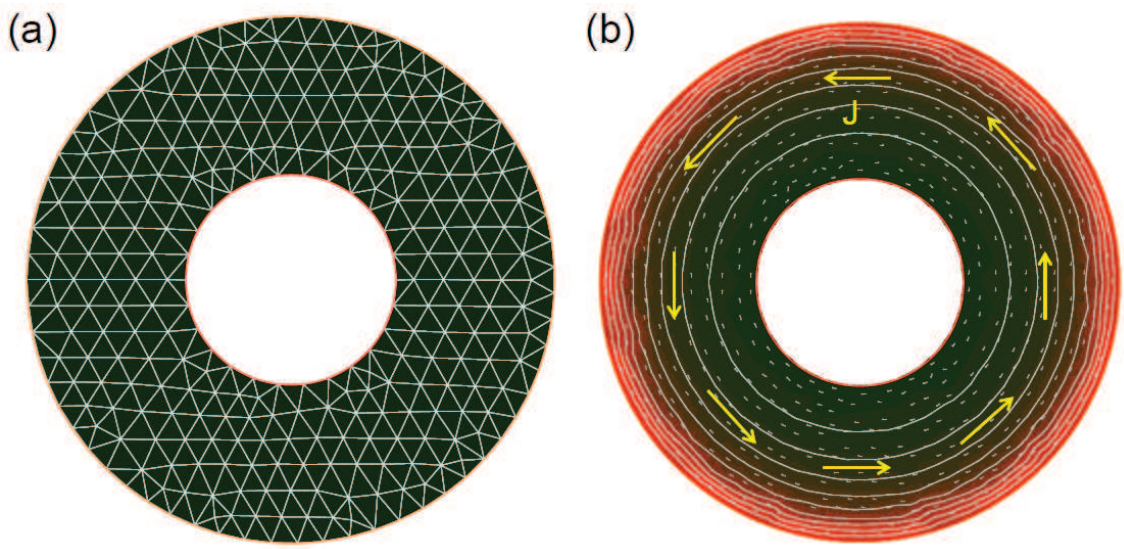

Figure A1: (a) Triangulation of a superconducting ring. (b) 3D-MLSI output: the current distribution $\vec{J}(x,y)$ is indicated by the yellow arrows, white lines indicate equipotential lines of the stream function $g(x,y)$. Amplitude of the $\vec{J}(x,y)$ is encoded in colour with red areas indicating locations of high current density.

within which the system of partial differential equations (3), (4) is solved. For the boundary conditions, $g(x,y) = 0$ at the edges of the films and $g(x,y) = \text{const.}$ inside an isolated hole or slit within the film. Fig. A1 (a) shows an example for the subdivision of a superconducting ring into triangles (triangulation) and (b) the corresponding current distribution for an applied field $B = 1\,\text{mT}$ normal to the surface of the film and zero trapped flux in the hole.

Method 1

Method 1 is similar to the approach first presented in [69]. First we give 3D-MLSI the exact physical dimensions of the nanoSQUID and choose an arbitrary value (1 mA) for the total current J_{total} circulating around the SQUID hole. With the corresponding sheet current density distribution $\vec{J}(x,y)$ we calculate the magnetic field distribution $\vec{B}(\vec{r})$ generated in 3D space in the vicinity of the device. The coupling factor is obtained from

$$\phi_\mu = -\hat{e}_\mu \cdot \vec{B}(\vec{r})/J_{\text{total}}, \tag{5}$$

with $\hat{e}_\mu$ being the unit vector along the direction of the magnetic moment $\vec{\mu} = \mu\hat{e}_\mu$ at position $\vec{r}$. Note that in this case the magnetic moment is "virtual" and point-like. But also for finite size magnetic objects, ϕ_μ can be derived by integrating the

coupling factor over the corresponding volume of the object [64]. In earlier works [62, 63, 69] we used two current sheets located at the upper and lower surface of the superconductor and calculated an averaged $< \vec{B}(\vec{r}) >$ arising from two sheets. However, if one is interested in the scaling of ϕ_μ with film thickness d, it is appropriate to use more current sheets to avoid numerical artefacts, as shown in Publication 3. As a result, we found that ϕ_μ is up to 20% smaller if a more realistic number of sheets ($n = 11, 101$) is considered.

Method 2

Since the derivation of (5) in [69] was rather controversial, we developed another approach to the problem. Instead of considering a virtual magnetic moment near the SQUID loop, we construct a "quasi-dipole" with finite size within 3D-MLSI, cf. Fig. A2. Obviously, the simplest way to mimic a magnetic dipole would be a circulating current in a tiny ring. However, within 3D-MLSI, it is not possible to construct such an object in the x-z-plane forming a dipole in y-direction, as it is favorable for the YBCO nanoSQUID design. Instead, we consider two strips lying on top of each other as depicted in Fig. A2. Currents flowing along $\hat{e}_\mathrm{x}$ ($-\hat{e}_\mathrm{x}$) in the lower (upper) strip create a quasi-dipole field with a magnetic moment oriented along $-\hat{e}_\mathrm{y}$. The currents can be adjusted to generate the magnetic moment of a

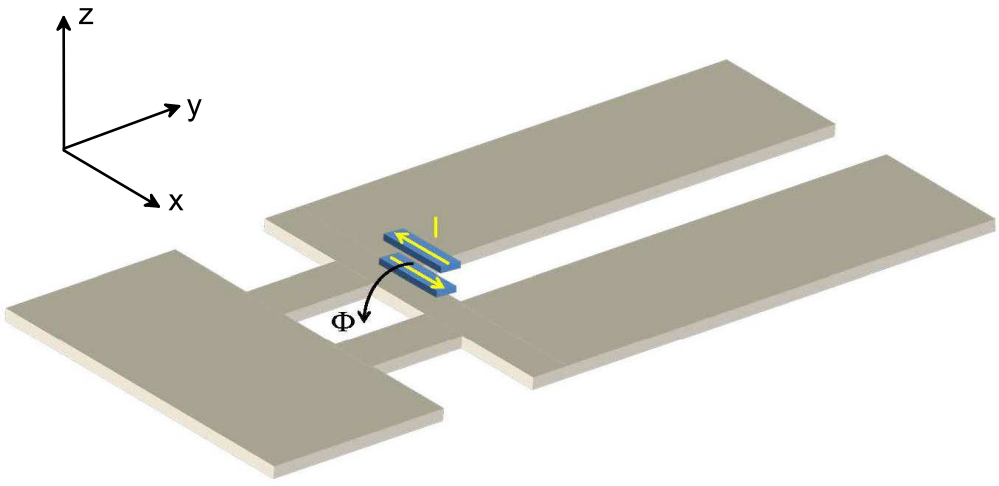

Figure A2: Sketch of the YBCO nanoSQUID (grey) as presented in Publication 2, 3 and 4 and the quasi-dipole (blue) formed by two superconducting strips (not to scale). Yellow arrows indicate currents which generate a magnetic dipole field.

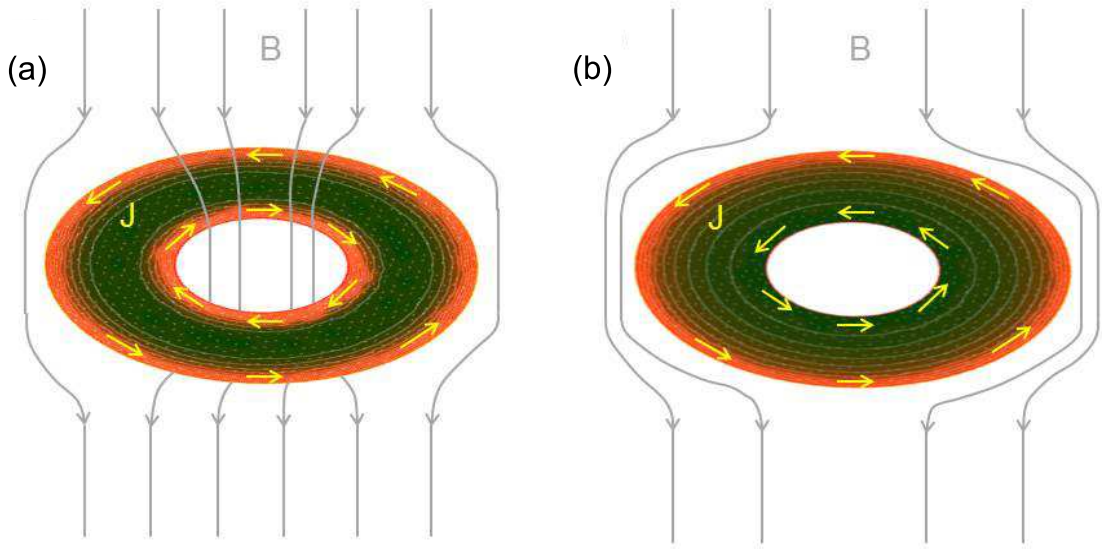

Figure A3: Current and field distribution for the case of ideal flux focussing (a) and ideal screening (b) for a simple superconducting ring in a homogenous magnetic field B applied normal to the film surface. For reasons of clarity, the current paths are emphasized by yellow arrows. Magnetic field lines are indicated in grey.

single Bohr magneton μ_{B}. The quasi-dipole formed in this manner does not feature the magnetic field distribution of an ideal dipole, since the strips are not connected. However, the field generated by the missing links is of minor relevance, since it would not interact with the superconducting structures or the SQUID hole. In Fig. 2 of Publication 3 it is shown that the quasi-dipole is a very good approximation to an ideal magnetic dipole with only minor deviations of around 1%.

To get access to ϕ_μ, we use problem 3 ("pb = 3") within 3D-MLSI, which allows for setting the total current circulating around the hole to a desired value by the command line "hc i n", with i being the hole number and n the total current. We choose $J_{\mathrm{total}} = 0$, which means that the screening currents in the superconducting structures induced by the magnetic field of the quasi-dipole are counterbalanced so that there is no net current circulating in the loop. The situation corresponds to the case of ideal flux focussing and is schematically shown in Fig. A3 (a) for a simple superconducting ring. In this case the output of 3D-MLSI is the fluxoid ϕ_{fluxoid} induced in the SQUID hole by a magnetic moment with an amplitude of one Bohr magneton. Thus, we can interpret the result as the coupling factor $\phi_\mu = \phi_{\mathrm{fluxoid}}/\mu_{\mathrm{B}}$. Similar to Method 1, the calculation is deployed for $n = 11$ current sheets.

Method 3

For Method 3 we again consider the quasi-dipole as introduced in Method 2. In contrast to the former approach, we now use problem 2 ("pb = 2") within 3D-MLSI, which allows to fix the number n of flux quanta trapped in the hole with number i to a desired value by the command line "hc i n". For our purposes, we set $n = 0$, which means the loop will induce screening currents that shield the magnetic field generated by the quasi-dipole, i.e. we consider the case of ideal screening (cf. Fig. A3 (b)). The coupling factor $\phi_\mu = LJ_{\mathrm{screen}}/\mu_{\mathrm{B}}$ is obtained by computing the total screening current J_{screen} and the inductance L of the bare SQUID (without quasi-dipole). As before, the calculation is performed for $n = 11$ current sheets.

As already pointed out in the summary of Publication 3, the three Methods yield the same results and therefore constitute a valid approach for calculating the coupling factor.

Appendix B: List of acronyms and physical constants

List of acronyms

3D-MLSI	3-dimensional multilayer superconducting integrated circuits
AFM	antiferromagnet/antiferromagnetic
br	bias reversal
cJJ	constriction type Josephson junction
CNT	carbon nanutube
dc	direct current
FEM	finite-element-method
FIB	focused ion beam
FLL	flux locked loop
FM	ferromagnet/ferromagnetic
GB	grain boundary
IFW	Leibnitz-Institut für Festkörper- und Werkstoffforschung
IVC	current-voltage-characteristic
JJ	Jospehson junction
NP	nanoparticle
NT	nanotube
NW	nanowire
PSI	Paul-Scherrer-Institut
PTB	Physikalisch Technische Bundesanstalt
Py	Permally
rf	radio frequency
rms	root mean square
SEM	scanning electron microscopy
SNS	superconductor normal metal superconductor

SOT	SQUID-on-tip
SQUID	superconducting quantum interference device
SSA	series SQUID array
STO	strontium titanate
XAS	X-ray absorption spectroscopy
YBCO	yttrium barium copper oxide $YBa_2Cu_3O_7$

List of physical constants

$\mu_B = 9.274 \cdot 10^{-24}\,J/T$	Bohr magneton
$\Phi_0 = 2.072 \cdot 10^{-15}\,Tm^2$	magnetic flux quantum
$\mu_0 = 4\pi \cdot 10^{-7}\,Tm/A$	vacuum permeability
$k_B = 1.38 \cdot 10^{-23}\,J/K$	Boltzmann constant

Bibliography

[1] Q. A. Pankhurst, N. T. K. Thanh, S. K. Jones and J. Dobson. Progress in Applications of Magnetic Nanoparticles in Biomedicine. *J. Phys. D: Appl. Phys.*, **42**, 224001, 2009.

[2] D. H. Reich, M. Tanase, A. Hultgren, L. A. Bauer, C. S. Chen and G. J. Meyer. Biological Applications of Multifunctional Magnetic Nanowires. *J. Appl. Phys.*, **93**, 7275, 2003.

[3] P. Landeros, P. R. Guzmán, R. Soto-Garrido and J. Escrig. Magnetic Fields in Tubular Nanostructures. *J. Phys. D: Appl. Phys.*, **42**, 225002, 2009.

[4] P. Bushev, D. Bothner, J. Nagel, M. Kemmler, K. B. Konovalenko, A. Loerincz, K. Ilin, M. Siegel, D. Koelle, R. Kleiner and F. Schmidt-Kaler. Trapped Electron Coupled to Superconducting Devices. *Eur. Phys. J. D*, **63**, 9, 2011.

[5] S. D. Bader. Colloquium: Opportunities in Nanomagnetism. *Rev. Mod. Phys.*, **78**, 1, 2006.

[6] J. Bartolomé, F. Luis and J. F. Fernández (editors). *Molecular Magnets: Physics and Applications.* NanoSciene and Technology. Springer, Heidelberg, 2014.

[7] M. N. Leuenberger and D. Loss. Quantum Computing in Molecular Magnets. *Nature*, **410**, 789-793, 2001.

[8] R. H. Kodoma. Magnetic Nanoparticles. *J. Magn. Magn. Mater.*, **200**, 359-372, 1999.

[9] W. Wernsdorfer. Classical and Quantum Magnetization Reversal Studied in Nanometersized Particles and Clusters. *Adv. Chem. Phys.*, **118**, 99-190, 2001.

[10] C. P. Bean and I. S. Jacobs. Magnetic Granuloemtry and Super-Paramagnetism. *J. Appl. Phys.*, **27**, 1448, 1956.

[11] C. P. Bean and J. D. Livingston. Superparamagnetism. *J. Appl. Phys.*, **30**, 120, 1959.

[12] A. Ito, M. Shinkai, H. Honda and T. Kobayashi. Medical Application of Functionalized Magnetic Nanoparticles. *J. Biosci. Bioeng.*, **100**, 1-11, 2005.

[13] S. C. McBain, H. H. P. Yiu and J. Dobson. Magnetic Nanoparticles for Gene and Drug Delivery. *Int. J. Nanomed.*, **3**, 169-180, 2008.

[14] K. Ohno, C. Mori, T. Akashi, S. Yoshida, Y. Tago, Y. Tsujii and Y. Tabata. Fabrication of Contrast Agents for Magnetic Resonance Imaging from Polymer-Brush-Afforded Iron Oxide Magnetic Nanoparticles Prepared by Surface-Initiated Living Radical Polymerization. *Biomacromolecules*, **14**, 3453-3462, 2013.

[15] B. Thiesen and A. Jordan. Clinical Applications of Magnetic Nanoparticles for Hyperthermia. *Int. J. Hyperthermia*, **24**, 467-474, 2008.

[16] A. Jordan, R. Scholz, P. Wust, H. Fähling and R. Felix. Magnetic Fluid Hyperthermia (MFH): Cancer Treatment with AC Magnetic Field Induced Excitation of Biocompatible Superparamagnetic Nanoparticles. *J. Magn. Magn. Mat.*, **201**, 413-419, 1999.

[17] R. C. Semelka and T. K. G. Helmberger. State of the Art: Contrast Agents for MR Imaging of the Liver. *Radiology*, **218**, 27-38, 2001.

[18] R. Klingeler, S. Hampel and B. Büchner. Carbon Nanotube Based Biomedical Agents for Heating, Temperature Sensoring and Drug Delivery. *Int. J. Hyperthermia*, **24**, 496, 2008.

[19] P. Laird, R. Bergamasco, V. Berube, E. F. Borra, A. Ritcey, M. Rioux, N. Robitaille, S. Thibault, L. V. da Silva Jr. and H. Yockell-Lelievre. Ferrofluid Based Deformable Mirrors: A New Approach to adaptive Optics Using Liquid Mirrors. *Proc.SPIE Int. Soc. Opt. Eng.*, **4839**, 733, 2003.

[20] S. Odenbach, editor. Ferrofluids. *J. Phys.: Condens. Matter*, **18**, 38, 2006.

[21] L. Bogani and W. Wernsdorfer. Molecular Spintronics Using Single-Molecule Magnets. *Nature Materials*, **7**, 179-186, 2008.

[22] S. N. Piramanayagam and K. Srinivasan. Recording Media Research for Future Hard Disk Drives. *J. Magn. Magn. Mat.*, **321**, 485-494, 2009.

[23] D. Rugar, R. Budakian, H. J. Mamin and B. W. Chui. Single Spin Detection by Magnetic Resonance Force Microscopy. *Nature*, **430**, 329-332, 2004.

[24] J. R. Maze, P. L. Stanwix, J. S. Hodges, S. Hong, J. M. Taylor, P. Cappellaro, L. Jiang, M. V. Gurudev Dutt, E. Togan, A. S. Zibrov, A. Yacoby, R. L. Walsworth and M. D. Lukin. Nanoscale Magnetic Sensing with an Individual Electronic Spin in Diamond. *Nature*, **455**, 644-647, 2008.

[25] G. Balasubramanian, I. Y. Chan, R. Kolesov, M. Al-Hmoud, J. Tisler, C. Shin, C. Kim, A. Wojcik, P. R. Hemmer, A. Krueger, T. Hanke, A. Leitenstorfer, R. Bratschitsch, F. Jelezko, and J. Wrachtrup. Nanoscale Imaging Magnetometry with Diamond Spins Under Ambient Conditions. *Nature*, **455**, 648-651, 2008.

[26] C. Durkan and M. E. Welland. Electronic Spin Detection in Molecules Using Scanning-Tunneling-Microscopy-Assisted Electron-Spin Resonance. *Appl. Phys. Lett.*, **80**, 458, 2002.

[27] B. Chesca, R. Kleiner and D. Koelle. *SQUID Theory, volume 1: Fundamentals and Technology of SQUIDs and SQUID Systems.* Chapter 2, 29-92. Wiley-VCH, Weinheim, 2004.

[28] W. Wernsdorfer. From Micro- to Nano-SQUIDs: Applications to Nanomagnetism. *Supercond. Sci. Technol.*, **22**, 064013, 2009.

[29] J. Gallop. *SQUIDs: Some Limits to Measurement. Supercond. Sci. Technol.*, **16**, 1575-1582, 2003.

[30] R. C. Jaklevic, J. Lambe, A. H. Silver and J. E. Mercereau. Quantum Interference Effects in Josephson Tunneling. *Phys. Rev. Lett.*, **12**, 159, 1964.

[31] J. E. Zimmermann, P. Thiene and J. T. harding. Design and Operation of Stable rf-Biased Superconducting Point-Contact Quantum Devices. *J. Appl. Phys.*, **41**, 1572, 1970.

[32] B. D. Josephson. The Discovery of Tunnelling Supercurrents. *Rev. Mod. Phys.*, **46**, 251-254, 1974.

[33] R. F. Voss, R. B. Laibowitz and A. N. Broers. Niobium Nanobridge dc SQUID. *Appl. Phys. Lett.*, **37**, 656-658, 1980.

[34] A. G. P. Troeman, H. Derking, B. Borger, J. Pleikies, D. Veldhuis and H. Hilgenkamp. NanoSQUIDs Based on Niobium Constrictions. *Nano Lett.*, **7**, 2152-2156, 2007.

[35] C. Granata, E. Esposito, A. Vettoliere, L. Petti and M. Russo. An Integrated Superconductive Magnetic Nanosensor for High-Sensitivity Nanoscale Applications. *Nanotechnology*, **19**, 275501, 2008.

[36] V. Bouchiat. Detection of Magnetic Moments Using a Nano-SQUID: Limits of Resolution and Sensitivity in Near-Field SQUID Magnetometry. *Supercond. Sci. Technol.*, **22**, 064002, 2009.

[37] D. L. Tilbrook. NanoSQUID Sensitivity for Isolated Dipoles and Small Spin Populations. *Supercond. Sci. Technol.*, **22**, 064003, 2009.

[38] P. F. Vohralik and S. K. H. Lam. NanoSQUID Detection of Magnetization from Ferritin Nanoparticles. *Supercond. Sci. Technol.*, **22**, 064007, 2009.

[39] J. Bardeen and M. J. Stephen. Theory of the Motion of Vortices in Superconductors. *Phys. Rev.*, **140**, A1197, 1965.

[40] M. Faucher, P.-O. Jubert, O. Fruchart, W. Wernsdorfer and V. Bouchiat. Optimizing the Flux Coupling Between a NanoSQUID and a Magnetic Particle Using Atomic Force Microscope Nanolithography. *Supercond. Sci. Technol.*, **22**, 064010, 2009.

[41] P. Meservey and P. M. Tedrow. Measurements of the Kinetic Inductance of Superconducting Linear Structures . *J. Appl. Phys.*, **40**, 2028, 1969.

[42] D. D. Awschalom, J. R. Rozen, M. B. Ketchen, W. J. Gallagher, A. W. Kleinsasser, R. L. Sandstrom, B. Bumble. Low-Noise Modular Microsusceptometer Using Nearly Quantum Limited dc SQUIDs. *Appl. Phys. Lett.*, **53**, 2108-2110, 1988.

[43] S. K. H. Lam. Noise Properties of SQUIDs Made from Nanobridges. *Supercond. Sci. Technol.*, **19**, 963-967, 2006.

[44] M. Ketchen, D. Awschalom, W. Gallagher, A. Kleinsasser, R. Sandstrom, J. Rozen, B. Bumble. Design, Fabrication, and Performance of Integrated Miniature SQUID Susceptometers. *IEEE Trans. Magn.*, **25**, 1212-1215, 1989.

[45] K. Hasselbach, D. Mailly and J. R. Kirtley. Micro-Superconducting Quantum Interference Device Characteristics. *J. Appl. Phys.*, **91**, 4432-4437, 2002.

[46] S. K. H. Lam and D. L. Tilbrook. Development of a Niobium Nanosuperconducting Quantum Interference Device for the Detection of Small Spin Populations. *Appl. Phys. Lett.*, **82**, 1078-1080, 2003.

[47] J.-P. Cleuziou, W. Wernsdorfer, V. Bouchiat, T. Ondarçuhu and M. Monthioux. Carbon Nanotube Superconducting Quantum Interference Device. *Nature Nanotech.*, **1**, 53-59, 2006.

[48] N. C. Koshnick, M. E. Huber, J. A. Bert, C. W. Hicks, J. Large, H. Edwards and K. A. Moler. A Terraced Scanning Super Conducting Quantum Interference Device Susceptometer with Submicron Pickup Loops. *Appl. Phys. Lett.*, **93**, 243101, 2008.

[49] L. Hao, J. C. Macfarlane, J. C. Gallop, D. Cox, J. Beyer, D. Drung and T. Schurig. Measurement and Noise Performance of Nano-Superconducting-Quantum-Interference Devices Fabricated by Focused Ion Beam. *Appl. Phys. Lett.*, **92**, 192507, 2008.

[50] C. P. Foley and H. Hilgenkamp. Why NanoSQUIDs Are Important: An Introduction to the Focus Issue. *Supercond. Sci. Technol.*, **22**, 064001, 2009.

[51] F. Giazotto, J. T. Peltonen, M. Meschke and Jukka P. Pekola. Superconducting Quantum Interference Proximity Transistor. *Nature Phys.*, **6**, 254-259, 2010.

[52] M. J. Martínez-Pérez, E. Bellido, R. de Miguel, J. Sesé, A. Lostao, C. Gómez-Moreno, D. Drung, T. Schurig, D. Ruiz-Molina and F. Luis. Alternating Current Magnetic Susceptibility of a Molecular Magnet Submonolayer Directly Patterned onto a Micro Superconducting Quantum Interference Device. *Appl. Phys. Lett.*, **99**, 032504, 2011.

[53] E. J. Romans, S. Rozhko, L. Young, A. Blois, L. Hao, D. Cox and J. C. Gallop. Noise Performance of Niobium Nano-SQUIDs in Applied Magnetic Fields. *IEEE Trans. Appl. Supercond.*, **21**, 404-407, 2011.

[54] R. Russo, C. Granata, E. Esposito, D. Peddis, C. Cannas and A. Vettoliere. Nanoparticle Magnetization Measurements by a High Sensitive Nano-Superconducting Quantum Interference Device. *Appl. Phys. Lett.*, **101**, 122601, 2012.

[55] C. Granata, A. Vettoliere, R. Russo, M. Fretto, N. De Leo and V. Lacquaniti. Three-Dimensional Spin Nanosensor Based on Reliable Tunnel Josephson Nano-Junctions for Nanomagnetism Investigations. *Appl. Phys. Lett.*, **103**, 102602, 2013.

[56] D. Drung, J.-H. Storm, F. Ruede, A. Kirste, M. Regin, T. Schurig, A. M. Repollés, J. Sesé and F. Luis. Thin-Film Microsusceptometer with Integrated Nanoloop. *IEEE Trans. Appl. Supercond.*, **24**, 1600206, 2014.

[57] R. Arpaia, M. Arzeo, S. Nawaz, S. Charpentier, F. Lombardi and T. Bauch. Ultra Low Noise $YBa_2Cu_3O_{7-\delta}$ Nano Superconducting Quantum Interference Devices Implementing Nanowires. *App. Phys. Lett.*, **104**, 072603, 2014.

[58] L. Chen, W. Wernsdorfer, C. Lampropoulos, G. Christou, I. Chiorescu. On-Chip SQUID Measurements in the Presence of High Magnetic Fields. *Nanotechnology*, **21**, 405504, 2010.

[59] A. Finkler, Y. Segev, Y. Myasoedov, M. L. Rappaport, L. Ne'eman, D. Vasyukov, E. Zeldov, M. E. Huber, J. Martin and A. Yacoby. Self-Aligned Nanoscale SQUID on a Tip. *Nano Lett.*, **10**, 1046-1049, 2010.

[60] D. Vasyukov, Y. Anahory, L. Embon, D. Halbertal, J. Cuppens, L. Ne'eman, A. Finkler, Y. Segev, Y. Myasoedov, M. L. Rappaport, M. E. Huber and E. Zeldov. A Scanning Superconducting Quantum Interference Device with Single Electron Spin Sensitivity. *Nature Nanotechnol.*, **8**, 639-644, 2013.

[61] Y. Anahory, J. Reiner, L. Embon, D. Halbertal, A. Yakovenko, Y. Myasoedov, M. L. Rappaport, M. E. Huber and E. Zeldov. Three-Junction SQUID-on-Tip with Tunable In-Plane and Out-of-Plane Magnetic Field Sensitivity. *Nano Letters*, **14**, 6481-6487, 2014.

[62] J. Nagel, O. F. Kieler, T. Weimann, R. Wölbing, J. Kohlmann, A. B. Zorin, R. Kleiner, D. Koelle and M. Kemmler. Superconducting Quantum Interference Devices with Submicron Nb/HfTi/Nb Junctions for Investigation of Small Magnetic Particles. *Appl. Phys. Lett.*, **99**, 032506, 2011.

[63] R. Wölbing, J. Nagel, T. Schwarz, O. Kieler, T. Weimann, J. Kohlmann, A. B. Zorin, M. Kemmler, R. Kleiner and D. Koelle. Nb Nano Superconducting Quantum Interference Devices with High Spin Sensitivity for Operation in Magnetic Fields up to 0.5 T. *Appl. Phys. Lett.*, **102**, 192601, 2013.

[64] J. Nagel, A. Buchter, F. Xue, O. F. Kieler, T. Weimann, J. Kohlmann, A. B. Zorin, D. Rüffer, E. Russo-Averchi, R. Huber, P. Berberich, A. Fontcuberta i Morral, D. Grundler, R. Kleiner, D. Koelle, M. Poggio and M. Kemmler. Nanoscale Multifunctional Sensor Formed by a Ni Nanotube and a Scanning Nb NanoSQUID. *Phys. Rev. B*, **88**, 064425, 2013.

[65] A. Buchter, J. Nagel, D. Rüffer, F. Xue, D. P. Weber, O. F. Kieler, T. Weimann, J. Kohlmann, A. B. Zorin, E. Russo-Averchi, R. Huber, P. Berberich, A. Fontcuberta i Morral, M. Kemmler, R. Kleiner, D. Koelle, D. Grundler and M. Poggio. Reversal Mechanism of an Individual Ni Nanotube Simultaneously Studied by Torque and SQUID Magnetometry. *Phys. Rev. Lett.*, **111**, 067202, 2013.

[66] D. Hagedorn, R. Dolata, F.-Im. Buchholz and J. Niemeyer. Properties of SNS Josephson Junctions with HfTi layers. *Physica C*, **7**, 372-376, 2002.

[67] D. Hagedorn, O. Kieler, R. Dolata, R. Behr, F. Müller, J. Kohlmann and J. Niemeyer. Modified Fabrication of Planar Sub-μm Superconductor-Normal Metal-Superconductor Josephson Junctions for Use in a Josphson Arbitrary Waveform Synthesizer. *Supercond. Sci. Technol.*, **19**, 294-298, 2006.

[68] D. Koelle, R. Kleiner, F. Ludwig, E. Dantsker, John Clarke. High-Transition-Temperature Superconducting Quantum Interference Devices. *Rev. Mod. Phys.*, **71**, 631-686, 1999.

[69] J. Nagel, K. B. Konovalenko, M. Kemmler, M. Turad, R. Werner, E. Kleisz, S. Menzel, R. Klingeler, B. Büchner, R. Kleiner and D. Koelle. Resistively Shunted $YBa_2Cu_3O_7$ Grain Boundary Junctions and Low-Noise SQUIDs Patterned by a Focused Ion Beam down to 80 nm Linewidth. *Supercond. Sci. Technol.*, **24**, 015015, 2011.

[70] T. Schwarz, J. Nagel, R. Wölbing, M. Kemmler, R. Kleiner and D. Koelle. Low-Noise Nano Superconducting Quantum Interference Device Operating in Tesla Magnetic Fields. *ACS Nano*, **7**, 844-850, 2013.

[71] R. Wölbing, T. Schwarz, B. Müller, J. Nagel, M. Kemmler, R. Kleiner and D. Koelle. Optimizing the Spin Sensitivity of Grain Boundary Junction NanoSQUIDs – Towards Detection of Small Spin Systems with Single-Spin Resolution. *Supercond. Sci. Technol.*, **27**, 125007, 2014.

[72] M. Rudolph, J. Nagel, J. M. Meckbach, M. Kemmler, M. Siegel, K. Ilin, D. Koelle and R. Kleiner. Direct Current Superconducting Quantum Interferometers with Asymmetric Shunt Resistors. *Appl. Phys. Lett.*, **101**, 052602, 2012.

[73] D. Drung and M. Mück. *SQUID Electronics, volume 1: Fundamentals and Technology of SQUIDs and SQUID Systems.* chapter 4, 127-170. Whiley-VCH, Weinheim, 2004.

[74] M. Khapaev, M. Kupriyanov, E. Goldobin and M. Siegel. Current Distribution Simulation for Superconducting Multi-Layered Structures. *Supercond. Sci. Technol.*, **16**, 24-27, 2003.

[75] R. H. Koch, D. P. DiVincenzo and J. Clarke. Model for $1/f$ Flux Noise in SQUIDs and Qubits. *Phys. Rev. Lett.*, **98**, 267003, 2007.

[76] D. C. Joy. *Helium Ion Microscopy.* Chapter 8, 51-53. SpringerBriefs in Materials, 2013.

[77] K. Potzger, J.Osten, A. A.Levin, A.Shalimov, G.Talut, H.Reuther, S.Arpaci, D. Bürger,H. Schmidt, T.Nestler and D. C.Meyer. Defect-Induced Ferromagnetism in Crystalline $SrTiO_3$. *J. Magn. Magn. Mater.*, **323**, 1551-1562, 2011.

[78] R. de Sousa. Dangling-Bond Spin Relaxation and Magnetic $1/f$ Noise from the Amorphous-Semiconductor/Oxide Interface: Theory. *Phys. Rev. B*, **76**, 245306, 2007.

[79] S. Sendelbach, D. Hover, A. Kittel, M. Mück, John M. Martinis and R. McDermott. Magnetism in SQUIDs at Millikelvin Temperatures. *Phys. Rev. Lett.*, **100**, 227006, 2008.

[80] A. Winkler, T. Mühl, S. Menzel, R. Kozhuharova-Koseva, S. Hampel, A. Leonhardt and B. Büchner. Magnetic Force Microscopy Sensors Using Iron-Filled Carbon Nanotubes. *J. Appl. Phys.*, **99**, 104905, 2006.

[81] A. Leonhardt, S. Hampel, C. Müller, I. Mönch, R. Koseva, M. Ritschel, D. Elefant, K. Biedermann and B. Büchner. Synthesis, Properties, and Applications of Ferromagnetic-Filled Carbon Nanotubes. *Chem. Vap. Deposition*, **12**, 380-387, 2006.

[82] T. Mühl, J. Körner, S. Philippi, C. F. Reiche, A. Leonhardt and B. Büchner. Magnetic Force Microscopy Sensors Providing In-Plane and Perpendicular Sensitivity. *App. Phys. Lett.*, **101**, 112401, 2012.

[83] K. Lipert, S. Bahr, F. Wolny, P. Atkinson, U. Weißker, T. Mühl, O. G. Schmidt, B. Büchner and R. Klingeler. An Individual Iron Nanowire-Filled Carbon Nanotube Probed by Micro-Hall Magnetometry. *App. Phys. Lett.*, **97**, 212503, 2010.

[84] D. Drung, J. Beyer, J.-H. Storm, M. Peters and T. Schurig. Investigation of Low-Frequency Excess Flux Noise in dc SQUIDs at mK Temperatures. *IEEE Trans. Appl. Supercond.*, **21**, 340-344, 2011.

[85] E. Sassier, R. Kleiner and D. Koelle. A Spectroscopic Method for Excess-Noise Spectrum Analysis. Unpublished.

[86] D. P. Weber, D. Rüffer, A. Buchter, F. Xue, E. Russo-Averchi, R. Huber, P. Berberich, J. Arbiol, A. Fontcuberta i Morral, D. Grundler and M. Poggio. Cantilever Magnetometry of Individual Ni Nanotubes. *Nano Lett.*, **12**, 6139-6144, 2012.

[87] S. J. Son, J. Reichel, B. He, M. Schuchman and S. B. Lee. Magnetic Nanotubes for Magnetic-Field-Assisted Bioseparation, Biointeraction, and Drug Delivery. *J. Am. Chem. Soc.*, **127**, 7316-7317, 2005.

[88] K. Nielsch, F. J. Castano, S. Matthias, W. Lee and C. A. Ross. Synthesis of Cobalt/Polymer Multilayer Nanotubes. *Adv. Eng. Mater.*, **7**, 217-221, 2005.

[89] Z. K. Wang, H. S. Lim, H. Y. Liu, S. C. Ng, M. H. Kuok, L. L. Tay, D. J. Lockwood, M. G. Cottam, K. L. Hobbs, P. R. Larson, J. C. Keay, G. D. Lian and M. B. Johnson. Spin Waves in Nickel Nanorings of Large Aspect Ratio. *Phys. Rev. Lett.*, **94**, 137208, 2005.

[90] R. Hertel and J. Kirschner. Resonant Modes of Vortex Structures in Soft-Magnetic Nanodiscs. *J. Magn. Magn. Mater.*, **272**, 655-656, 2004.

[91] D. Rüffer. *Magnetic States and Spin-Wave Modes in Single Ferromagnetic Nanotubes.* PhD thesis. Lausanne, EPFL, 2014.

[92] P. Landeros, O. J. Suarez, A. Cuchillo and P. Vargas. Equilibrium States and Vortex Domain Wall Nucleation in Ferromagnetic Nanotubes. *Phys. Rev. B*, **79**, 024404, 2009.

[93] X. M. Liu, J. Ding and A. O. Adeyeye. Exchange Bias Effect in $Ni_{80}Fe_{20}$/CoO Bi-Component Nanowires. *EPL*, **108**, 17003, 2014.

[94] N. J. Gökemeijer, J. W. Cai and C. L. Chien. Memory Effects of Exchange Coupling in Ferromagnet/Antiferromagnet Bilayers. *Phys. Rev. B*, **60**, 3033, 1999.

[95] S. Giri, M. Patra and S. Majumdar. Exchange Bias Effect in Alloys and Compounds. *J. Phys.: Condens. Matter*, **23**, 073201, 2011.

[96] S. Brems, K. Temst and C. van Haesendonck. Origin of the Training Effect and Asymmetry of the Magnetization in Polycrystalline Exchange Bias Systems. *Phys. Rev. Lett.*, **99**, 067201, 2007.

[97] T. Hauet, J. A. Borchers, Ph. Mangin, Y. Henry and S. Mangin. Training Effect in an Exchange Bias System: The Role of Interfacial Domain Walls. *Phys. Rev. Lett.*, **96**, 067207, 2006.

[98] C. Binek. Training of the Exchange-Bias Effect: A Simple Analytic Approach. *Phys. Rev. B*, **70**, 014421, 2004.

[99] A. Hoffmann. Symmetry Driven Irreversibilities at Ferromagnetic-Antiferromagnetic Interfaces. *Phys. Rev. Lett.*, **93**, 097203, 2004.

[100] M. D. Stiles and R. D. McMichael. Temperature Dependence of Exchange Bias in Polycrystalline Ferromagnet-Antiferromagnet Bilayers. *Phys. Rev. B*, **60**, 12950, 1999.

[101] M. Ali, C. H. Marrows, M. Al-Jawad, B. J. Hickey, A. Misra, U. Nowak and K. D. Usadel. Antiferromagnetic Layer Thickness Dependence of the IrMn/Co Exchange-Bias System. *Phys. Rev. B*, **68**, 214420, 2003.

[102] P. J. van der Zaag, Y. Ijiri, J. A. Borchers, L. F. Feiner, R. M. Wolf, J. M. Gaines, R. W. Erwin and M. A. Verheijen. Difference Between Blocking and Néel Temperatures in the Exchange Biased Fe_3O_4/CoO System. *Phys. Rev. Lett.*, **84**, 6102, 2000.

[103] C. Binek, X. He and S. Polisetty. Temperature Dependence of the Training Effect in a Co/CoO Exchange-Bias Layer. *Phys. Rev. B*, **72**, 054408, 2005.

[104] E. H. Brandt. Thin Superconductors and SQUIDs in Perpendicular Magnetic Field. *Phys. Rev. B*, **72**, 024529, 2005.

[105] M. M. Khapaev. Extraction of Inductances of Plane Thin Film Superconducting Circuits. *Supercond. Sci. Technol.*, **10**, 389-394, 1997.

Appended publications

Publication 1

Nb nano superconducting quantum interference devices with high spin sensitivity for operation in magnetic fields up to 0.5 T

R. Wölbing,[1] J. Nagel,[1] T. Schwarz,[1] O. Kieler,[2] T. Weimann,[2] J. Kohlmann,[2] A. B. Zorin,[2] M. Kemmler,[1] R. Kleiner,[1] and D. Koelle[1]
[1]*Physikalisches Institut – Experimentalphysik II and Center for Collective Quantum Phenomena in LISA*$^+$, *Universität Tübingen, Auf der Morgenstelle 14, D-72076 Tübingen, Germany*
[2]*Fachbereich 2.4 "Quantenelektronik," Physikalisch-Technische Bundesanstalt, Bundesallee 100, D-38116 Braunschweig, Germany*

(Received 10 April 2013; accepted 27 April 2013; published online 14 May 2013)

We investigate electric transport and noise properties of microstrip-type submicron direct current superconducting quantum interference devices (dc SQUIDs) based on Nb thin films and overdamped Josephson junctions with a HfTi barrier. The SQUIDs were designed for optimal spin sensitivity $S_\mu^{1/2}$ upon operation in intermediate magnetic fields B (tens of mT), applied perpendicular to the substrate plane. Our, so far, best SQUID can be continuously operated in fields up to $B \approx \pm 50\,\mathrm{mT}$ with rms flux noise $S_{\Phi,\mathrm{w}}^{1/2} \leq 250\,\mathrm{n}\Phi_0/\mathrm{Hz}^{1/2}$ in the white noise regime and spin sensitivity $S_\mu^{1/2} \leq 29\,\mu_\mathrm{B}/\mathrm{Hz}^{1/2}$. Furthermore, we demonstrate operation in $B = 0.5\,\mathrm{T}$ with high sensitivity in flux $S_{\Phi,\mathrm{w}}^{1/2} \approx 680\,\mathrm{n}\Phi_0/\mathrm{Hz}^{1/2}$ and in electron spin $S_\mu^{1/2} \approx 79\,\mu_\mathrm{B}/\mathrm{Hz}^{1/2}$. We discuss strategies to further improve the nanoSQUID performance. © *2013 AIP Publishing LLC*. [http://dx.doi.org/10.1063/1.4804673]

Recent developments in miniaturized submicron-sized direct current (dc) superconducting quantum interference devices (SQUIDs) are motivated by the need of sensitive detectors for small spin systems such as molecular magnets[1–3] and magnetic nanoparticles,[4] cold atom clouds,[5] or single electrons and atoms[6] and improved resolution in scanning SQUID microscopy.[7–12] As a common approach, nanoSQUIDs based on constriction Josephson junctions (JJs) have been used,[13–19] achieving root mean square (rms) flux noise power $S_\Phi^{1/2}$ down to a few $100\,\mathrm{n}\Phi_0/\mathrm{Hz}^{1/2}$ (Φ_0 is the magnetic flux quantum) in magnetically shielded environment.[20] However, constriction JJs, even if resistively shunted, often show hysteretic current-voltage-characteristics (IVCs). This hampers continuous SQUID operation as required for the investigation of magnetization dynamics of magnetic particles and the use of common SQUID electronics, developed for readout of very sensitive dc SQUIDs with nonhysteretic JJs. Furthermore, the noise properties of constriction JJs are not well understood, which makes SQUID optimization difficult.

An alternative approach is the use of submicron superconductor-normal conductor-superconductor (SNS) sandwich-type JJs, which offer large critical current densities in the $10^5\,\mathrm{A/cm}^2$ range and which are intrinsically shunted, providing nonhysteretic IVCs without the need of bulky external shunt resistors.[21] In a standard thin film SQUID geometry, the SQUID loop and the JJ barrier are in the plane of the thin films. For detection of magnetization reversal of a small magnetic particle, one applies an external magnetic field in the plane of the SQUID loop and detects the change of the stray field coupled to the SQUID upon magnetization reversal, without coupling the external field to the SQUID. However, in this case, the applied field also couples magnetic flux into the JJ barrier and reduces its critical current, which in turn reduces the SQUID sensitivity. In order to avoid this problem, in this letter we present results on a modified SQUID design, which takes advantage of the multilayer technology used for SNS JJ fabrication. This approach allows for a further reduction of the SQUID inductance and hence improved SQUID sensitivity and at the same time operation in higher magnetic fields.

The Nb thin film dc SQUIDs have a microstrip geometry, i.e., the two 250 nm wide arms of the SQUID loop lie directly on top of each other. The 200 nm thick bottom and 160 nm thick top Nb layers are separated by a 225 nm thick insulating SiO_2 layer and are connected via two JJs with areas $200 \times 200\,\mathrm{nm}^2$ and a nominally 24 nm thick HfTi barrier (see Fig. 1). HfTi was chosen as a barrier material as, among other binary materials, it provides a relatively high resistivity, does not become superconducting at 4.2 K, and is compatible with our fabrication technology. For details on sample fabrication and JJ properties we refer to Refs. 21–23. The size of the SQUID loop is defined by the 1.6 μm spacing between the JJs and by the SiO_2 interlayer thickness. In contrast to earlier work,[21] for this geometry a sufficiently large magnetic field B can be applied perpendicular to the substrate plane without inducing a significant magnetic flux penetrating either the SQUID loop or the junction barrier. Furthermore, this design provides a very small area of the SQUID loop and hence a very small SQUID inductance L of a few pH or even lower. This is essential for reaching ultralow values for the spectral density of flux noise power S_Φ.[24]

For current and flux biasing, additional 250 nm wide Nb lines are connecting the SQUID in a cross-shape geometry, and a bias current I_b, flowing from the top Nb layer through the JJs to the bottom Nb layer, can be applied either in a symmetric or asymmetric configuration (see Fig. 1). For simplified readout we use asymmetric current bias in the following. A magnetic flux Φ can be coupled into the SQUID loop by applying a modulation current I_mod across the bottom Nb layer ("flux bias line"). This enables flux biasing the SQUIDs at the optimum working point without the need of

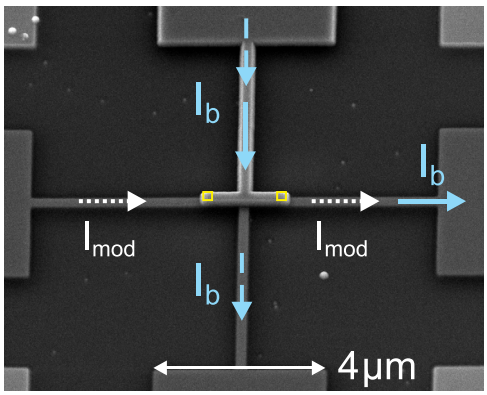

FIG. 1. Scanning electron microscopy (SEM) image of SQUID 2. Open (yellow) squares indicate positions of JJs. Arrows indicate current paths for bias current I_b (dashed: symmetric bias; solid: asymmetric bias) and modulation current I_{mod} (dotted).

an external coil. Furthermore, the flux bias line can also be used to provide a feedback flux for SQUID operation in a flux locked loop. However, in this work, the SQUIDs were always read out open loop.

We investigated various SQUIDs which were fabricated in two different runs on separate wafers. Below we present results for two devices, SQUID 1 from wafer 1 and SQUID 2 from wafer 2. The main difference in the design of these devices is the different lengths $\sim 2.5\,\mu$m (SQUID 1) and $\sim 5\,\mu$m (SQUID 2) of the narrow bias lines, running from the center of the SQUID to the $4\,\mu$m wide connection lines further away from the SQUID (cf., Fig. 1). This variation has a strong impact on the SQUID performance in applied magnetic fields, as will be shown below.

All data were taken at temperature $T = 4.2\,$K. We first present results of transport and noise measurements of the two SQUIDs in an electrically and magnetically shielded environment. Since both devices showed qualitatively the same behavior, we only give a detailed analysis of SQUID 2 and summarize the main parameters extracted for both devices in Table I. Regarding absolute values, a major difference between both devices are the values for maximum critical current I_c and normal resistance R_N, which probably is due to variations in the HfTi barrier thickness for the devices fabricated in different runs. Devices fabricated from the same run showed a spread in I_c and R_N values of $\pm 10\,\%$.

Figure 2(a) shows IVCs of SQUID 2 for $\Phi/\Phi_0 = 0$, 1/4, and 1/2. The IVCs are nonhysteretic with $I_c = 227\,\mu$A and $R_N = 250\,\text{m}\Omega$, yielding a characteristic voltage $V_c \equiv I_c R_N = 57\,\mu$V. The IVC at $\Phi/\Phi_0 = 1/2$ exhibits a small bump for low voltages. This bump appears in all our devices and is presumably a property of the quasiparticle current rather than a *LC* resonance of the SQUID. The inset of Fig. 2(a) shows the modulation $I_c(I_{mod})$ for positive and negative bias current.

TABLE I. Parameters of SQUID 1 and SQUID 2.

	I_c (μA)	R_N (mΩ)	I_cR_N (μV)	β_L	L (pH)	M_i^{-1} $\left(\frac{\text{mA}}{\Phi_0}\right)$	V_Φ $\left(\frac{\mu\text{V}}{\Phi_0}\right)$	$S_{\Phi,w}^{1/2}$ $\left(\frac{\text{n}\Phi_0}{\text{Hz}^{1/2}}\right)$
SQUID 1	129	385	50	0.19	3.0	2.63	154	260
SQUID 2	227	250	57	0.25	2.3	2.73	164	200

From the modulation period we obtain the inverse mutual inductance $M_i^{-1} = 2.73\,\text{mA}/\Phi_0$. From the modulation depth we find a screening parameter $\beta_L \equiv 2I_0L/\Phi_0 = 0.25$. By assuming that both JJs are identical, i.e., $I_c \equiv 2I_0$, we determine the SQUID inductance $L = 2.3\,$pH.

The $V(I_{mod})$ modulation for different bias currents, plotted in the inset of Fig. 2(b), yields a maximum transfer function $V_\Phi \equiv \partial V/\partial\Phi = 164\,\mu\text{V}/\Phi_0$ for $I_b = 230\,\mu$A. The shift in $I_c(I_{mod})$ and $V(I_{mod})$ for positive and negative bias currents can be attributed to the asymmetric current bias, which leads to an inductance asymmetry $\alpha_L \equiv (L_2 - L_1)/(L_1 + L_2)$; here L_1 and L_2 are the inductances of the two SQUID arms. The measured $I_c(I_{mod})$-characteristics are fitted well by numerical simulations based on coupled Langevin equations[25] with a noise parameter $\Gamma \equiv 2\pi k_B T/I_0\Phi_0 = 1.55 \cdot 10^{-3}$ (k_B is the Boltzmann constant) and $\alpha_L = -0.35$ (see inset of Fig. 2(a), dotted lines).

Using a commercial SQUID amplifier with a voltage noise $S_V^{1/2} \approx 40\,\text{pV}/\text{Hz}^{1/2}$ and a $-3\,$dB cutoff frequency $f_c \approx 30\,$kHz, we measured the spectral density of the rms flux noise $S_\Phi^{1/2}(f) \equiv S_V^{1/2}(f)/|V_\Phi|$ at the optimum working point (see solid line in Fig. 2(b)). Here the SQUID amplifier contribution was subtracted. We observe a significant low-frequency excess noise, which we assign to I_0 fluctuations in the JJs. Since the low-frequency excess noise extends to well

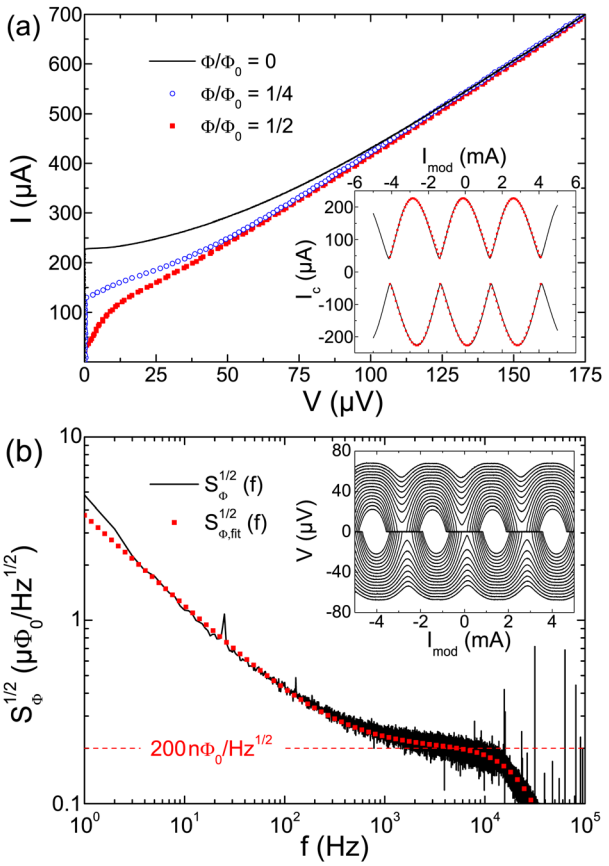

FIG. 2. Transport and noise characteristics of SQUID 2. (a) IVCs for different flux Φ; inset shows measurement (solid black lines) and numerical simulation (dotted red lines) of $I_c(I_{mod})$. (b) Solid black line: Spectral density of rms flux noise $S_\Phi^{1/2}(f)$ at optimum working point ($I_b = 230\,\mu$A, $I_{mod} = 243\,\mu$A). Dotted (red) line: fitted spectrum; dashed (red) line indicates white noise level for fitted curve. Inset shows $V(I_{mod})$ for $I_b = \pm(150\ldots300)\,\mu$A (in $10\,\mu$A steps).

above 1 kHz and due to the limited bandwidth of the SQUID amplifier, we do not see a clear white noise region in the spectrum. By fitting the experimental data (dotted line in Fig. 2(b)), we derive a low-frequency noise contribution $S_{\Phi,f}^{1/2} \propto 1/f^{\alpha}$ with $\alpha = 0.5$ and $S_{\Phi,f}^{1/2}(f = 1\,\mathrm{Hz}) = 3.7\,\mu\Phi_0/\mathrm{Hz}^{1/2}$ and a white noise contribution $S_{\Phi,\mathrm{w}}^{1/2} = 200\,\mathrm{n}\Phi_0/\mathrm{Hz}^{1/2}$ (dashed line in Fig. 2(b)).

In order to determine the spin sensitivity $S_{\mu}^{1/2} \equiv S_{\Phi}^{1/2}/\phi_{\mu}$ of our SQUIDs, we calculated the coupling factor ϕ_{μ}, using a routine based on the numerical solution of the London equations for the given SQUID geometry.[26] Here, $\phi_{\mu} \equiv \Phi/\mu$ is the magnetic flux Φ per magnetic moment $|\vec{\mu}| \equiv \mu$ coupled by a magnetic particle to the SQUID loop. Very recently, the validity of this approach has been verified experimentally by measuring the magnetic coupling of a Ni nanotube to a Nb nanoSQUID which had the same geometry as SQUID 2.[27] For a point-like magnetic particle with $\vec{\mu}$ perpendicular to the substrate plane, placed at a lateral distance of 10 nm from the lower edge of the upper Nb SQUID arm at the center of the loop, we obtain $\phi_{\mu} = 8.6\,\mathrm{n}\Phi_0/\mu_B$ (μ_B is the Bohr magneton). Along with the obtained value of the rms flux noise $S_{\Phi,\mathrm{w}}^{1/2} = 200\,\mathrm{n}\Phi_0/\mathrm{Hz}^{1/2}$ we calculate the spin sensitivity to $S_{\mu}^{1/2} = 23\,\mu_B/\mathrm{Hz}^{1/2}$.

To investigate the SQUID performance in a magnetic field B applied perpendicular to the substrate plane we mounted SQUID 1 on a high-precision alignment system (one rotator, two goniometers). B is generated by a superconducting split coil running in persistent mode to suppress field noise.[28] Figure 3(a) shows $I_c(B)$ for SQUID 1 after the alignment process for a field sweep sequence as indicated by labels 0–6. The observed hysteresis for $|B| < 45\,\mathrm{mT}$ is ascribed to entry and trapping of Abrikosov vortices in the 4 μm wide connection lines, cf., inset of Fig. 3(b). The steep jump in I_c at $B \approx 45\,\mathrm{mT}$ can be assigned to a vortex entering the narrow Nb leads very close to the SQUID loop, as confirmed recently by magnetic force microscopy on a similar Nb nanoSQUID (with layout of SQUID 2).[27] Subsequently, we reduced the linewidth of the connection lines of SQUID 1 from 4 μm to ~500 nm by focused ion beam (FIB) milling[28] (see inset of Fig. 3(b)). For the repatterned device, the maximum I_c was reduced by ~10%, probably due to a slight degradation of the JJs during FIB milling. More importantly, I_c became almost independent of B, and within $B \approx \pm 50\,\mathrm{mT}$ the magnetic hysteresis disappeared, cf., Fig. 3(b). At $B \approx 50\,\mathrm{mT}$ we still observed the jump in I_c due to vortex entry in the narrow Nb line close to the SQUID. This indicates that the linewidth of the Nb wiring close to the SQUID may limit the range of operation to $|B| \leq 50\,\mathrm{mT}$. However, as will be shown below, even after vortex entry, by proper realignment of the applied magnetic field direction, which compensates the stray magnetic flux induced by trapped vortices, I_c can be restored and low flux noise can be retained.

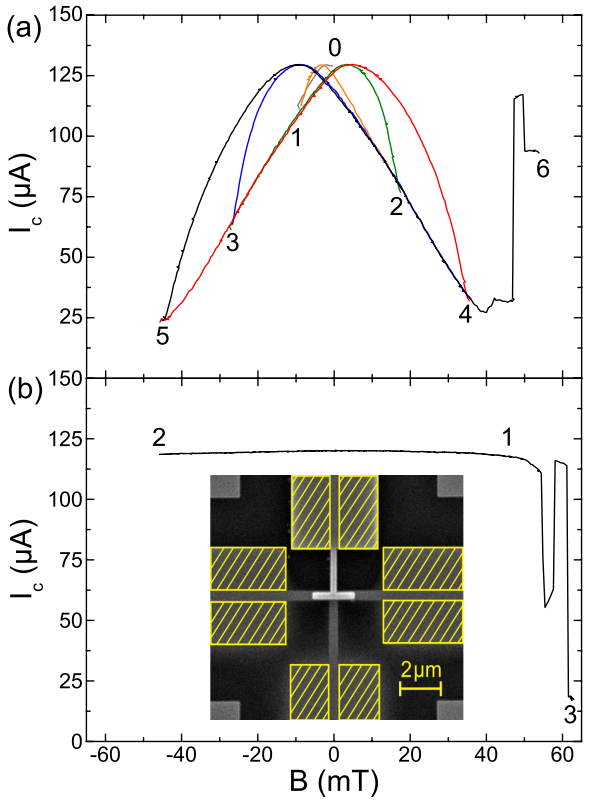

FIG. 3. $I_c(B)$ data of SQUID 1 for field sweep sequence 0–6 (a) and 1–3 (b) after removing Nb areas by FIB milling as indicated by hatched (yellow) rectangles in the inset (SEM image).

We now turn to SQUID 2, which has much longer narrow bias lines. Figure 4(a) shows $I_c(B)$ for a field sweep $46\,\mathrm{mT} \rightarrow -46\,\mathrm{mT} \rightarrow 55\,\mathrm{mT}$ (1–3). Again I_c is almost independent of B for $|B| \leq 50\,\mathrm{mT}$ and, as before, we find a jump in I_c at $B \approx 50\,\mathrm{mT}$ due to a vortex entering the narrow bias lines. The vortex can be removed by sweeping back the field as indicated by the curve (3–4) in Fig. 4(a).

For SQUID 2 we performed noise measurements as described above to determine $S_{\Phi,\mathrm{w}}^{1/2}$ at several values of B from 0 to 50 mT, without any jump in I_c (see inset of Fig. 4(a)). For $B = 0$, $S_{\Phi,\mathrm{w}}^{1/2} \approx 220\,\mathrm{n}\Phi_0/\mathrm{Hz}^{1/2}$, which is slightly higher than the value obtained in the low-field setup. We attribute this to external disturbances from the unshielded environment in the high-field setup (cf., noise spectrum in Fig. 4(b), black line). As indicated in the inset of Fig. 4(a), the white noise level increases only slightly with B to $S_{\Phi,\mathrm{w}}^{1/2} \approx 250\,\mathrm{n}\Phi_0/\mathrm{Hz}^{1/2}$ at $B = 50\,\mathrm{mT}$ (cf., noise spectrum in Fig. 4(b)), still corresponding to a very small spin sensitivity $S_{\mu}^{1/2} \approx 29\,\mu_B/\mathrm{Hz}^{1/2}$ (in the white noise regime). We assign this behavior to a minor decrease of I_c due to an imperfect alignment of the device relative to B. At $B = 55\,\mathrm{mT}$, i.e., after the jump in I_c occurred and after realigning the SQUID by maximizing I_c, we obtain a similar value $S_{\Phi,\mathrm{w}}^{1/2} \approx 240\,\mathrm{n}\Phi_0/\mathrm{Hz}^{1/2}$ as for $B = 50\,\mathrm{mT}$. Following the same procedure of realignment, we were able to operate the SQUID in magnetic fields up to $B = 0.5\,\mathrm{T}$, yielding the noise spectrum as shown in Fig. 4(b), with $S_{\Phi,\mathrm{w}}^{1/2} \approx 680\,\mathrm{n}\Phi_0/\mathrm{Hz}^{1/2}$, corresponding to $S_{\mu}^{1/2} \approx 79\,\mu_B/\mathrm{Hz}^{1/2}$. Note that all spectra feature excess low-frequency noise peaks, which are presumably due to mechanical vibrations of the setup.

In conclusion, we fabricated and investigated Nb nanoSQUIDs based on a trilayer geometry which were optimized for stable operation in comparatively large magnetic fields. Very low white flux noise values down to $S_{\Phi,\mathrm{w}}^{1/2} \approx 200\,\mathrm{n}\Phi_0/\mathrm{Hz}^{1/2}$ have been achieved in a shielded environment yielding a spin sensitivity $S_{\mu}^{1/2} \approx 23\,\mu_B/\mathrm{Hz}^{1/2}$. Concerning the suitability to applied magnetic fields, we

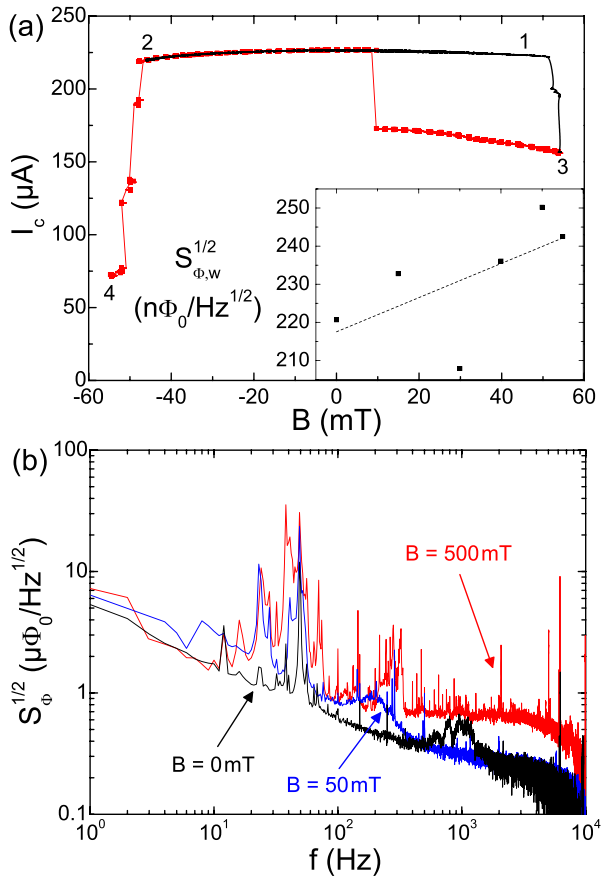

FIG. 4. (a) $I_c(B)$ data of SQUID 2 for field sweep sequence 1–3 (black solid line) and 3–4 (red line plus symbols). Inset: $S^{1/2}_{\Phi,w}(B)$ at optimum working point; dashed line is a linear fit. (b) Spectral density of rms flux noise $S^{1/2}_{\Phi}(f)$ for $B = 0$ mT, 50 mT, and 500 mT.

redesigned the layout of SQUID 1 via FIB milling and implemented these findings into the design of SQUID 2. We demonstrated stable operation in a field range of $B \approx \pm 50$ mT with a marginal increase in white flux noise and spin sensitivity with B ($S^{1/2}_{\Phi,w} \leq 250\,n\Phi_0/Hz^{1/2}$ and $S^{1/2}_{\mu} \leq 29\,\mu_B/Hz^{1/2}$). Moreover it was shown that SQUID 2 can maintain high sensitivity in large fields up to $B = 0.5$ T with $S^{1/2}_{\Phi,w} \approx 680\,n\Phi_0/Hz^{1/2}$ and $S^{1/2}_{\mu} \approx 79\,\mu_B/Hz^{1/2}$. An obvious way to further decrease $S^{1/2}_{\Phi}$ and $S^{1/2}_{\mu}$ is to lower the SQUID inductance L, which can be done easily by decreasing the lateral distance between the JJs and by reducing the thickness of the SiO_2 layer separating the top and bottom Nb layers. In addition, the width of the Nb lines can be reduced further to increase ϕ_μ and to extend the range of magnetic fields where the SQUID can be operated without vortices entering the wiring. All in all, we consider a spin sensitivity down to a few $\mu_B/Hz^{1/2}$, for a field range exceeding 100 mT, to be achievable for this type of device.

J. Nagel and T. Schwarz gratefully acknowledge support by the Carl-Zeiss-Stiftung. We thank K. Störr for assistance in device fabrication. This work was funded by the DFG via the SFB TRR 21 and by the ERC via SOCATHES.

[1]D. Gatteschi and R. Sessoli, Angew. Chem., Int. Ed. **42**, 268 (2003).
[2]W. Wernsdorfer, Nature Mater. **6**, 174 (2007).
[3]L. Bogani, A. Vindigni, R. Sessoli, and D. Gatteschi, J. Mater. Chem. **18**, 4750 (2008).
[4]W. Wernsdorfer, Adv. Chem. Phys. **118**, 99 (2001).
[5]J. Fortágh and C. Zimmermann, Science **307**, 860 (2005).
[6]P. Bushev, D. Bothner, J. Nagel, M. Kemmler, K. B. Konovalenko, A. Loerincz, K. Ilin, M. Siegel, D. Koelle, R. Kleiner, and F. Schmidt-Kaler, Eur. Phys. J. D **63**, 9 (2011).
[7]J. R. Kirtley, M. B. Ketchen, K. G. Staviasz, J. Z. Sun, W. J. Gallagher, S. H. Blanton, and S. J. Wind, Appl. Phys. Lett. **66**, 1138 (1995).
[8]R. Black, F. Wellstood, E. Dantsker, A. Miklich, D. Nemeth, D. Koelle, F. Ludwig, and J. Clarke, Appl. Phys. Lett. **66**, 99 (1995).
[9]C. Veauvy, K. Hasselbach, and D. Mailly, Rev. Sci. Instrum. **73**, 3825 (2002).
[10]J. R. Kirtley, Supercond. Sci. Technol. **22**, 064008 (2009).
[11]A. Finkler, Y. Segev, Y. Myasoedov, M. L. Rappaport, L. Neman, D. Vasyukov, E. Zeldov, M. E. Huber, J. Martin, and A. Yacoby, Nano Lett. **10**, 1046 (2010).
[12]A. Finkler, D. Vasyukov, Y. Segev, L. Néeman, E. O. Lachman, M. L. Rappaport, Y. Myasoedov, E. Zeldov, and M. E. Huber, Rev. Sci. Instrum. **83**, 073702 (2012).
[13]C. P. Foley and H. Hilgenkamp, Supercond. Sci. Technol. **22**, 064001 (2009).
[14]M. Faucher, P.-O. Jubert, O. Fruchart, W. Wernsdorfer, and V. Bouchiat, Supercond. Sci. Technol. **22**, 064010 (2009).
[15]L. Chen, W. Wernsdorfer, C. Lampropoulos, G. Christou, and I. Chiorescu, Nanotechnology **21**, 405504 (2010).
[16]E. J. Romans, S. Rozhko, L. Young, A. Blois, L. Hao, D. Cox, and J. C. Gallop, IEEE Trans. Appl. Supercond. **21**, 404 (2011).
[17]R. Russo, C. Granata, E. Esposito, D. Peddis, C. Cannas, and A. Vettoliere, Appl. Phys. Lett. **101**, 122601 (2012).
[18]N. Antler, E. M. Levenson-Falk, R. Naik, Y.-D. Sun, A. Narla, R. Vijay, and I. Siddiqi, arXiv:1303.2737.
[19]E. M. Levenson-Falk, R. Vijay, N. Antler, and I. Siddiqi, Supercond. Sci. Technol. **26**, 055015 (2013).
[20]L. Hao, J. C. Macfarlane, J. C. Gallop, D. Cox, J. Beyer, D. Drung, and T. Schurig, Appl. Phys. Lett. **92**, 192507 (2008).
[21]J. Nagel, O. F. Kieler, T. Weimann, R. Wölbing, J. Kohlmann, A. B. Zorin, R. Kleiner, D. Koelle, and M. Kemmler, Appl. Phys. Lett. **99**, 032506 (2011).
[22]D. Hagedorn, R. Dolata, F.-I. Buchholz, and J. Niemeyer, Physica C **372–376**, 7 (2002).
[23]D. Hagedorn, O. Kieler, R. Dolata, R. Behr, F. Müller, J. Kohlmann, and J. Niemeyer, Supercond. Sci. Technol. **19**, 294 (2006).
[24]D. J. Van Harlingen, R. H. Koch, and J. Clarke, Appl. Phys. Lett. **41**, 197 (1982).
[25]B. Chesca, R. Kleiner, and D. Koelle, "Fundamentals and technology of SQUIDs and SQUID systems," in *The SQUD Handbook*, edited by J. Clarke and A. I. Braginski (Wiley-VCH, Weinheim, 2004), Vol. 1, Chap. 2, pp. 29–92.
[26]J. Nagel, K. B. Konovalenko, M. Kemmler, M. Turad, R. Werner, E. Kleisz, S. Menzel, R. Klingeler, B. Büchner, R. Kleiner, and D. Koelle, Supercond. Sci. Technol. **24**, 015015 (2011).
[27]J. Nagel, A. Buchter, F. Xue, O. F. Kieler, T. Weimann, J. Kohlmann, A. B. Zorin, D. Rüffer, E. Russo-Averchi, R. Huber, P. Berberich, A. Fontcuberta i Morral, D. Grundler, R. Kleiner, D. Koelle, M. Poggio, and M. Kemmler, arXiv:1305.1195.
[28]T. Schwarz, J. Nagel, R. Wölbing, M. Kemmler, R. Kleiner, and D. Koelle, ACS Nano **7**, 844 (2013).

Publication 2

Low-Noise Nano Superconducting Quantum Interference Device Operating in Tesla Magnetic Fields

Tobias Schwarz, Joachim Nagel, Roman Wölbing, Matthias Kemmler, Reinhold Kleiner, and Dieter Koelle*

Physikalisches Institut—Experimentalphysik II and Center for Collective Quantum Phenomena in LISA$^+$, Universität Tübingen, Auf der Morgenstelle 14, D-72076 Tübingen, Germany

ABSTRACT Superconductivity in the cuprate $YBa_2Cu_3O_7$ (YBCO) persists up to huge magnetic fields (B) up to several tens of Teslas, and sensitive direct current (dc) superconducting quantum interference devices (SQUIDs) can be realized in epitaxially grown YBCO films by using grain boundary Josephson junctions (GBJs). Here we present the realization of high-quality YBCO nanoSQUIDs, patterned by focused ion beam milling. We demonstrate low-noise performance of such a SQUID up to $B = 1$ T applied parallel to the plane of the SQUID loop at the temperature $T = 4.2$ K. The GBJs are shunted by a thin Au layer to provide nonhysteretic current voltage characteristics, and the SQUID incorporates a 90 nm wide constriction which is used for on-chip modulation of the magnetic flux through the SQUID loop. The white flux noise of the device increases only slightly from 1.3 $\mu\Phi_0/(\mathrm{Hz})^{1/2}$ at $B = 0$ to 2.3 $\mu\Phi_0/(\mathrm{Hz})^{1/2}$ at 1 T. Assuming that a point-like magnetic particle with magnetization in the plane of the SQUID loop is placed directly on top of the constriction and taking into account the geometry of the SQUID, we calculate a spin sensitivity $S_\mu^{1/2} = 62\ \mu_B/(\mathrm{Hz})^{1/2}$ at $B = 0$ and 110 $\mu_B/(\mathrm{Hz})^{1/2}$ at 1 T. The demonstration of low noise of such a SQUID in Tesla fields is a decisive step toward utilizing the full potential of ultrasensitive nanoSQUIDs for direct measurements of magnetic hysteresis curves of magnetic nanoparticles and molecular magnets.

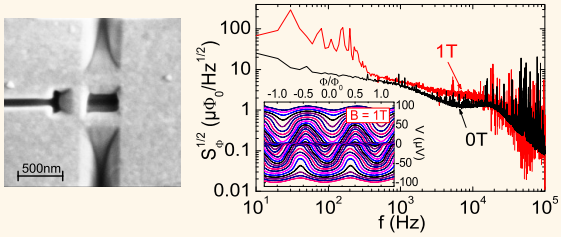

KEYWORDS: YBCO · SQUID · superconductivity · nanofabrication · flux noise · spin sensitivity · magnetic particle detection

Growing interest in the detection and investigation of small spin systems like single-molecular/single-chain magnets,[1,2] cold atom clouds,[3] or even single electrons/atoms[4] demands for sensors that are sensitive to very small changes of the magnetization of small particles with the ultimate goal of single spin detection. The interest for the investigation of such particles affects many fields of research such as material science, chemistry, information technology, medical and biological science, or studies of quantum effects in mesoscopic matter. In order to meet the challenge of detecting a single electron spin, various techniques such as magnetic resonance force microscopy,[5] magneto-optic spin detection,[6,7] and scanning tunneling microscopy assisted electron spin resonance[8,9] have been adapted.

In contrast to these techniques, miniaturized Hall bars[10,11] or direct current (dc) superconducting quantum interference devices (SQUIDs)[12−29] offer the possibility of measuring directly magnetization changes in small spin systems by probing changes of the particle's stray magnetic field or magnetic flux coupled to the Hall bars or SQUIDs, respectively. Such devices can be operated continuously as field-to-voltage or flux-to-voltage converters (for dc SQUIDs with nonhysteretic Josephson junctions), allowing one to investigate magnetization dynamics of the sample under investigation. Indeed, apart from pioneering work by Wernsdorfer *et al.* using microSQUIDs for the measurements of the magnetization of nanoparticles,[13] recent publications reported on preliminary measurements of small clusters of nanoparticles by using nanoSQUIDs with a flux capture area below 1 μm^2.[22,26,30]

For SQUIDs, scaling down their size to the submicrometer range offers the possibility to reach extremely low values of the spectral density of flux noise power S_Φ (*via* reduction of the inductance L of the SQUID loop).[31] Furthermore, by placing a magnetic particle on top of a very narrow constriction intersecting the SQUID loop, one can achieve a large coupling factor $\phi_\mu \equiv \Phi/\mu$, that is, the amount of magnetic flux Φ

* Address correspondence to koelle@uni-tuebingen.de.

Received for review November 22, 2012 and accepted December 19, 2012.

Published online December 19, 2012
10.1021/nn305431c

which is coupled by a particle with magnetic moment μ to the SQUID loop. Hence, it has been proposed that nanoSQUIDs may reach spin sensitivities $S_\mu^{1/2} \equiv S_\Phi^{1/2}/\phi_\mu$ of only a few $\mu_B/(\mathrm{Hz})^{1/2}$,[32] where μ_B is the Bohr magneton. Taking $\phi_\mu \approx 20\ n\Phi_0/\mu_B$, for example, which is achievable as we demonstrate below, a spin sensitivity of 1 $\mu_B/(\mathrm{Hz})^{1/2}$ requires an ultralow rms flux noise $S_\Phi^{1/2} = 20\ n\Phi_0/(\mathrm{Hz})^{1/2}$ (Φ_0 is the magnetic flux quantum). We note that state-of-the art, nonminiaturized dc SQUIDs reach values for $S_\Phi^{1/2}$ on the order of 1 $\mu\Phi_0/(\mathrm{Hz})^{1/2}$.[33] However, for very low inductance SQUIDs, values of $S_\Phi^{1/2}$ down to $\sim$20 $n\Phi_0/(\mathrm{Hz})^{1/2}$ have been demonstrated indeed.[31]

So why have we not seen demonstrations of measurements of magnetization reversals of small magnetic particles by using ultrasensitive dc nanoSQUIDs so far? The reason for this is that such measurements typically require the application of very strong magnetic fields in the Tesla range,[13] while very low flux noise in SQUIDs has been demonstrated only for operation of such SQUIDs in the earth's magnetic field ($\sim$60 μT) or, more typically, in a magnetically well-shielded environment in the nT range (*i.e.*, 9 orders of magnitude lower magnetic fields).[33]

Miniaturized nanoSQUIDs based on very thin Nb films with constriction-type Josephson junctions have been operated in impressive background fields in the Tesla range.[34,27] Chen *et al.*[34] achieved operation in fields up to 7 T for SQUIDs made of $d \sim 5.5$ nm thin Nb films. However, there are two drawbacks in this design. First, the very low thickness of the Nb film causes the (kinetic) SQUID inductance L ($\propto 1/d$) and consequently the SQUID flux noise power S_Φ ($\propto L$) to be large,[35] at least 4 orders of magnitude above the values obtained for sensitive state-of-the-art SQUIDs. Second, the constriction junctions have a hysteretic current voltage characteristic (IVC). This prevents continuous measurements and the use of advanced readout schemes,[36] which are required for ultrasensitive dc SQUIDs. Similar values for the flux noise (at $B \sim 0.3$ T) have been reported very recently for boron-doped diamond μ-SQUIDs based on constriction junctions, which operated up to 4 T.[29] For $B > 0.5$ T, the IVCs became nonhysteretic; however, noise data at such high fields have not been reported, and the very low transfer function $V_\Phi \equiv (\partial V/\partial\Phi)_{max} \approx 0.5\ \mu V/\Phi_0$ at $B = 1$ T implies probably similar noise performance as for lower fields (V is the voltage across the SQUID).

We should note here that very sensitive Nb thin film (d = 200 nm) nanoSQUIDs based on nonhysteretic constriction type junctions, resistively shunted with a 150 nm thick W layer, have been realized with $S_\Phi^{1/2} = 0.2\ \mu\Phi_0/(\mathrm{Hz})^{1/2}$.[37] However, these devices are probably only suited for operation in subTesla fields[38] and show optimum performance only in a narrow temperature range not too far below the transition temperature (T_c) of Nb. This makes them less interesting for applications which are most promising for temperatures of a few Kelvin and well below.[13]

In order to fully exploit the potential of SQUIDs, there is thus a clear need to develop sensitive nanoSQUIDs with nonhysteretic IVCs that at the same time can be operated in strong background fields. As for the SQUIDs with constriction junctions, such SQUIDs should incorporate at least one very thin and/or narrow section where the magnetic particle is placed, allowing for a good coupling of the magnetic stray field of the particle to the SQUID. This all calls for a superconductor which has a very high critical field and allows for patterning nanosized structures and not too large Josephson junctions. The cuprate superconductor $YBa_2Cu_3O_7$ (YBCO) fulfills these requirements. Compared to Nb, YBCO is not a mature material and even the most reliable type of YBCO Josephson junctions, such as grain boundary junctions (GBJs), exhibit a large $1/f$ noise as well as an appreciable scatter in their electrical parameters.[39,40] Nonetheless, based on a recently developed process for fabricating high-quality submicrometer YBCO grain boundary junctions,[41] SQUIDs with high spin sensitivity can be fabricated reproducibly. YBCO GBJ SQUIDs have already been demonstrated to operate in $B = 1$ T[4] and were used to measure magnetization curves of microscale magnets in fields up to 0.12 T,[42] however, with poor noise performance. Here, we show that this field scale can be extended to above 1 T, while still maintaining state-of-the art noise performance of the SQUID.

RESULTS AND DISCUSSION

Sample Fabrication and Layout. The YBCO nanoSQUIDs were made in a similar way, as described in Nagel *et al.*[41] Using pulsed laser deposition, epitaxial *c*-axis-oriented YBCO thin films of thickness $d = 50$ nm were grown on $SrTiO_3$ (STO) [001] bicrystal substrates with misorientation angle $\Theta = 24°$. Subsequently, a Au layer of thickness $d_{Au} = 60$ nm was evaporated *in situ*, serving as a shunt resistance for the YBCO GBJs (providing nonhysteretic IVCs at the envisaged operation temperature $T = 4.2$ K and below) and also acting as a protection layer during focused ion beam (FIB) milling. The critical temperature (T_c) of the YBCO film, measured inductively, was $\sim$91 K.

To obtain the nanoSQUID, structures with line widths down to 1 μm (at the region of the grain boundary) were prepatterned by photolithography and Ar ion milling. Subsequently, two nanoscaled Josephson junctions and a constriction next to the SQUID loop, which permits modulation of the SQUID by applying an additional current I_{mod}, were patterned by FIB. Cutting deep into the STO substrate results in sloped junction edges due to redeposition of amorphous YBCO and STO, which should help to prevent oxygen outdiffusion from the YBCO film. With this procedure, we could fabricate high-performance SQUIDs with junction

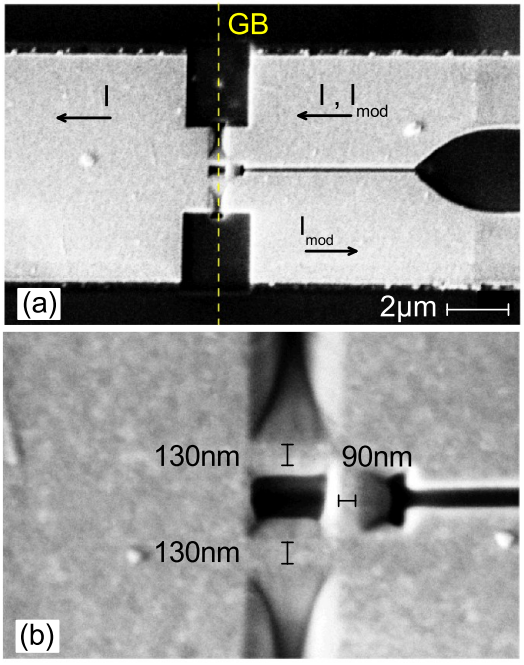

Figure 1. SEM images of the nanoSQUID. In (a), the directions of the modulation and bias currents I_{mod} and I are indicated by arrows, and the grain boundary (GB) is indicated by the vertical dashed line. In (b), the widths of the most narrow sections of the nanoSQUID are indicated.

widths w_J down to ~100 nm. The SQUIDs had almost identical transport and noise characteristics. Below, we discuss data of one device.

Figure 1 shows a scanning electron microscope (SEM) image of the nanoSQUID with a hole size of 300 nm × 400 nm. The junctions have a width $w_J \approx$ 130 nm, and the lengths of the bridges containing the junctions are $l_J \approx 400$ nm. The constriction has a width $w_c \approx 90$ nm and length $l_c = 300$ nm. A bias current I flowing across the junctions, as well as a modulation current I_{mod} flowing across the constriction are applied as indicated by arrows in Figure 1a.

Electric Transport Data. All measurements were performed at $T = 4.2$ K with the magnetic field B carefully aligned in the plane of the SQUID loop. Figure 2a shows the IVC of the nanoSQUID at $B = 0$ and $I_{mod} = 0$. We find a critical current of the SQUID $I_c = 2I_0 = 37\ \mu$A and a resistance $R/2 = 3.5\ \Omega$, which results in $I_0R = 130\ \mu$V (I_0 and R refer to the average junction critical current and resistance, respectively). The corresponding values $j_0 = I_0/(w_J d) = 2.85$ mA/μm^2, $\rho = Rw_J d = 0.046\ \Omega\cdot\mu$m^2, and the value for I_0R are close to the values obtained for earlier devices.[41] Very slightly above I_c, the voltage increases continuously from zero, but then the IVC develops a small hysteresis between 15 and 70 μV. This is presumably caused by some Fiske or LC-type resonance, which prevented accurately fitting the resistive part of this IVC to a resistively and capacitively shunted junction (RCSJ) model.[43,44] Simulations using Langevin equations[45] were still possible for $I_c(I_{mod})$.

Figure 2b shows the measured $I_c(I_{mod})$ at $B = 0$ (solid black line), together with $I_c(I_{mod})$ curves at $B = 1$ and 3 T, which will be discussed below. The data for $B = 0$ are fitted well by the Langevin simulations, which is shown as the dashed cyan line. For the simulations, we have used a noise parameter $\Gamma = 2\pi k_B T/I_0\Phi_0 = 0.01$, corresponding to the measured value of I_0 at $T = 4.2$ K. We further used an inductance asymmetry $\alpha_L = (L_2 - L_1)/(L_1 + L_2) = 0.175$ due to asymmetric biasing of the device; here, L_1 and L_2 are the inductance of the upper and lower arm of the SQUID, respectively (cf. Figure 1). We also used a junction critical current asymmetry $\alpha_i = (I_{02} - I_{01})/(I_{01} + I_{02}) = 0.22$. For the inductance parameter, the simulations yield $\beta_L \equiv 2I_0L/\Phi_0 = 0.65$, which results in $L = 36$ pH. From the $I_c(I_{mod})$ modulation period, we find for the magnetic flux Φ, coupled to the SQUID by I_{mod}, the value $\Phi/I_{mod} = 3.1\ \Phi_0$/mA, which corresponds to a mutual inductance $M_{mod} = 6.4$ pH. We note that the values quoted above for L and M_{mod} are determined experimentally; given the geometry of our device, these values seem to be consistent. However, using standard expressions taking into account the large contribution of the kinetic inductance due to the small YBCO film thickness $d \ll \lambda_L$ (λ_L is the London penetration depth), one expects much smaller values for L and M_{mod}. The reason for this is still unclear. The final parameter to be determined is the Stewart–McCumber parameter $\beta_C \equiv 2\pi I_0R^2C/\Phi_0$, where C is the junction capacitance. Since we cannot fit the experimental IVC accurately, we cannot infer a precise number here. However, due to the fact that a small hysteresis shows up in limited ranges of bias current and applied flux, we assume that β_C is on the order of 1, yielding $C \approx 0.36$ pF. Figure 2c shows the $V(\Phi)$ characteristics of the device for bias currents I ranging from −49.5 to 49.5 μA at $B = 0$. Near $I = I_c$, the curves are hysteretic. The transfer function, that is, the maximum slope of the $V(\Phi)$ curves at optimum I (determined for the nonhysteretic curves), is $V_\Phi = 500\ \mu V/\Phi_0$.

For further measurements, the nanoSQUID was shunted by the input circuit of the SQUID amplifier with an input resistance $R_{inp} = 10\ \Omega$. The additional shunt resistance reduces β_C, yielding nonhysteretic IVCs and $V(I_{mod})$ characteristics; in this case, $V_\Phi \approx 450\ \mu V/\Phi_0$ (at $B = 0$).

At $B = 1$ T (cf. dashed red line in Figure 2b), the $I_c(I_{mod})$ characteristics show a slightly suppressed maximum critical current $I_c(1\ T) = 30\ \mu$A. This pattern is shifted in comparison to the $B = 0$ data, as the SQUID is not perfectly aligned to the magnetic field and flux couples into the Josephson junctions and the SQUID loop. In addition, when sweeping I_{mod} back and forth, a hysteresis becomes visible in a small interval of I_{mod}, presumably caused by Abrikosov vortices trapped in the bias leads. Flux jumps caused by Abrikosov vortices also affect the modulation period, reducing it by about 5% in the interval plotted in Figure 2b. Figure 2d shows

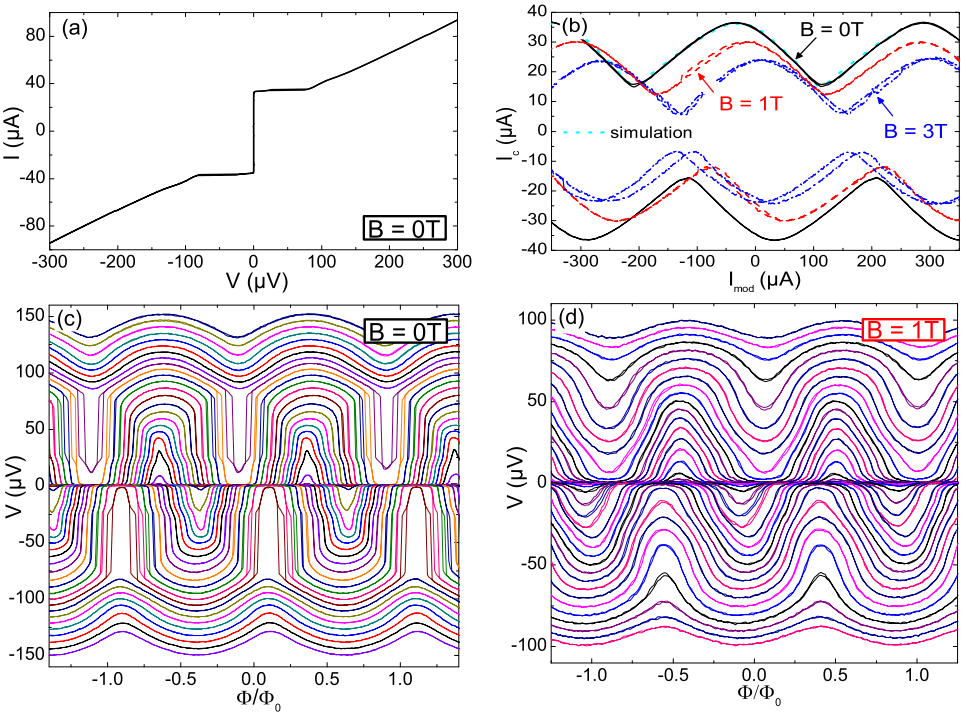

Figure 2. Transport characteristics of the nanoSQUID: (a) IVC at $I_{mod} = 0$ and $B = 0$. (b) Critical current $I_c(I_{mod})$ for $B = 0$, 1, and 3 T; for comparison, the numerically calculated curve for $B = 0$ is also shown. (c) $V(\Phi)$ at $B = 0$ for $I = -49.5 \ldots 49.5$ μA (in 1.5 μA steps.) (d) $V(\Phi)$ at $B = 1$ T for currents fed to the SQUID which is shunted by the input resistance $R_{inp} = 10\ \Omega$ of the SQUID amplifier $I_b = -40.5 \ldots 40.5$ μA (in 1.5 μA steps.) All curves in (a–d) were traced out in both sweep directions.

$V(\Phi)$ characteristics at $B = 1$ T for currents I_b (fed to the SQUID which is shunted by R_{inp}) ranging from -40.5 to 40.5 μA. The IVCs are nonhysteretic and hence the $V(\Phi)$ characteristics are smooth, exhibiting no jumps as in Figure 2c. The lack of hysteresis is either due to the additional shunt resistance R_{inp} or due to the strong magnetic field suppressing the critical current. The transfer function is $V_\Phi = 350\ \mu V/\Phi_0$. Interestingly, the hysteresis in $V(\Phi)$ at $B = 1$ T upon sweeping the applied flux in both directions almost disappeared, which is helpful for reading out the SQUID when operated in strong magnetic fields.

Upon increasing B up to 3 T, still periodic $I_c(I_{mod})$ characteristics with only a slightly suppressed maximum critical current $I_c = 24$ μA could be measured, as shown in Figure 2b as blue dashed-dotted lines. The shift in comparison to the $B = 0$ data did increase further, and also the hysteresis did increase, as mentioned above presumably due to vortices in the bias leads. These data clearly show that the SQUID is operating also in $B = 3$ T. As mentioned above, noise measurements could not be performed for fields much higher than 1 T since the SQUID amplifier trapped magnetic flux. However, this is just a technical problem which can be solved in future measurements by implementing field compensation *via* a coil mounted around the Nb shield.

Flux Noise Measurements. Figure 3 summarizes the flux noise spectra $S_\Phi^{1/2}(f)$ of the nanoSQUID at $B = 0$ and $B = 1$ T at the optimum working point.

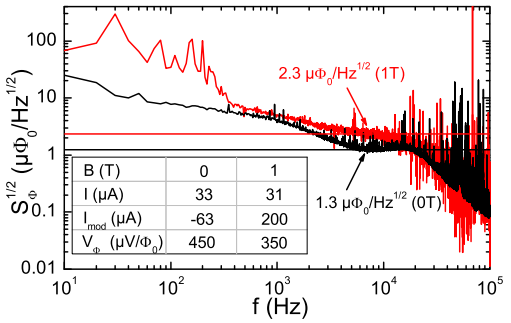

Figure 3. Flux noise spectra of the nanoSQUID at optimum working points at $B = 0$ and 1 T. The horizontal lines indicate the white noise levels.

As measurements were performed without magnetic shielding, noise spikes occur on both spectra. The noise data were corrected for the noise contribution of the amplifier. In both cases, $S_\Phi^{1/2}$ increases for frequencies f below ~3 kHz, a behavior which at least for $B = 0$ is known to arise from critical current fluctuations of the junctions. This contribution can, in principle, be eliminated by proper modulation techniques (bias reversal).[46] At $B = 1$ T, there are presumably additional contributions due to fluctuating Abrikosov vortices. Note, however, that between ~300 Hz and 3 kHz the noise level is less than a factor of 2 higher at $B = 1$ T as compared to $B = 0$. The decrease in $S_\Phi^{1/2}$ above 10 kHz is caused by the limited bandwidth of our measurement setup. At $B = 0$, the white noise level averaged between 6 and 7 kHz is 1.3 $\mu\Phi_0/(\text{Hz})^{1/2}$. For $B = 1$ T, we determine

a rms flux noise of 2.3 $\mu\Phi_0/(\mathrm{Hz})^{1/2}$ averaged between 6 and 7 kHz.

These numbers may be compared to the theoretical expression obtained from Langevin simulations, $S_\Phi = f(\beta_L)\Phi_0 k_B TL/I_0 R$, which is valid for $\beta_C \lesssim 1$.[47] For $\beta_L > 0.4$, $f(\beta_L) \approx 4(1 + \beta_L)$. For lower values of β_L, S_Φ increases. For the parameters of our device, we calculate $S_\Phi^{1/2} = 0.23\ \mu\Phi_0/(\mathrm{Hz})^{1/2}$, that is, a factor of almost 6 less than the experimental value at $B = 0$. Such an excess noise is not unusual for YBCO SQUIDs.[46]

Finally, we note that the observed increase by a factor of ~1.8 in $S_\Phi^{1/2}$ at 6−7 kHz upon increasing B from 0 to 1 T cannot be explained by the reduction of I_0 and V_Φ. From the above-mentioned expression for S_Φ, one would only expect an increase in the white rms flux noise by ~10%. However, we note that in the flux noise data for B = 1 T (cf. Figure 3) no clear white noise is observable. Hence, the quoted value for $S_\Phi^{1/2}(B = 1\ \mathrm{T})$ should be seen as an upper limit for the white noise level.

Spin Sensitivity. In order to estimate the spin sensitivity $S_\mu^{1/2} = S_\Phi^{1/2}/\phi_\mu$ of the nanoSQUID, we numerically calculated the coupling factor $\phi_\mu = \Phi/\mu$, that is, the flux Φ coupled into the SQUID loop by a point-like particle with magnetic moment μ, using the software package 3D-MLSI.[48] Details on the calculation procedure can be found in Nagel *et al.*[41] In brief, one calculates the magnetic field distribution $\vec{B}(\vec{r})$ generated by a current J circulating around the SQUID hole. The coupling factor is obtained from $\phi_\mu = -\hat{e}_\mu \vec{B}(\vec{r})/J$. Here, $\hat{e}_\mu$ is the direction of the magnetic moment $\vec{\mu}$ at position $\vec{r}$. The results of these calculations are summarized in Figure 4 for a point-like particle with magnetic moment pointing in the x-direction. The particle is located in the (x,z) plane (perpendicular to the plane of the SQUID loop in the (x,y) plane) at position $y = 0$ and $x = 0$ to 1000 nm, as indicated by the dashed line in the SEM image shown in Figure 4a. The contour plot in Figure 4b shows $\phi_\mu(x,z)$ for values of $z = 0$ (substrate surface) up to z = 1000 nm. Figure 4c shows a linescan $\phi_\mu(x)$ through this plane, as indicated by the horizontal dashed line in Figure 4b. The linescan is taken at a distance of 10 nm above the Au layer. The coupling factor ϕ_μ has a maximum of 9.2 $n\Phi_0/\mu_B$ at the position of the constriction at $x \approx 0.64\ \mu$m. The minimum in $\phi_\mu(x)$ is slightly left from the center of the SQUID loop; this is because the constriction breaks symmetry. Figure 4d shows a linescan taken along the vertical dashed line in graph (b). The coupling factor ϕ_μ decreases strongly with increasing z. Calculating the spin sensitivity with ϕ_μ = 9.2 $n\Phi_0/\mu_B$, we obtain $S_\mu^{1/2} = 141\ \mu_B/(\mathrm{Hz})^{1/2}$ at $B = 0$ and 250 $\mu_B/(\mathrm{Hz})^{1/2}$ at B = 1 T. In principle, the particle could be brought even closer to the constriction by removing the Au layer right above the constriction, without affecting S_Φ. In this case (for a distance of 10 nm above the YBCO), ϕ_μ = 21 $n\Phi_0/\mu_B$ and $S_\mu^{1/2}$ = 62 $\mu_B/(\mathrm{Hz})^{1/2}$ at $B = 0$ and 110 $\mu_B/(\mathrm{Hz})^{1/2}$ at B = 1 T. The geometrical and electrical parameters for our device are summarized in Table 1.

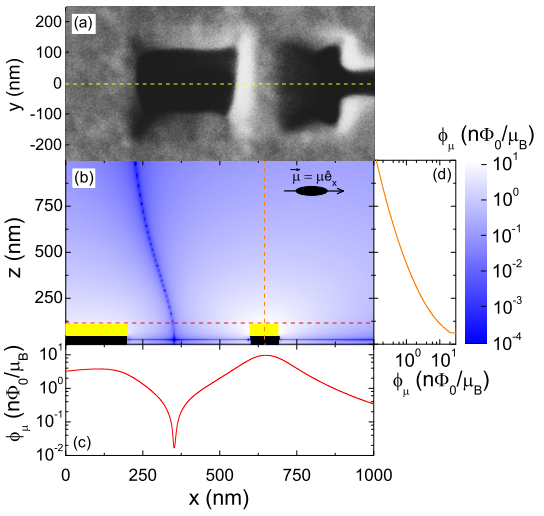

Figure 4. Calculated coupling factor ϕ_μ for the nanoSQUID. (a) SEM image showing SQUID hole and constriction in the (x,y) plane. The dashed line indicates the location of the (x,z) plane for which data are shown in (b); it also indicates the position of the linescan $\phi_\mu(x)$ shown in (c). (b) Contour plot of the coupling factor ϕ_μ *vs* position (x,z) of a magnetic moment pointing in the x-direction. Dashed lines indicate position of the linescans shown in (c) and (d). (c) Horizontal linescan $\phi_\mu(x)$ at a distance of 10 nm above the Au layer. (d) Vertical linescan $\phi_\mu(z)$ at the center of the constriction.

TABLE 1. Summary of Geometric and Electric NanoSQUID Parameters (As Defined in the Text)

d (nm)	l_c (nm)	l_j (nm)	w_c (nm)	w_j (nm)	β_L	L (pH)
50	300	400	90	130	0.65	36

I_0 (μA)	R (Ω)	I_0R (mV)	j_0 (mA/μm^2)	$S_\Phi^{1/2}$ ($n\Phi_0/(\mathrm{Hz})^{1/2}$)	ϕ_μ ($n\Phi_0/\mu_B$)	$S_\mu^{1/2}$ ($\mu_B/(\mathrm{Hz})^{1/2}$)
18.5	7.0	0.13	2.85	1300	21	62

CONCLUSIONS

In summary, we have demonstrated low-noise performance of a YBCO nanoSQUID in magnetic fields up to 1 T. At zero applied field, the white flux noise of the device at 7 kHz was 1.3 $\mu\Phi_0/(\mathrm{Hz})^{1/2}$, increasing only slightly to 2.3 $\mu\Phi_0/(\mathrm{Hz})^{1/2}$ at 1 T. For the spin sensitivity, assuming that a small particle is placed onto a constriction in the SQUID loop, directly on top of the YBCO film, we calculated values of 62 $\mu_B/(\mathrm{Hz})^{1/2}$ at $B = 0$ and 110 $\mu_B/(\mathrm{Hz})^{1/2}$ at B = 1 T.

The device investigated experimentally was not optimized yet in terms of its geometrical and electrical parameters. In particular, the thickness of the epitaxially grown YBCO films can be increased (to ~300 nm). This, in turn, would decrease the SQUID inductance by approximately a factor of 10, which will significantly reduce the flux noise. However, such an increase in thin film thickness will also reduce the coupling factor.

Hence, one has to carefully optimize all SQUID parameters by also taking into account technological constraints. Very recently, we performed such an optimization study, for YBCO nanoSQUIDs operated at 4.2 K and below, which predicts an optimum spin sensitivity of a few $\mu_B/(\mathrm{Hz})^{1/2}$. It remains to be shown whether or not such values can be achieved in high fields.

Furthermore, we note that miniaturized YBCO dc SQUIDs have been already used to investigate the magnetic properties of magnetic microcrystals at 0.12 T between 30 and 70 K.[42] Hence, due to their high T_c, YBCO nanoSQUIDs might also be useful for applications over a wide temperature range up to 70−80 K, such as for the investigation of the transition between the superparamagnetic and ferromagnetic state of magnetic nanoparticles. Optimization of the SQUID parameters for such a large temperature range—and according variation in the critical current of the grain boundary junctions and hence in the noise parameter Γ, the inductance parameter β_L and the Stewart−McCumber parameter β_C—will be more challenging than for operation at a few Kelvin and below. Still, such an approach may be rewarding because highly sensitive YBCO SQUIDs operating at 77 K have been demonstrated in the past.[46]

METHODS

Film Deposition. The films were deposited on 10 mm × 10 mm (1 mm thick) $SrTiO_3$ [001] bicrystal substrates. The substrates contain a single symmetric [001] tilt grain boundary with misorientation angle $\Theta = 24°$. After mounting the substrates by sliver paste on the sample holder, they were transferred to the ultrahigh vacuum (UHV) thin film deposition cluster tool (base pressure 10^{-9} mbar), equipped with a pulsed laser deposition (PLD) chamber and an electron beam evaporation (EBE) chamber. In the PLD chamber, 60 nm thick YBCO films were grown epitaxially by using a pulsed KrF excimer laser (wavelength 248 nm, pulse frequency 2 Hz), which is ablating material from a stochiometric YBCO target (purity 99.995%) with an energy density of ∼2 J/cm^2 of the laser spot on the target. During deposition at an oxygen pressure $p_{O_2} = 0.2$ mbar, the substrate was heated to a temperature T_s = 780 °C by a laser heating system. For the used 60 mm substrate-to-target distance, the PLD parameters yield a deposition rate of 9.8 nm/s. After deposition, the pressure was increased to p_{O_2} = 450 mbar; subsequently, T_s was reduced to 450 °C and kept there for 30 min before cooling the sample to room temperature. For the next deposition step, the sample was transferred in UHV to the EBE chamber, where a 60 nm thick Au film was deposited by electron beam evaporation (deposition rate ∼0.2 nm/s).

FIB Patterning. FIB patterning was performed in a FEI Dualbeam Strata 235, equipped with a Ga ion source. Parameters for FIB milling needed to be chosen carefully, as this patterning step can suppress superconductivity of YBCO. In the cutting scheme, which finally permitted the fabrication of nanoscaled Josephson junctions with no significant reduction of the critical current density j_c, Ga ion currents where adjusted to 30 pA at an acceleration voltage of 30 kV. Four rectangular patterns cut line-by-line (cleaning cross section cut), with cutting directions pointing away from the Josephson junctions, were placed at the grain boundary to form the final SQUID layout.

Measurements of Electric Transport Properties and Noise. The transport and noise measurements were performed at $T = 4.2$ K in an electrically shielded environment. We used a four-terminal configuration with filtered lines to measure IVCs, critical current $I_c(I_{mod})$, and $V(I_{mod})$. For transport measurements, the voltage V across the SQUID was amplified using a room temperature amplifier. All currents were applied by battery-powered current sources. In-plane magnetic fields up to $B = 7$ T could be applied by a split coil superconducting magnet. As magnetic fields that couple into the Josephson junctions suppress their critical current and hence the modulation amplitude of the SQUID, the SQUID loop needed to be aligned with high accuracy parallel to the magnetic field, and the in-plane field was aligned perpendicular to the grain boundary. To do so, the sample was mounted on two goniometers with perpendicular tilt axes (minimum step size 0.02 m°) and a rotator (minimum step size 0.5 m°). Alignment was done by monitoring and maximizing I_c at $B \sim 1$ T.

For noise measurements, the voltage drop across the nanoSQUID was preamplified by a dc SQUID amplifier[49] with 0.l nV/(Hz)$^{1/2}$ resolution and ∼30 kHz bandwidth. In this case, the SQUID was shunted by the input resistance $R_{inp} = 10\ \Omega$ of the SQUID amplifier. The thermal noise of the input resistance (at $T = 4.2$ K) limits the voltage resolution of the SQUID amplifier. To minimize stray fields, the SQUID amplifier was placed inside a Nb shield mounted inside the cryostat at a position of minimum magnetic field. Still, for $B \sim 1.5$ T (at the sample position), the SQUID amplifier trapped magnetic flux, preventing noise measurements at higher fields.

Conflict of Interest: The authors declare no competing financial interest.

Acknowledgment. We gratefully acknowledge S. Menzel for helping us with his expertise and with FIB facilities at IFW Dresden in the early stage of this project. J.N. and T.S acknowledge support by the Carl-Zeiss-Stiftung. This work was funded by the Nachwuchswissenschaftlerprogramm of the Universität Tübingen, by the Deutsche Forschungsgemeinschaft (DFG) *via* the SFB/TRR 21 and by the European Research Council *via* SOCATHES.

REFERENCES AND NOTES

1. Gatteschi, D.; Sessoli, R. Quantum Tunneling of Magnetization and Related Phenomena in Molecular Materials. *Angew. Chem., Int. Ed.* **2003**, *42*, 268–297.
2. Bogani, L.; Vindigni, A.; Sessoli, R.; Gatteschi, D. Single Chain Magnets: Where to from Here? *J. Mater. Chem.* **2008**, *18*, 4750–4758.
3. Fortágh, J.; Zimmermann, C. Toward Atom Chips. *Science* **2005**, *307*, 860–861.
4. Bushev, P.; Bothner, D.; Nagel, J.; Kemmler, M.; Konovalenko, K. B.; Loerincz, A.; Ilin, K.; Siegel, M.; Koelle, D.; Kleiner, R.; *et al.* Trapped Electron Coupled to Superconducting Devices. *Eur. Phys. J. D* **2011**, *63*, 9–16.
5. Rugar, D.; Budakian, R.; Mamin, H. J.; Chui, B. W. Single Spin Detection by Magnetic Resonance Force Microscopy. *Nature* **2004**, *430*, 329–332.
6. Maze, J. R.; Stanwix, P. L.; Hodges, J. S.; Hong, S.; Taylor, J. M.; Cappellaro, P.; Jiang, L.; Gurudev Dutt, M. V.; Togan, E.; Zibrov, A. S.; *et al.* Nanoscale Magnetic Sensing with an Individual Electronic Spin in Diamond. *Nature* **2008**, *455*, 644–647.
7. Balasubramanian, G.; Chan, I. Y.; Kolesov, R.; Al-Hmoud, M.; Tisler, J.; Shin, C.; Kim, C.; Wojcik, A.; Hemmer, P. R.; Krueger, A.; *et al.* Nanoscale Imaging Magnetometry with Diamond Spins under Ambient Conditions. *Nature* **2008**, *455*, 648–651.
8. Manassen, Y.; Hamers, R. J.; Demuth, J. E.; Castellano, A. J., Jr. Direct Observation of the Precession of Individual Paramagnetic Spins on Oxidized Silicon Surfaces. *Phys. Rev. Lett.* **1989**, *62*, 2531–2534.

9. Durkan, C.; Welland, M. E. Electronic Spin Detection in Molecules Using Scanning-Tunneling-Microscopy-Assisted Electron-Spin Resonance. *Appl. Phys. Lett.* **2002**, *80*, 458–460.
10. Theil Kuhn, L.; Geim, A. K.; Lok, J. G. S.; Hedegård, P.; Ylänen, K.; Jensen, J. B.; Johnson, E.; Lindelof, P. E. Magnetisation of Isolated Single Crystalline Fe-Nanoparticles Measured by a Ballistic Hall Micro-Magnetometer. *Eur. Phys. J. D* **2000**, *10*, 259–263.
11. Kazakova, O.; Panchal, V.; Gallop, J.; See, P.; Cox, D. C.; Spasova, M.; Cohen, L. F. Ultrasmall Particle Detection Using a Submircon Hall Sensor. *J. Appl. Phys.* **2010**, *107*, 09E708.
12. Voss, R. F.; Laibowitz, R. B.; Broers, A. N. Niobium Nanobridge dc SQUID. *Appl. Phys. Lett.* **1980**, *37*, 656–658.
13. Wernsdorfer, W. Classical and Quantum Magnetization Reversal Studied in Nanometersized Particles and Clusters. *Adv. Chem. Phys.* **2001**, *118*, 99–190.
14. Lam, S. K. H.; Tilbrook, D. L. Development of a Niobium Nanosuperconducting Quantum Interference Device for the Detection of Small Spin Populations. *Appl. Phys. Lett.* **2003**, *82*, 1078–1080.
15. Cleuziou, J.-P.; Wernsdorfer, W.; Bouchiat, V.; Ondarçuhu, T.; Monthioux, M. Carbon Nanotube Superconducting Quantum Interference Device. *Nat. Nanotechnol.* **2006**, *1*, 53–59.
16. Troeman, A. G. P.; Derking, H.; Borger, B.; Pleikies, J.; Veldhuis, D.; Hilgenkamp, H. NanoSQUIDs Based on Niobium Constrictions. *Nano Lett.* **2007**, *7*, 2152–2156.
17. Huber, M. E.; Koshnick, N. C.; Bluhm, H.; Archuleta, L. J.; Azua, T.; Björnsson, P. G.; Gardner, B. W.; Halloran, S. T.; Lucero, E. A.; Moler, K. A. Gradiometric Micro-SQUID Susceptometer for Scanning Measurements of Mesoscopic Samples. *Rev. Sci. Instrum.* **2008**, *79*, 053704.
18. Granata, C.; Esposito, E.; Vettoliere, A.; Petti, L.; Russo, M. An Integrated Superconductive Magnetic Nanosensor for High-Sensitivity Nanoscale Applications. *Nanotechnology* **2008**, *19*, 275501.
19. Wu, C. H.; Chou, Y. T.; Kuo, W. C.; Chen, J. H.; Wang, L. M.; Chen, J. C.; Chen, K. L.; Sou, U. C.; Yang, H. C.; Jeng, J. T. Fabrication and Characterization of High-T_c $YBa_2Cu_3O_{7-x}$ NanoSQUIDs Made by Focused Ion Beam Milling. *Nanotechnology* **2008**, *19*, 315304.
20. Koshnick, N. C.; Huber, M. E.; Bert, J. A.; Hicks, C. W.; Large, J.; Edwards, H.; Moler, K. A. A Terraced Scanning Superconducting Quantum Interference Device Susceptometer with Submicron Pickup Loops. *Appl. Phys. Lett.* **2008**, *93*, 243101.
21. Foley, C. P.; Hilgenkamp, H. Why NanoSQUIDs Are Important: An Introduction to the Focus Issue. *Supercond. Sci. Technol.* **2009**, *22*, 064001.
22. Vohralik, P. F.; Lam, S. K. H. NanoSQUID Detection of Magnetization from Ferritin Nanoparticles. *Supercond. Sci. Technol.* **2009**, *22*, 064007.
23. Bouchiat, V. Detection of Magnetic Moments Using a Nano-SQUID: Limits of Resolution and Sensitivity in Near-Field SQUID Magnetometry. *Supercond. Sci. Technol.* **2009**, *22*, 064002.
24. Faucher, M.; Jubert, P.-O.; Fruchart, O.; Wernsdorfer, W.; Bouchiat, V. Optimizing the Flux Coupling between a NanoSQUID and a Magnetic Particle Using Atomic Force Microscope Nanolithography. *Supercond. Sci. Technol.* **2009**, *22*, 064010.
25. Finkler, A.; Segev, Y.; Myasoedov, Y.; Rappaport, M. L.; Ne'eman, L.; Vasyukov, D.; Zeldov, E.; Huber, M. E.; Martin, J.; Yacoby, A. Self-Aligned Nanoscale SQUID on a Tip. *Nano Lett.* **2010**, *10*, 1046–1049.
26. Hao, L.; Aßmann, C.; Gallop, J. C.; Cox, D.; Ruede, F.; Kazakova, O.; Josephs-Franks, P.; Drung, D.; Schurig, T. Detection of Single Magnetic Nanobead with a Nano-Superconducting Quantum Interference Device. *Appl. Phys. Lett.* **2011**, *98*, 092504.
27. Lam, S. K. H.; Clem, J. R.; Yang, W. A Nanoscale SQUID Operating at High Magnetic Fields. *Nanotechnology* **2011**, *22*, 455501.
28. Nagel, J.; Kieler, O. F.; Weimann, T.; Wölbing, R.; Kohlmann, J.; Zorin, A. B.; Kleiner, R.; Koelle, D.; Kemmler, M. Superconducting Quantum Interference Devices with Submicron Nb/HfTi/Nb Junctions for Investigation of Small Magnetic Particles. *Appl. Phys. Lett.* **2011**, *99*, 032506.
29. Mandal, S.; Bautze, T.; Williams, O. A.; Naud, C.; Étienne Bustarret,; Omnès, F.; Rodière, P.; Meunier, T.; Bäuerle, C.; Saminadayar, L. The Diamond Superconducting Quantum Interference Device. *ACS Nano* **2011**, *5*, 7144–7148.
30. Russo, R.; Granata, C.; Esposito, E.; Peddis, D.; Cannas, C.; Vettoliere, A. Nanoparticle Magnetization Measurements by a High Sensitive Nano-Superconducting Quantum Interference Device. *Appl. Phys. Lett.* **2012**, *101*, 122601.
31. Van Harlingen, D. J.; Koch, R. H.; Clarke, J. Superconducting Quantum Interference Device with Very Low Magnetic Flux Noise Energy. *Appl. Phys. Lett.* **1982**, *41*, 197–199.
32. Gallop, J. SQUIDs: Some Limits to Measurement. *Supercond. Sci. Technol.* **2003**, *16*, 1575–1582.
33. Kleiner, R.; Koelle, D.; Ludwig, F.; Clarke, J. Superconducting Quantum Interference Devices: State-of-the-Art and Applications. *Proc. IEEE* **2004**, *92*, 1534–1548.
34. Chen, L.; Wernsdorfer, W.; Lampropoulos, C.; Christou, G.; Chiorescu, I. On-Chip SQUID Measurements in the Presence of High Magnetic Fields. *Nanotechnology* **2010**, *21*, 405504.
35. Wernsdorfer, W. From Micro- to Nano-SQUIDs: Applications to Nanomagnetism. *Supercond. Sci. Technol.* **2009**, *22*, 064013.
36. Drung, D.; Mück, M. In *The SQUD Handbook*; Clarke, J., Braginski, A. I., Eds.; Wiley-VCH: Weinheim, Germany, 2004; Vol. 1: Fundamentals and Technology of SQUIDs and SQUID Systems, Chapter 4, pp 127–170.
37. Hao, L.; Macfarlane, J. C.; Gallop, J. C.; Cox, D.; Beyer, J.; Drung, D.; Schurig, T. Measurement and Noise Performance of Nano-Superconducting-Quantum-Interference Devices Fabricated by Focused Ion Beam. *Appl. Phys. Lett.* **2008**, *92*, 192507.
38. Romans, E. J.; Rozhko, S.; Young, L.; Blois, A.; Hao, L.; Cox, D.; Gallop, J. C. Noise Performance of Niobium Nano-SQUIDs in Applied Magnetic Fields. *IEEE Trans. Appl. Supercond.* **2011**, *21*, 404–407.
39. Gross, R.; Alff, L.; Beck, A.; Froehlich, O.; Koelle, D.; Marx, A. Physics and Technology of High Temperature Superconducting Josephson Junctions. *IEEE Trans. Appl. Supercond.* **1997**, *7*, 2929–2935.
40. Hilgenkamp, H.; Mannhart, J. Grain Boundaries in High-T_c Superconductors. *Rev. Mod. Phys.* **2002**, *74*, 485.
41. Nagel, J.; Konovalenko, K. B.; Kemmler, M.; Turad, M.; Werner, R.; Kleisz, E.; Menzel, S.; Klingeler, R.; Büchner, B.; Kleiner, R.; *et al.* Resistively Shunted $YBa_2Cu_3O_7$ Grain Boundary Junctions and Low-Noise SQUIDs Patterned by a Focused Ion Beam down to 80 nm Linewidth. *Supercond. Sci. Technol.* **2011**, *24*, 015015.
42. Takeda, K.; Mori, H.; Yamaguchi, A.; Ishimoto, H.; Nakamura, T.; Kuriki, S.; Hozumi, T.; Ohkoshi, S. High Temperature Superconductor Micro-Superconducting-Quantum-Interference-Device Magnetometer for Magnetization Measurement of a Microscale Magnet. *Rev. Sci. Instrum.* **2008**, *79*, 033909.
43. Stewart, W. C. Current-Voltage Characteristics of Josephson Junctions. *Appl. Phys. Lett.* **1968**, *12*, 277.
44. McCumber, D. Effect of ac Impedance of dc Voltage-Current Characteristics of Josephson Junctions. *J. Appl. Phys.* **1968**, *39*, 3113.
45. Tesche, C. D.; Clarke, J. DC SQUID: Noise and Optimization. *J. Low Temp. Phys.* **1977**, *29*, 301–331.
46. Koelle, D.; Kleiner, R.; Ludwig, F.; Dantsker, E.; Clarke, J. High-Transition-Temperature Superconducting Quantum Interference Devices. *Rev. Mod. Phys.* **1999**, *71*, 631–686.
47. Chesca, B.; Kleiner, R.; Koelle, D. In *The SQUD Handbook*; Clarke, J., Braginski, A. I., Eds.; Wiley-VCH: Weinheim, Germany, 2004; Vol. 1: Fundamentals and Technology of SQUIDs and SQUID Systems, Chapter 2, pp 29–92.
48. Khapaev, M.; Kupriyanov, M.; Goldobin, E.; Siegel, M. Current Distribution Simulation for Superconducting Multi-Layered Structures. *Supercond. Sci. Technol.* **2003**, *16*, 24–27.
49. SQ100 LTS dc SQUID, PC-100 Single-Channel dc SQUID Electronics System, STAR Cryoelectronics, USA.

Publication 3

IOP Publishing Superconductor Science and Technology
Supercond. Sci. Technol. **27** (2014) 125007 (12pp) doi:10.1088/0953-2048/27/12/125007

Optimizing the spin sensitivity of grain boundary junction nanoSQUIDs—towards detection of small spin systems with single-spin resolution

R Wölbing, T Schwarz, B Müller, J Nagel, M Kemmler, R Kleiner and D Koelle

Physikalisches Institut-Experimentalphysik II and Center for Collective Quantum Phenomena in LISA$^+$, Universität Tübingen, Auf der Morgenstelle 14, D-72076 Tübingen, Germany

Received 3 June 2014, revised 22 September 2014
Accepted for publication 24 September 2014
Published 7 November 2014

Abstract

We present an optimization study of the spin sensitivity of nano superconducting quantum interference devices (SQUIDs) based on resistively shunted grain boundary Josephson junctions. In addition the direct current SQUIDs contain a narrow constriction onto which a small magnetic particle can be placed (with its magnetic moment in the plane of the SQUID loop and perpendicular to the grain boundary) for efficient coupling of its stray magnetic field to the SQUID loop. The separation of the location of optimum coupling from the junctions allows for an independent optimization of the coupling factor ϕ_μ and junction properties. We present different methods for calculating ϕ_μ (for a magnetic nanoparticle placed 10 nm above the constriction) as a function of device geometry and show that those yield consistent results. Furthermore, by numerical simulations we obtain a general expression for the dependence of the SQUID inductance on geometrical parameters of our devices, which allows to estimate their impact on the spectral density of flux noise S_Φ of the SQUIDs in the thermal white noise regime. Our analysis of the dependence of S_Φ and ϕ_μ on the geometric parameters of the SQUID layout yields a spin sensitivity $S_\mu^{1/2} = S_\Phi^{1/2}/\phi_\mu$ of a few μ_B Hz$^{-1/2}$ (μ_B is the Bohr magneton) for optimized parameters, respecting technological constraints. However, by comparison with experimentally realized devices we find significantly larger values for the measured white flux noise, as compared to our theoretical predictions. Still, a spin sensitivity on the order of $10\,\mu_B$ Hz$^{-1/2}$ for optimized devices seems to be realistic.

Keywords: Josephson junctions, nanoSQUIDs, spin sensitivity

(Some figures may appear in colour only in the online journal)

1. Introduction

Miniaturized direct current (dc) superconducting quantum interference devices (SQUIDs) with dimensions in the sub-micrometer range (nanoSQUIDs) are promising devices for the sensitive detection and investigation of small spin systems [1]. The basic idea behind this is to attach a small (nanometer-sized) magnetic particle directly to the SQUID and trace out magnetic hysteresis loops of the particle. This shall be done by detecting the change of the stray magnetic field of the particle with magnetic moment $\boldsymbol{\mu}$ via the change of the magnetic flux Φ coupled to the SQUID loop [2–4]. To meet the ultimate goal of detecting the flipping of only a few electron spins [5], the spin sensitivity $S_\mu^{1/2} = S_\Phi^{1/2}/\phi_\mu$ has to be optimized carefully via reducing the spectral density of flux noise S_Φ of the SQUID and increasing the coupling factor $\phi_\mu \equiv \Phi/\mu$ (with $\mu \equiv |\boldsymbol{\mu}|$). S_Φ can be reduced by shrinking the size of the SQUID loop, and hence its inductance L, and ϕ_μ

can be increased by placing the particle on a narrow constriction inserted in the SQUID loop, which motivates the need to implement sub-micron SQUID structures [2, 4, 6–26].

Until now, the most common approach for the realization of nanoSQUIDs is to use constriction type Josephson junctions (cJJs) intersecting small SQUID loops (see e.g. [13] published in a special issue on nanoSQUIDs and related articles therein and [7, 8, 10, 12, 15, 20, 23, 25]). Although impressive results have been achieved very recently for ultra-small SQUIDs based on Pb constrictions [24], the cJJ approach comes with several drawbacks: cJJs often show hysteretic current–voltage characteristics (IVCs). This hampers continuous operation of cJJ-based nanoSQUIDs, which however is required for the investigation of the magnetization dynamics of the sample under investigation. Hence, more advanced readout-schemes are required for operating such devices. Here, a promising approach is the dispersive nanoSQUID magnetometer with ultra-low flux noise down to $\sim 30\ \mathrm{n}\Phi_0\ \mathrm{Hz}^{-1/2}$ achieved with Al variable thickness nanobridges at 30 mK [23]. We should also note here, that very sensitive Nb thin film nanoSQUIDs based on cJJs, resistively shunted with a thin W layer and operated in the voltage state, have been realized [12]. However, in this case, the devices show optimum performance only in a narrow range of temperature T not too far below the transition temperature T_c of Nb, which makes them less interesting for applications. Also, the noise properties of cJJs are not well understood and hence hard to optimize. And, finally, the magnetic particles have to be placed close to the cJJs to achieve optimum coupling. However, this means that the junction properties and the coupling factor ϕ_μ cannot be optimized independently, which hampers a careful optimization of the spin sensitivity.

With respect to the application of nanoSQUIDs for the detection of the magnetization reversal of nanomagnets, the most interesting regime of operation is at $T \approx 1$ K and below and at very high magnetic fields in the tesla range [1]. It has been demonstrated that Nb thin film nanoSQUIDs based on constriction type junctions can be operated in impressive background fields up to 7 T [27]. However, the upper critical field B_{c2} of typical Nb thin films ($\sim$1 T) requires to use very thin Nb films with thicknesses of only a few nm, i.e. well below the London penetration depth λ_L of the Nb films, if such SQUIDs shall be operated in tesla fields. This leads to a large kinetic inductance contribution to the SQUID inductance, and hence a large flux noise of such SQUIDs, which does not allow to use the huge potential for the realization of ultralow-noise nanoSQUIDs. We note that ultralow noise values have been achieved for ultra-small SQUIDs based on Pb cJJs up to $\sim$1 T, where the high-field operation was presumably also limited by B_{c2} [24].

To circumvent the above mentioned drawbacks, we recently started to develop dc nanoSQUIDs based on c-axis oriented $YBa_2Cu_3O_7$ (YBCO) thin films with submicron wide bicrystal grain boundary Josephson junctions (GBJs) [28]. Due to the huge upper critical field of YBCO, such SQUIDs can be realized with film thicknesses on the order of λ_L and above and operated in tesla fields. Furthermore, due to the large critical current densities of the YBCO GBJs (several $\mathrm{mA}\,\mu\mathrm{m}^{-2}$ at $T = 4.2$ K and below for a grain boundary misorientation angle of 24°) submicron junctions still yield reasonably large values of the critical current I_0. To achieve non-hysteretic IVCs, the GBJs are shunted by a thin Au film. Due to the fact that the barrier of the GBJs is oriented perpendicular to the YBCO thin film plane, it is possible to apply tesla magnetic fields in the plane of the film, without a significant reduction of I_0 [29]. And finally, by implementing an additional narrow constriction (which can be much narrower than the GBJs) in the SQUID loop, the optimization of the coupling factor for a nanoparticle placed on top of the constriction is possible without affecting the junction properties.

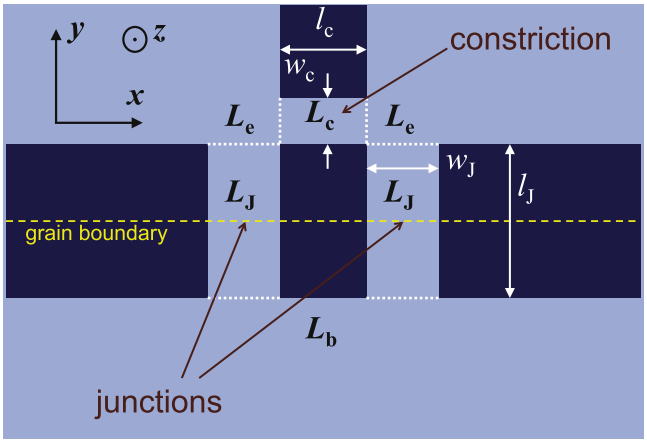

Figure 1. Schematic view of the nanoSQUID layout, divided (by white dotted lines) into the constriction (inductance L_c, length l_c, width w_c), two corners (each with inductance L_e), the two junctions (each with inductance L_J, length l_J, width w_J) and the bottom part (inductance L_b).

Here, we present a detailed optimization study of the spin sensitivity of such grain boundary junction nanoSQUIDs by analyzing the dependence of the flux noise S_Φ and the coupling factor ϕ_μ on the geometry of our devices. We find that for an optimized SQUID geometry a continuous detection of magnetic moments down to a spin sensitivity $S_\mu^{1/2}$ of a few $\mu_B\ \mathrm{Hz}^{-1/2}$ (μ_B is the Bohr magneton) is feasible if a magnetic particle is placed 10 nm above the center of the constriction, with its magnetic moment oriented in the plane of the SQUID loop and perpendicular to the grain boundary.

2. nanoSQUID design

The layout of the nanoSQUID (top view) is shown in figure 1. The SQUID structure is patterned in a YBCO thin film of thickness d, covered by a thin Au film with thickness d_{Au}. The two bridges straddling the grain boundary have a width w_J and length l_J. The upper part of the SQUID loop contains a constriction of width w_c and length l_c. An applied bias current I_b is flowing from top to bottom across the two GBJs. A small magnetic particle can be placed on top of the constriction, and an in-plane magnetic field (perpendicular to the grain

boundary, i.e. along the y-direction) can be applied without significant suppression of the critical current I_0 of the two GBJs.

Optimizing the SQUID for spin sensitivity means to minimize the ratio S_Φ/ϕ_μ^2. The coupling factor ϕ_μ is essentially determined by the geometry of the constriction, i.e., its width w_c and thickness d. S_Φ depends on the SQUID inductance L and on the junction parameters I_0, resistance R and capacitance C. If the constriction could be made not only arbitrarily thin and narrow, but also arbitrarily short, one could envision a scenario, where ϕ_μ reaches a value around $0.5\ \Phi_0/\mu_B$ [4], while, at the same time, the inductance of the constriction remains small (Φ_0 is the magnetic flux quantum). Then, S_Φ could be optimized independently by proper choice of the SQUID size and the junction properties. For the type of device we discuss here, this is certainly not the case and we thus look for an optimization, which is compatible with technological limitations. A large coupling ϕ_μ demands an as narrow and thin as possible constriction. On the other hand, for a too narrow constriction, given a fixed value of d, its inductance L_c and thus also the total inductance L of the SQUID may become too large, possibly degrading the flux noise. This may be counterbalanced by choosing a different film thickness and changing, e.g., the junction width w_J.

In the following sections, we derive explicit expressions for the dependence of ϕ_μ (section 3) and S_Φ (section 4) on various geometric and electric SQUID parameters, which then allows us to optimize S_μ (section 5).

3. Coupling factor

We numerically calculate the coupling factor $\phi_\mu = \Phi/\mu$, i.e. the flux Φ coupled into the SQUID loop by a point-like particle with magnetic moment μ, using the software package 3D-MLSI. This routine takes explicitly into account the geometry in the plane of the SQUID loop (see figure 1), and is based on the numerical simulation of the two-dimensional (2D) sheet current density distribution $j_{2D}(x, y)$ in the SQUID loop, using London theory with λ_L and d (and hence the effective penetration depth in the thin film limit) as adjustable parameters [30].

3.1. Methods

Three different methods, which are briefly described in the following, have been developed to calculate ϕ_μ.

Method 1. With 3D-MLSI we choose an arbitrary value for the total current J circulating around the SQUID hole and calculate the corresponding sheet current density distribution $j_{2D}(x, y)$ in the SQUID loop. The resulting $j_{2D}(x, y)$ is then used to calculate the three-dimensional (3D) magnetic field distribution $\boldsymbol{B}(\boldsymbol{r})$ generated by J. The coupling factor is then obtained from the relation

$$\phi_\mu(\boldsymbol{r}, \hat{\boldsymbol{e}}_\mu) = -\hat{\boldsymbol{e}}_\mu \cdot \boldsymbol{B}(\boldsymbol{r})/J \qquad (1)$$

which was derived in [28]. Here, $\hat{\boldsymbol{e}}_\mu$ is the unit vector along the direction of the magnetic moment $\boldsymbol{\mu} = \mu\,\hat{\boldsymbol{e}}_\mu$ at position $\boldsymbol{r}$. This means that equation (1) provides ϕ_μ for any given position $\boldsymbol{r}$ and orientation $\hat{\boldsymbol{e}}_\mu$ of a point-like magnetic particle.

To capture variations of $\boldsymbol{B}$ with film thickness d, we simply assume that the circulating current J flows within a number n of 2D sheets in the x–y-plane, stacked equidistantly along the z-axis from the upper surface (at $z = 0$) to the lower surface (at $z = -d$) of the SQUID loop. The resulting field $\boldsymbol{B}(\boldsymbol{r})$ is obtained by averaging the individual fields generated by the sheets.

In our earlier work (see [31] and references therein) we used $n = 2$, which corresponds to a circulating current flow only in the upper and lower surface sheet of the SQUID loop. This approach works well if d is small enough. However, if one is interested in the scaling of ϕ_μ with d one should use a larger value for n, which provides a better approximation of a homogeneous current density distribution within the entire film thickness in z-direction, in particular for relatively large d. Since for YBCO $\lambda_L \approx 0.7\ \mu$m along the c-axis (here, the z-direction), we expect such a homogenous current distribution along $\hat{\boldsymbol{e}}_z$ for a technologically reasonable thickness ($d \lesssim 0.5\ \mu$m).

Method 2. The expression for the coupling factor ϕ_μ from equation (1), as used for method 1 does not take into account modifications of $j_{2D}(x, y)$ due to the strongly inhomogeneous dipole field in close vicinity to the magnetic particle. Such a modification, however, may become important when the distance between the point-like dipole and the SQUID surface is smaller than the film thickness d. Within method 2, we achieve a better description of the near-field regime by calculating (with 3D-MLSI) the fluxoid $\Phi_{\text{fluxoid}}(\boldsymbol{r})$ in the SQUID loop, which is induced by a 'quasi-dipole' (mimicking a small magnetic particle at position $\boldsymbol{r}$) with a magnetic moment of $1\ \mu_B$. With this we obtain $\phi_\mu(\boldsymbol{r}) = \Phi_{\text{fluxoid}}(\boldsymbol{r})/\mu_B$. Such a quasi-dipole can be constructed by a properly adjusted circulating current in a tiny loop placed at position $\boldsymbol{r}$. However, in this case, the orientation $\hat{\boldsymbol{e}}_\mu$ of the magnetic moment of the quasi-dipole is now fixed by the design of this tiny loop, implemented in 3D-MLSI, which allows only to construct 2D structures in the x–y-plane.

For instance a quasi-dipole with its magnetic moment oriented along the z-axis (i.e. $\hat{\boldsymbol{e}}_\mu = \hat{\boldsymbol{e}}_z$) can be realized by a current circulating in a tiny ring in the x–y-plane. Due to the layout of the nanoSQUID considered in this work, it is however more favorable to construct a dipole with magnetic moment pointing in y-direction. Unfortunately, it is not possible to build a corresponding ring within 3D-MLSI. Instead, we consider two strips (2D current sheets) lying on top of each other with separation $\Delta z = 3$ nm along the z-axis. Both strips expand 4 nm and 2 nm in x- and y-direction, respectively. Currents flowing along $\hat{\boldsymbol{e}}_x$ ($-\hat{\boldsymbol{e}}_x$) in the upper (lower) strip create a quasi-dipole field with a magnetic moment oriented along $\hat{\boldsymbol{e}}_y$. The currents were adjusted to generate the magnetic field distribution of a single μ_B. Furthermore the two strips are regarded as normal conductors by setting $\lambda_L \to \infty$. The quasi-dipole does not provide the field distribution of an ideal dipole (from a point-like particle) since

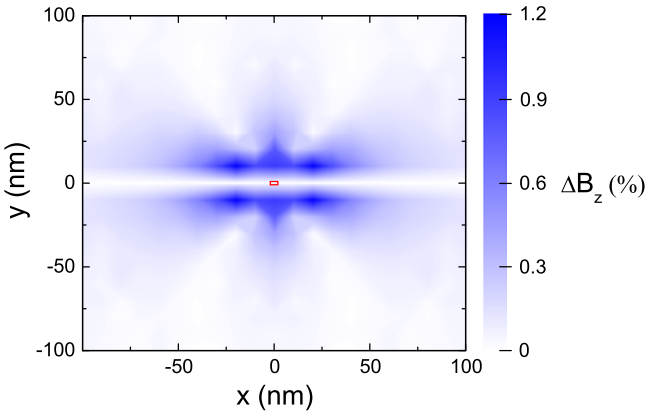

Figure 2. Distribution of normalized difference $\Delta B_z(x, y)$ in the z-components of the quasi-dipole vs ideal dipole fields at $z = 0$, with both dipoles centered at $(0, 0, z_0 = 10\,\text{nm})$. The small rectangle in the center indicates size and position of the two strips (stacked on top of each other) forming the quasi-dipole.

the two strips are not connected. However, the field generated by the missing links should be of minor relevance since it neither interacts with the superconducting structure nor with the SQUID hole. In figure 2 we plot the relative deviation ΔB_z between the z-component of the magnetic field $B_{z,\text{qd}}$ created by the quasi-dipole and $B_{z,\text{d}}$ of an ideal dipole

$$\Delta B_z = \left| \frac{B_{z,\text{qd}} - B_{z,\text{d}}}{B_{z,\text{d}}} \right| \tag{2}$$

in the x–y-plane at $z = 0$, with both dipoles centered at $\boldsymbol{r}_0 = (0, 0, z_0 = 10\,\text{nm})$ and with an orientation of their magnetic moment along the y-axis. As expected, the quasi-dipole is a very good approximation to an ideal magnetic dipole in the far field regime. In the near field regime one finds minor deviations of $\Delta B_{z,\text{max}} \approx 1.2\%$, which presumably arise from the finite volume of the quasi-dipole.

For the nanoSQUID structure, the effect of (ideal) flux focussing is taken into consideration by setting the net current J circulating around the hole to zero. The calculation is deployed for $n = 11$ current sheets and the resulting fluxoids are averaged in a similar way as for method 1.

Method 3. For this method we again examine the interaction of the quasi-dipole with the SQUID loop. In contrast to method 2, (ideal) screening is taken into consideration by setting the fluxoid in the loop to zero. In other words, a circulating current J is induced in the loop, which counterbalances the coupled flux of the quasi-dipole, due to the diamagnetic response of the SQUID. The coupling factor is obtained by computing L of the bare SQUID within 3D-MLSI and calculating $\phi_\mu(\boldsymbol{r}) = \Phi_{\text{fluxoid}}(\boldsymbol{r})/\mu_\text{B} = LJ/\mu_\text{B}$. As before, the calculation is performed for $n = 11$ current sheets. We note that method 3 is very similar to the method used by Koch *et al* [32] for the calculation of the coupling between an electron magnetic moment and a SQUID.

3.2. Comparison of methods

To compare the three methods, we calculate ϕ_μ for a particle with its magnetic moment oriented along $\hat{e}_y$, which corresponds to the optimum direction of the applied external magnetic field for our SQUID design. In all cases, we find a maximum in $\phi_\mu(\boldsymbol{r})$ if the dipole is placed as close as possible on top of the constriction at its center in the x–y-plane. For the following considerations, we set the origin of our coordinate system at the center of the constriction in the x–y-plane at the upper surface of the superconducting film.

Assuming that the particle is placed at the position $\boldsymbol{r}_0 = (0, 0, z_0)$ with $z_0 = 10\,\text{nm}$ above the constriction (without an Au layer, which can be removed without affecting the junction properties), we calculate $\phi_\mu(d)$ in the range $10\,\text{nm} \leqslant d \leqslant 500\,\text{nm}$ for the three presented methods (see figure 3(a)).

For method 1, with $n = 2$ current sheets, $\phi_\mu(d)$ saturates for $d \gtrsim 200\,\text{nm}$ to $\phi_{\mu,\text{s}} \approx \frac{1}{2}\phi_\mu(d = 10\,\text{nm})$. Since the current J is circulating in sheets at the lower $(z = -d)$ and upper $(z = 0)$ surface of the superconductor, the field $B_y(z_0 = 10\,\text{nm})$ induced by the lower sheet decays as d increases. However, the field induced by the upper sheet remains constant and thus the mean value of B_y as well, as soon as the contribution from the lower sheet becomes negligible for large enough d. Obviously, the saturation in $\phi_\mu(d)$ is an artefact stemming from the simple approximation of the current distribution along $\hat{\boldsymbol{e}}_z$ by the currents in only two surface sheets.

Turning to method 1 with $n = 11$ current sheets, the unphysical saturation of $\phi_\mu(d)$ is eliminated. Similar calculations with $n = 101$ and $n = 1001$ reveal the same behavior of $\phi_\mu(d)$ for the range of thickness shown. As expected, method 1 with $n = 2$ and $n = 11$ yields the same $\phi_\mu(d)$ for very small d.

Albeit method 1 provides a sensible approximation of ϕ_μ for currents flowing across the entire film thickness if n is large enough, it does not incorporate the effect of local screening currents induced by a magnetic particle in close proximity to the SQUID. This becomes obvious by comparison of the current distributions in the region of the constriction, as shown for method 1 in figure 3(b) and for methods 2 and 3 in figures 3(c) and 3(d), respectively. The latter two feature a more complex current distribution, arising from local screening currents. The corresponding dependence $\phi_\mu(d)$ for method 2 and 3 (see figure 3(a)), however, show qualitatively and quantitatively the same behavior as for method 1 (with $n = 11$). Accordingly, the local screening currents taken into account in method 2 and 3 do not alter ϕ_μ in the near field regime as compared to method 1.

Concluding this section, we have shown that all three methods constitute a valid approach for calculating the coupling factor, since each technique gives the same dependence $\phi_\mu(d, w_\text{c})$ for large enough values of n. Furthermore, we note that these methods can also be applied to calculations of ϕ_μ for other nanoSQUID designs, including constriction-type or planar sandwich-type junctions, which would facilitate optimization of their spin sensitivity and comparison of different designs.

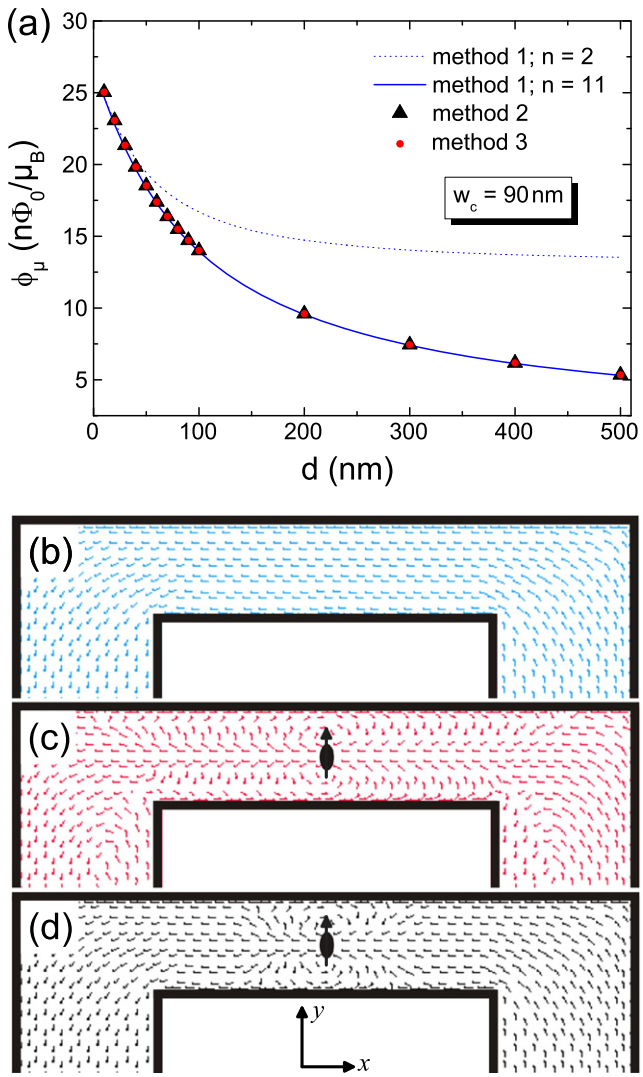

Figure 3. Comparison of methods used for calculating the coupling factor and current distribution in a $w_c = 90$ nm wide constriction (for $\lambda_L = 250$ nm). (a) $\phi_\mu(d)$ for a particle at $z_0 = 10$ nm; position and direction of magnetic moment is indicated in (c) and (d). (b)–(d) 3D-MLSI output of the current distribution in the x–y-plane calculated with (b) method 1 (identical distribution for all n sheets), (c) method 2 and (d) method 3 (for uppermost sheet at $z = 0$). Arrows indicate the local direction of currents.

3.3. Results

As already mentioned in section 2, the coupling factor should also depend on the width of the constriction. Hence, we computed ϕ_μ in the range 10 nm $\leqslant w_c \leqslant$ 500 nm and 10 nm $\leqslant d \leqslant$ 500 nm, assuming that the quasi-dipole is placed 10 nm above the center of the constriction, as in the previous section. The numerical results can be approximated by

$$\phi_\mu(d, w_c) \approx \frac{\phi_{\mu,0}}{\left(1 + \frac{d}{d_0}\right)\left(1 + \frac{w_c}{w_0}\right)}, \tag{3}$$

with the values for the fitting parameters $\phi_{\mu,0}$, d_0 and w_0 given in table 1 for two different values of λ_L. As expected, ϕ_μ decreases with increasing width w_c and thickness d. Within the simulation range, we find a monotonic decrease of $\phi_\mu(d, w_c)$, with a slightly weaker decay in $\phi_\mu(d)$ as for $\phi_\mu(w_c)$.

By modifying the distance z_0 between the magnetic particle and the upper surface of the superconductor, we find qualitatively the same dependence as in equation (3) within 10 nm $\leqslant z_0 \leqslant$ 1000 nm with absolute values scaling like $\phi_\mu(z_0) \propto z_0^{-3/2}$. Since the optimization of ϕ_μ does only trivially depend on the distance between particle and SQUID, we can absorb $\phi_\mu(z_0)$ into $\phi_{\mu,0}$.

4. Flux noise

To determine the flux noise of the SQUID in the thermal white noise regime, we use the theoretical expression obtained from Langevin simulations

$$S_\Phi = f(\beta_L)\Phi_0 k_B T L / I_0 R, \tag{4}$$

which is valid for a Stewart–McCumber parameter $\beta_C \equiv 2\pi I_0 R^2 C/\Phi_0 \lesssim 1$ and $\Gamma\beta_L < 0.1$ [33]. Here, $\Gamma \equiv 2\pi k_B T/I_0\Phi_0$ is the noise parameter, and $\beta_L \equiv 2LI_0/\Phi_0$ is the screening parameter. For $\beta_L > 0.4$, $f(\beta_L) \approx 4(1 + \beta_L)$. For lower values of β_L, S_Φ increases.

The first factor to be discussed is I_0R. The junction resistance R can be varied to some extent by varying the thickness d_{Au} of the Au layer covering the YBCO film; the maximum achievable value is the unshunted junction normal state resistance R_N (for $d_{Au} = 0$). For 24° YBCO grain boundary junctions, I_0R_N values ~2 − 3 mV are achievable at 4.2 K [34]. However, such junctions typically have hysteretic IVCs. We thus demand $\beta_C \lesssim 1$ to avoid hysteresis. Ideally, one would like to derive an expression for I_0R as a function of w_J, d and d_{Au} using the constraint $\beta_C \lesssim 1$ and assuming certain values for the critical current density j_0, unshunted normal junction resistance times area $\rho \equiv R_N w_J d$ and capacitance per junction area C'. However, the scaling of R with w_J, d and d_{Au} is currently not known. Furthermore, an estimate of C' as a function of w_J and d, based on various scaling laws available in literature [35–37] is quite difficult, in particular since it is difficult to determine C for underdamped YBCO GBJs and since the stray capacitance due to the commonly used $SrTiO_3$ substrates may play an important role [38]. On the other hand, we have fabricated nanoSQUIDs from 24° YBCO GBJs with different junction widths 85 $\leqslant w_J \leqslant$ 440 nm and film thicknesses 50, 100, 120 and 300 nm, using the focused ion beam (FIB) milling technique as described in [29]. Parameters of some of those devices are listed in table 2. Except for the devices with both, small film thickness ($d = 50$ nm) and narrow junctions ($w_J \approx 100$ nm), which tend to have slightly lower I_0R and j_0, typical values for our devices are $I_0R \approx 0.5$ mV and $j_0 = 3 - 5$ mA μm^{-2} at $T = 4.2$ K. Below we will find an optimum junction width well above 100 nm and a very weak dependence of the optimum spin sensitivity on film thickness for

Table 1. Summary of fit parameters from numerical simulations on nanoSQUIDs for two different values of λ_L. The values for $S_{\Phi,0}^{1/2}$ and $S_{\mu,0}^{1/2}$ are given for $T = 4.2$ K and $I_0R = 0.5$ mV.

λ_L (nm)	$\phi_{\mu,0}$ ($n\Phi_0/\mu_B$)	d_0 (nm)	w_0 (nm)	w_c' (nm)	L' (pH·nm)	L_e' (pH·nm)	L_b' (pH·nm)	L_b'' (pH·nm)	b	r	L'/d_0 (pH)	$S_{\Phi,0}^{1/2}$ ($n\Phi_0$ $Hz^{-1/2}$)	$S_{\mu,0}^{1/2}$ (μ_B $Hz^{-1/2}$)
250	49	120	102	7	85	56	25	120	0.29	2.73	0.71	12.6	0.26
335	78	83	53	4.8	143	100	45	150	0.31	2.45	1.72	19.7	0.25

100 nm $\lesssim d \lesssim$ 500 nm. Thus, rather than introducing an ill-defined scaling of I_0R with w_J and d, below we fix $I_0R = 0.5$ mV and $j_0 = 3$ mAμm^{-2} as realistic values.

We next determine the dependence of the SQUID inductance L on the various geometrical parameters. We separate the SQUID into the constriction (inductance L_c, length l_c, width w_c), the two (symmetric) bridges containing the junctions (inductance L_J, length l_J, width w_J), the two corners connecting the constriction and the junction arms (inductance L_e), and the bottom part of the SQUID (inductance L_b), as indicated in figure 1. Then, L is given by

$$L = L_c + 2L_J + 2L_e + L_b. \tag{5}$$

We should find $L_c(w_c, l_c, d)$, $L_J(w_J, l_J, d)$, $L_e(w_c, w_J, d)$ and $L_b(l_c, w_J, d)$. From 3D-MLSI simulations we find the parametrization $L_c(w_c, l_c, d) \approx L' \cdot l_c/w_c d$. This expression fits the computed L_c well, within the parameter range 10 nm $\leqslant l_c, w_c, d \leqslant$ 500 nm, covered by the simulations. We use the same parametrization for $L_J(w_J, l_J, d)$. For the corners we find, within a 15% variation with respect to w_J and w_c, the expression $L_e \approx L_e'/d$. Finally, we find $L_b \approx L_b' l_c/w_J d + L_b''/d$. The fitting parameters L', L_e', L_b' and L_b'' are summarized in table 1 for two different values of λ_L. Inserting these expressions into equation (5) yields

$$L \approx \frac{L'}{d}\left\{\frac{l_c}{w_c} + \frac{2l_J + bl_c}{w_J} + r\right\}, \tag{6}$$

with $b \equiv L_b'/L'$ and $r \equiv (2L_e' + L_b'')/L'$ (see table 1). We note that in our simulations we have adjusted $\lambda_L = 250$ nm to be consistent with most of the experimentally determined values of L for our nanoSQUIDs. This value is consistent with the literature on λ_L in the a–b-plane of epitaxially grown c-axis oriented YBCO thin films [25, 39]. However, for some devices we find good agreement between measured and simulated values of L only if we assume larger values for λ_L, e.g. $\lambda_L = 335$ nm for 'exp. device 1a'[1] listed in table 2.

For the minimization of S_μ, we will use β_L as a variable parameter. Since both, L and w_J are not independent of each other and are related to β_L, we express both as functions of β_L. This will allow us to eliminate L and w_J in the final expression for S_μ which has to be optimized. With $\beta_L = 2I_0L/\Phi_0$ and $I_0 = j_0 w_J d$, we obtain

$$w_J(\beta_L, L) = \frac{\Phi_0\beta_L}{2j_0 dL}. \tag{7}$$

[1] 'Exp. device 1a' corresponds to the YBCO nanoSQUID which has been described in [29]. Due to our refined calculation of the coupling factor ϕ_μ (i.e. using $n = 11$ instead of $n = 2$ current sheets), we find a ~14 % reduction of the calculated value for ϕ_μ, and correspondingly a slightly larger value for $S_\mu^{1/2}$, as compared to the values quoted in [29]. Our choice of $\lambda_L = 250$ nm for the calculation of ϕ_μ (instead of 335 nm in [29]) has a negligible effect on the calculated value of ϕ_μ for this device.

Inserting this into equation (6) yields

$$L(\beta_L) \approx \frac{L'}{d}\left(\frac{l_c}{w_c} + r\right)\left\{1 - \frac{\kappa}{\beta_L}\right\}^{-1}, \tag{8}$$

with

$$\kappa(l_J, l_c, j_0) \equiv 2(2l_J + bl_c)j_0 L'/\Phi_0. \tag{9}$$

Inserting equation (8) into equation (4) and using $f(\beta_L) = 4(1 + \beta_L)$ finally yields

$$S_\Phi(d, w_c, \beta_L) \approx S_{\Phi,0}\frac{d_0}{d}\left(\frac{l_c}{w_c} + r\right)\frac{1 + \beta_L}{1 - \frac{\kappa}{\beta_L}}, \tag{10}$$

with $S_{\Phi,0}^{1/2} \equiv 2\sqrt{\frac{\Phi_0 k_B T L'}{I_0 R d_0}}$ (see table 1). The most important result here is the scaling $S_\Phi \propto 1/d$. This is due to the fact that the SQUID inductance $L \propto 1/d$ within the simulation range for d, because of the increase of the kinetic inductance contribution with decreasing d below λ_L. For $d \gtrsim 2\lambda_L$ we expect a saturation of $L(d)$ and hence of $S_\Phi(d)$. However, we will neglect this for the optimization of S_μ, since values for $d \gtrsim$ 500 nm are outside the simulation range and since we cannot expect to produce high-quality GBJs for such large values of d.

5. Optimization of spin sensitivity via improved SQUID geometry

With equation (3) and (10) we find the spin sensitivity $S_\mu^{1/2} = S_\Phi^{1/2}/\phi_\mu$. The individual dependencies on d, β_L and constriction parameters w_c and l_c can be separated. Hence, we can express the spin sensitivity as

$$S_\mu^{1/2}(d, w_c, \beta_L) = S_{\mu,0}^{1/2} \cdot s_d(d) \cdot s_{\beta_L}(\beta_L) \cdot s_c(w_c, l_c), \tag{11}$$

with $S_{\mu,0}^{1/2} \equiv S_{\Phi,0}^{1/2}/\phi_{\mu,0}$ (see table 1) and with

$$s_d(d) \equiv \sqrt{\frac{d_0}{d}} + \sqrt{\frac{d}{d_0}}, \tag{12}$$

$$s_{\beta_L}(\beta_L) \equiv \sqrt{\frac{1 + \beta_L}{1 - \frac{\kappa}{\beta_L}}}, \tag{13}$$

$$s_c(w_c, l_c) \equiv \left(1 + \frac{w_c}{w_0}\right)\sqrt{\frac{l_c}{w_c} + r}. \tag{14}$$

Figure 4 shows $s_d(d)$, $s_{\beta_L}(\beta_L)$ for fixed κ, and $s_c(w_c)$ and $s_c(l_c)$ for fixed l_c and w_c, respectively, for $\lambda_L = 250$ nm. In the following we discuss the optimum choice of the various parameters.

For $s_d(d)$ from equation (12) we obtain a shallow minimum at $d_{min} = d_0$, and a rather weak dependence for $d \gtrsim$ 100 nm. This indicates that with increasing d above ~100 nm the decrease in kinetic inductance (and hence in flux noise) and coupling factor almost compensate each other within the simulation range. Hence, the optimization of the spin sensitivity with respect to film thickness is

Table 2. Summary of geometric and electric nanoSQUID parameters (as defined in the text). The values for 'opt. device 1' are calculated for optimized parameters obtained for a given constriction length l_c, with $\lambda_L = 250$ nm. For 'opt. device 2' we used more relaxed values for w_c, l_c and l_J and otherwise identical input parameters for d, j_0, I_0R, λ_L with correspondingly optimized β_L and adjusted w_J. For the experimental devices we quote experimentally determined values for L and $S_\Phi^{1/2}$ (in the thermal white noise limit) [40] together with values (in brackets) which are calculated with equation (6) and (4), respectively, with $\lambda_L = 250$ nm. Here, the flux noise was calculated based on the measured SQUID inductance L. Accordingly, the values in brackets for the spin sensitivity $S_\mu^{1/2}$ are based on the calculated values for the flux noise $S_\Phi^{1/2}$.

	d	l_c	l_J	w_c	w_J	β_L	L	I_0	R	I_0R	j_0	L_c	L_J	L_e	L_b	$S_\Phi^{1/2}$	ϕ_μ	$S_\mu^{1/2}$
Units	nm	nm	nm	nm	nm		pH	μA	Ω	mV	mA μm^{-2}	pH	pH	pH	pH	nΦ_0 Hz$^{-1/2}$	nΦ_0/μ_B	μ_B Hz$^{-1/2}$
opt. device1	120	44	174	25	280	0.40	4.1	101	5.0	0.5	3	1.3	0.44	0.47	1.0	36	20	1.8
opt. device2	120	100	200	60	316	0.45	4.1	114	4.4	0.5	3	1.2	0.45	0.47	1.1	36	15	2.4
exp. device1a	50	300	400	90	130	0.65	36 (22)	18.5	7.0	0.13	2.85	5.7	5.2	1.1	3.6	1300 (228)	18	71 (12)
exp. device1b	50	535	435	50	85	1.29	42 (43)	31.4	10.2	0.32	7.39	18	8.7	1.1	5.6	600 (185)	23	26 (8.0)
exp. device2a	100	500	500	420	190	0.78	8.9 (8.5)	91	5.4	0.49	4.79	1.0	2.2	0.56	1.9	450 (60)	5.2	86 (11)
exp. device2b	100	475	455	410	140	1.37	9.1 (9.7)	155	3.1	0.47	11.0	0.98	2.8	0.56	2.0	400 (72)	5.3	75 (13)
exp. device3	120	230	370	100	205	0.94	5.8 (6.4)	168	5.0	0.84	6.81	1.6	1.3	0.47	1.2	<83 (39)	12	<6.7 (3.1)
exp. device4a	300	300	450	120	280	0.87	2.9 (2.5)	315	1.4	0.44	3.75	0.71	0.46	0.19	0.49	240 (37)	6.4	37 (5.7)
exp. device4b	300	485	480	195	285	1.01	2.2 (2.6)	471	1.7	0.78	5.51	0.70	0.48	0.19	0.54	<240 (25)	4.8	<50 (5.3)

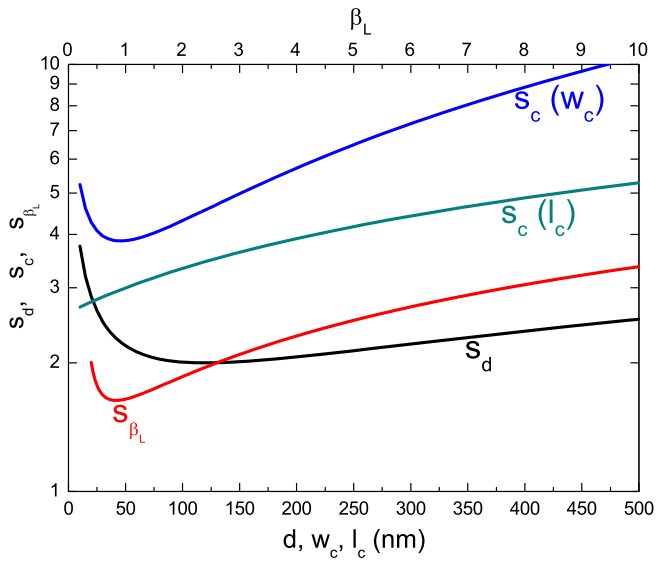

Figure 4. Scaling of the terms $s_d(d)$, $s_{\beta_L}(\beta_L)$ for $\kappa = 0.26$, $s_c(w_c)$ for $l_c = 200$ nm and $s_c(l_c)$ for $w_c = 60$ nm, which enter the spin sensitivity in equation (11) as calculated from equation (12)–(14) with $\lambda_L = 250$ nm.

straightforward, although, the proper choice of d is not very crucial as long as $d \gtrsim 100$ nm. However, in order to avoid too large aspect ratios d/w_c and d/w_J, it is advisable to fix the optimum film thickness to $d_{opt} = d_{min}$. This in turn fixes the optimum value for s_d according to equation (12) to

$$s_{d,opt} = s_d(d_{min}) = 2. \tag{15}$$

The evaluation of equation (13) shows a much more pronounced dependence for $s_{\beta_L}(\beta_L)$ with a clear minimum at $\beta_{L,min} = \kappa(1 + \sqrt{1 + \kappa^{-1}})$, and $s_{\beta_L}(\beta_{L,min}) = \sqrt{\kappa} + \sqrt{\kappa + 1}$. For $\kappa = 0.26$ used in figure 4, we obtain $\beta_{L,min} \approx 0.83$ and $s_{\beta_L}(\beta_{L,min}) \approx 1.6$. Both, $\beta_{L,min}(\kappa)$ and $s_{\beta_L}(\beta_{L,min})$ decrease monotonically with decreasing κ, which implies that κ should be as small as possible. However, as mentioned above, for $\beta_L < 0.4$ the flux noise increases again with further decreasing β_L, and equation (13) is not applicable. Hence, the optimum value for β_L is $\beta_{L,opt} = 0.4$, which then fixes the optimum value for κ via the relation $\beta_{L,min}(\kappa)$ to

$$\kappa_{opt} = \frac{\beta_{L,\,opt}^2}{1 + 2\beta_{L,opt}} = \frac{4}{45} \approx 0.09. \tag{16}$$

Accordingly, the optimum value for s_{β_L} in equation (13) yields

$$s_{\beta_L,opt} = s_{\beta_L}(\beta_{L,opt}, \kappa_{opt}) = \frac{3}{\sqrt{5}} \approx 1.3. \tag{17}$$

We note that according to equation (9), the choice of $\kappa = \kappa_{opt}$ relates the optimum length $l_{J,opt}$ of the bridges containing the GBJs and l_c via

$$l_{J,opt} = \frac{\kappa_{opt}\Phi_0}{4j_0L'} - \frac{b}{2}l_c. \tag{18}$$

Since $b/2 \approx 0.15 \ll 1$, the dependence $l_{J,opt}(l_c)$ is quite weak. For our choice of $j_0 = 3$ mA μm^{-2} and with $\lambda_L = 250$ nm, equation (18) yields $l_{J,opt} \approx 180$ nm $- 0.15 l_c$, i.e. $l_{J,opt}$ decreases only slightly from ~180 nm to ~150 nm for $l_c = 0$ to 200 nm. Hence, the choice of l_c (together with j_0 and λ_L) fixes $l_{J,opt}$.

By inserting $d = d_{opt} = d_0$, $\beta_L = \beta_{L,opt}$ and $\kappa = \kappa_{opt}$ into equation (8), we find for the optimized SQUID inductance

$$L_{opt} \approx 1.3\,\frac{L'}{d_0}\left(r + \frac{l_c}{w_c}\right), \tag{19}$$

i.e. $L_{opt} \approx 2.5$ pH $+ 0.91$ pH $\cdot \frac{l_c}{w_c}$ for $\lambda_L = 250$ nm and roughly a factor of two larger values for $\lambda_L = 335$ nm. Inserting this into equation (7), we find for the optimum junction width

$$w_{J,opt} = \frac{7\Phi_0}{45L'j_0}\,\frac{1}{r + \frac{l_c}{w_c}}. \tag{20}$$

For our choice of $j_0 = 3$ mA μm^{-2}, the prefactor in equation (20) is ≈1.26 μm (750 nm) for $\lambda_L = 250$ (335) nm; i.e. the optimum junction width decreases monotonically with increasing ratio l_c/w_c from ~340 (270) nm for $l_c/w_c = 1$ to ~100 (60)nm for $l_c/w_c = 10$, with $\lambda_L = 250$ (335)nm. For our choice of $j_0 = 3$ mA$/\mu$m^2, the prefactor in equation (20) is ≈1.26 μm (750 nm) for $\lambda_L = 250$ (335) nm; i.e. the optimum junction width decreases monotonically with increasing ratio l_c/w_c from ~340 (270) nm for $l_c/w_c = 1$ to ~100 (60)nm for $l_c/w_c = 10$, with $\lambda_L = 250$ (335)nm.

Finally, as shown in figure 4, the relation $s_c(w_c, l_c)$, given by equation (14) yields a monotonic decrease of s_c with decreasing l_c and a clear minimum in $s_c(w_c)$ at

$$w_{c,min} = \frac{l_c}{4r}\left(\sqrt{1 + \frac{8rw_0}{l_c}} - 1\right), \tag{21}$$

which can be approximated by a power law dependence $w_{c,min} \approx w_c' \cdot (l_c/\text{nm})^{0.35}$ (see dashed and dotted lines in figure 5) with $w_c' = 7$ (4.8) nm for $\lambda_L = 250$ (335) nm. Accordingly, s_c can be minimized by choosing $w_c = w_{c,min}(l_c)$. This yields

$$s_{c,opt}(l_c) = \left\{1 + \frac{w_c'}{w_0}\left(\frac{l_c}{\text{nm}}\right)^{0.35}\right\}\sqrt{r + \frac{\text{nm}}{w_c'}\left(\frac{l_c}{\text{nm}}\right)^{0.65}}. \tag{22}$$

Both, $w_{c,min}(l_c)$ and $s_{c,opt}(l_c)$ decrease monotonically with decreasing l_c. This implies that l_c should be made as small as possible.

All numbers in the following paragraph are quoted for $\lambda_L = 250$ nm. For $l_c = 500$ nm we find $w_{c,min} \approx 60$, which is feasible to realize with our FIB technology; however upon shrinking l_c it becomes increasingly hard to realize devices with optimum constriction width $w_{c,min}(l_c)$. Fortunately, it

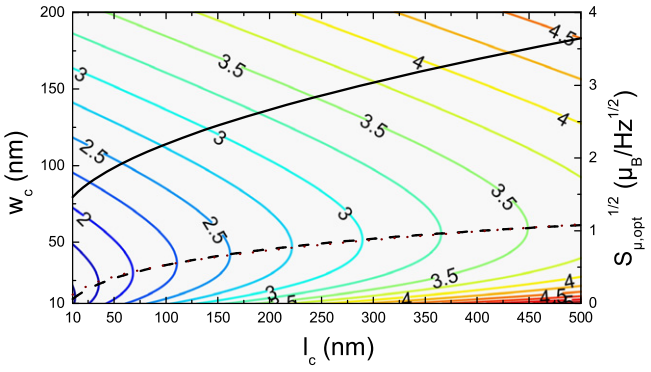

Figure 5. Contour plot of optimized spin sensitivity $S^{1/2}_{\mu,\,\mathrm{opt}}(l_\mathrm{c},\, w_\mathrm{c})$ (for $T = 4.2$ K, $I_0R = 0.5$ mV, $d = 120$ nm and $\beta_L = 0.4$). Numbers at contour lines are in units of $\mu_\mathrm{B}\mathrm{Hz}^{-1/2}$. Dashed and dotted lines show $w_{\mathrm{c,min}}\,(l_\mathrm{c})$ from equation (21) and approximation by power law dependence, respectively. The solid black line shows $S^{1/2}_{\mu,\,\mathrm{opt}}(l_\mathrm{c})$ for $w_\mathrm{c} = w_{\mathrm{c,min}}$. All quantities were calculated for $\lambda_\mathrm{L} = 250$ nm.

turns out that the degradation in spin sensitivity is not very severe if w_c deviates from $w_{\mathrm{c,min}}$, as long as one can keep w_c below, say, 100 nm. This is illustrated in the contour plot in figure 5, which shows the spin sensitivity for optimized d and β_L, i.e. $S^{1/2}_{\mu,\,\mathrm{opt}}(l_\mathrm{c},\, w_\mathrm{c}) = S^{1/2}_{\mu,\,0} \cdot s_{d,\mathrm{opt}} \cdot s_{\beta_L,\mathrm{opt}} \cdot s_\mathrm{c}(l_\mathrm{c},\, w_\mathrm{c}) \approx 0.69\,\mu_\mathrm{B}\,\mathrm{Hz}^{-1/2} \cdot s_\mathrm{c}(l_\mathrm{c},\, w_\mathrm{c})$ for $T = 4.2$ K and $I_0R = 0.5$ mV. Within the plotted range, the spin sensitivity lies in most cases between 2 and 4 $\mu_\mathrm{B}\,\mathrm{Hz}^{-1/2}$, and practically for an optimized device the spin sensitivity is limited by both, the smallest length and linewidth which can be realized for the constriction. The solid line in figure 5 shows $s_{\mathrm{c,opt}}(l_\mathrm{c})$ according to equation (22), i.e. with the additional condition $w_\mathrm{c} = w_{\mathrm{c,min}}\,(l_\mathrm{c})$. If we take $l_\mathrm{c} = 44$ nm, corresponding to $w_{\mathrm{c,min}} = 25$ nm as the current limitation for our FIB patterning technology, we calculate $S^{1/2}_{\Phi,\,\mathrm{opt}} \approx 36\,\mathrm{n}\Phi_0\,\mathrm{Hz}^{-1/2}$ and $\phi_{\mu,\mathrm{opt}} \approx 20\,\mathrm{n}\Phi_0/\mu_\mathrm{B}$, giving an optimized spin sensitivity $S^{1/2}_{\mu,\,\mathrm{opt}} \approx 1.8\,\mu_\mathrm{B}\,\mathrm{Hz}^{-1/2}$. Corresponding SQUID parameters are listed in table 2 ('opt. device 1'). If we take more easily achievable values $w_\mathrm{c} = 60$ nm, $l_\mathrm{c} = 100$ nm and $l_\mathrm{J} = 200$ nm (other input parameters are the same as for the initial optimization), we still get $S^{1/2}_{\mu} = 2.4\,\mu_\mathrm{B}\,\mathrm{Hz}^{-1/2}$ (see table 2 for parameters of 'opt. device 2').

6. Discussion

In the following, we discuss some practical issues regarding the realization of optimized YBCO GBJ nanoSQUIDs. The optimization of the spin sensitivity given by equation (11) certainly depends on the control over the various input parameters, which are not always known precisely. For example, I_0R and j_0 of YBCO GBJs can vary significantly, even on the same chip [34], and sometimes we find values for λ_L significantly above 250 nm.

Starting with the prefactor $S^{1/2}_{\mu,\,0}$, this depends on T and I_0R. Regarding operation temperature T, this will certainly depend on the different applications the nanoSQUIDs will be used for. Hence, this is not a parameter which should be used for optimization. Still, the use of YBCO SQUIDs based on GBJs offers operation from close to their transition temperature T_c (say, 77 K) down to the mK regime. The very large range of operation temperatures is certainly a significant advantage over nanoSQUIDs based on other materials or other junction types such as constriction junctions, which often can only be operated in a very limited temperature interval. The I_0R product does only enter into the expression for the spin sensitivity via $S_{\mu,0} \propto 1/I_0R$. Hence, any variation in I_0R does not affect the optimization of the device geometry. Obviously, as large as possible values for I_0R are helpful for improving the spin sensitivity.

The term for s_d depends on the film thickness d only, and due to the shallow minimum in $s_d(d)$, slight deviations from $d = d_\mathrm{opt} = 120$ nm (for $\lambda_\mathrm{L} = 250$ nm) or larger values for λ_L will have an almost negligible effect on $S^{1/2}_{\mu}$.

The term for s_c depends only on the geometry of the constriction and on λ_L. Here, technological limitations imposed by the patterning technique and possible edge damage effects are crucial, since the smallest achievable s_c will depend on the smallest achievable length l_c and width w_c of the constriction. For our FIB patterning technique, we currently do not know what the final limits for the minimum achievable values for l_c and w_c are, and how strong edge damage effects are. Further investigations are required to determine (and reduce) edge damage effects, which will finally limit the minimum achievable constriction size.

The term s_{β_L} depends on β_L and κ. Here, j_0 enters into the optimization only via $\kappa \propto j_0$. A variation in j_0 will modify the optimum length $l_{\mathrm{J,opt}}(j_0,\, l_\mathrm{c})$ (see equation (18)) and width $w_{\mathrm{J,opt}} \propto 1/j_0$ (see equation (20)), which are required for maintaining $\beta_L \approx 0.4$ (and hence $s_{\beta_L} = s_{\beta_L,\mathrm{opt}}$). Fortunately, j_0 can be measured prior to FIB patterning, which allows to adjust the geometry of the bridges straddling the GBJs. Hence, as long as j_0 does not change significantly after FIB milling [28], and as long as the conditions for $l_{\mathrm{J,opt}}$ and $w_{\mathrm{J,opt}}$ can be fulfilled, the optimized spin sensitivity is not affected by variations in j_0.

A variation in λ_L has a similar effect as a variation in j_0, since $\kappa \propto L'$ and L' increases with λ_L (see table 1). However, it is difficult to determine λ_L prior to FIB patterning in order to adjust w_J and l_J properly. For fixed geometrical parameters, we find that an increase in λ_L from 250 to 335 nm decreases the coupling factor only very slightly, as long as $w_\mathrm{c} \lesssim 100$ nm. The strongest effect comes from the increase in L' by a factor of ~1.7, which increases L and β_L, which both enter into the flux noise. Depending on the value of β_L, this induces an increase in $S^{1/2}_{\Phi}$ (and in $S^{1/2}_{\mu}$) by a factor of approximately 1.4–1.7.

Finally, we would like to comment on two additional practical issues. First, the predicted optimized spin sensitivity around a few $\mu_\mathrm{B}\mathrm{Hz}^{-1/2}$ is in particular due to the reduction in SQUID inductance for an optimized geometry, yielding improved flux noise. However, we should mention that for YBCO SQUIDs the measured flux noise is often significantly

higher than the theoretically predicted one [41]. For the experimental devices listed in table 2 the measured $S_\Phi^{1/2}$ was a factor 3.2–7.5 higher than predicted by equation (4). Hence, we expect the predicted spin sensitivities to be too low by a similar factor if compared with experimental results.

Second, the optimization procedure as described in this work is based on calculating the white thermal noise of the SQUIDs. However, it is well known that I_0 fluctuations can lead to a flux noise S_Φ which scales with the measurement frequency f as $1/f^\alpha$ with α typically close to 1, and it is also known that for YBCO GBJs such a $1/f$ noise contribution can be quite large [41]. For YBCO nanoSQUIDs with improved white thermal noise around 100 $n\Phi_0$ $Hz^{-1/2}$ and below, this implies that the $1/f$ noise may dominate at frequencies up to the MHz range. Hence, in order to utilize the full potential of such SQUIDs, the implementation of bias reversal schemes for suppression of $1/f$ noise from I_0 fluctuations will be very important. Furthermore, for dc SQUIDs based on metallic superconductors such as Nb, it has been shown that below $T \approx 1$ K additional sources of low-frequency excess flux noise may become important, which cannot be eliminated by bias reversal [42] (for more recent work see e.g. [43, 44] and references therein). In YBCO nanoSQUIDs also similar effects may be present and deserve further studies.

7. Conclusions

In summary, we have performed a detailed analysis of the coupling factor ϕ_μ and the spectral density of flux noise S_Φ, and hence of the spin sensitivity $S_\mu^{1/2} = S_\Phi^{1/2}/\phi_\mu$ for grain boundary junction dc nanoSQUIDs. Based on the calculation of ϕ_μ and S_Φ, we derived an explicit expression for the spin sensitivity $S_\mu^{1/2}$ as a function of the geometric and electrical parameters of our devices. This allows for an optimization of $S_\mu^{1/2}$, which predicts a spin sensitivity of a few $\mu_B Hz^{-1/2}$. Such a low value for $S_\mu^{1/2}$ can be achieved by realization of very low inductance nanoSQUIDs with ultra-low flux noise on the order of 100 $n\Phi_0$ $Hz^{-1/2}$ or even below, in the thermal white noise regime. This poses severe challenges on proper readout electronics for such SQUIDs. It remains to be shown whether or not the readout of such ultralow-noise SQUIDs is feasible and whether or not the envisaged values for the spin sensitivity can also be achieved in high fields, which is a major driving force for using these grain boundary junction nanoSQUIDs.

Acknowledgments

J Nagel and T Schwarz acknowledge support by the Carl-Zeiss-Stiftung. We gratefully acknowledge fruitful discussions with D Drung. This work was funded by the Nachwuchswissenschaftlerprogramm of the Universität Tübingen, and by the Deutsche Forschungsgemeinschaft (DFG) via projects KO 1303/13-1 and SFB/TRR 21 C2.

References

[1] Wernsdorfer W 2001 *Adv. Chem. Phys.* **118** 99
[2] Ketchen M, Awschalom D, Gallagher W, Kleinsasser A, Sandstrom R, Rozen J and Bumble B 1989 *IEEE Trans. Magn.* **25** 1212
[3] Wernsdorfer W, Mailly D and Benoit A 2000 *J. Appl. Phys.* **87** 5094
[4] Bouchiat V 2009 *Supercond. Sci. Technol.* **22** 064002
[5] Gallop J 2003 *Supercond. Sci. Technol.* **16** 1575
[6] Awschalom D D, Rozen J R, Ketchen M B, Gallagher W J, Kleinsasser A W, Sandstrom R L and Bumble B 1988 *Appl. Phys. Lett.* **53** 2108
[7] Hasselbach K, Mailly D and Kirtley J R 2002 *J. Appl. Phys.* **91** 4432
[8] Lam S K H and Tilbrook D L 2003 *Appl. Phys. Lett.* **82** 1078
[9] Cleuziou J-P, Wernsdorfer W, Bouchiat V, Ondarçuhu T and Monthioux M 2006 *Nat. Nanotechnology* **1** 53
[10] Troeman A G P, Derking H, Borger B, Pleikies J, Veldhuis D and Hilgenkamp H 2007 *Nano Lett.* **7** 2152
[11] Koshnick N C, Huber M E, Bert J A, Hicks C W, Large J, Edwards H and Moler K A 2008 *Appl. Phys. Lett.* **93** 243101
[12] Hao L, Macfarlane J C, Gallop J C, Cox D, Beyer J, Drung D and Schurig T 2008 *Appl. Phys. Lett.* **92** 192507
[13] Foley C P and Hilgenkamp H 2009 *Supercond. Sci. Technol.* **22** 064001
[14] Wernsdorfer W 2009 *Supercond. Sci. Technol.* **22** 064013
[15] Finkler A, Segev Y, Myasoedov Y, Rappaport M L, Ne'eman L, Vasyukov D, Zeldov E, Huber M E, Martin J and Yacoby A 2010 *Nano Lett.* **10** 1046
[16] Giazotto F, Peltonen J T, Meschke M and Pekola J P 2010 *Nat. Phys.* **6** 254
[17] Nagel J, Kieler O F, Weimann T, Wölbing R, Kohlmann J, Zorin A B, Kleiner R, Koelle D and Kemmler M 2011 *Appl. Phys. Lett.* **99** 032506
[18] Martínez-Pérez M J, Bellido E, de Miguel R, Sesé J, Lostao A, Gómez-Moreno C, Drung D, Schurig T, Ruiz-Molina D and Luis F 2011 *Appl. Phys. Lett.* **99** 032504
[19] Romans E J, Rozhko S, Young L, Blois A, Hao L, Cox D and Gallop J C 2011 *IEEE Trans. Appl. Supercond.* **21** 404
[20] Russo R, Granata C, Esposito E, Peddis D, Cannas C and Vettoliere A 2012 *Appl. Phys. Lett.* **101** 122601
[21] Wölbing R, Nagel J, Schwarz T, Kieler O, Weimann T, Kohlmann J, Zorin A B, Kemmler M, Kleiner R and Koelle D 2013 *Appl. Phys. Lett.* **102** 192601
[22] Granata C, Vettoliere A, Russo R, Fretto M, Leo N D and Lacquaniti V 2013 *Appl. Phys. Lett.* **103** 102602
[23] Levenson-Falk E M, Vijay R, Antler N and Siddiqi I 2013 *Supercond. Sci. Technol.* **26** 005015
[24] Vasyukov Denis *et al* 2013 *Nat. Nanotechnology* **8** 639
[25] Arpaia R, Arzeo M, Nawaz S, Charpentier S, Lombardi F and Bauch T 2014 *Appl. Phys. Lett.* **104** 072603
[26] Drung D, Storm J-H, Ruede F, Kirste A, Regin M, Schurig T, Repollés A M, Sesé J and Luis F 2014 *IEEE Trans Appl. Supercond.* **24** 1600206
[27] Chen L, Wernsdorfer W, Lampropoulos C, Christou G and Chiorescu I 2010 *Nanotechnology* **21** 405504
[28] Nagel J *et al* 2011 *Supercond. Sci. Technol.* **24** 015015
[29] Schwarz T, Nagel J, Wölbing R, Kemmler M, Kleiner R and Koelle D 2013 *ACS Nano* **7** 844
[30] Khapaev M, Kupriyanov M, Goldobin E and Siegel M 2003 *Supercond. Sci. Technol.* **16** 24
[31] Nagel J *et al* 2013 *Phys. Rev.* B **88** 064425
[32] Koch R H, DiVincenzo D P and Clarke J 2007 *Phys. Rev. Lett.* **98** 267003

[33] Chesca B, Kleiner R and Koelle D 2004 Fundamentals and Technology of SQUIDs and SQUID systems *The SQUD Handbook* ed J Clarke and A I Braginski vol 1 (Weinheim: Wiley) pp 29–92 chapter 2
[34] H Hilgenkamp and J Mannhart 2002 *Rev. Mod. Phys.* **74** 485
[35] Moeckly B H and Buhrman R A 1995 *IEEE Trans. Appl. Supecond.* **5** 3414–7
[36] McBrien P F, Hadfield R H, Booij W E, Moya A, Kahlmann F, Blamire M G, Pegrum C M and Tarte E J 2000 *Physica* C **339** 88
[37] Navacerrada M A, Lucía M L, Sánchez-Soto L L, Sánchez Quesada F, Sarnelli E and Testa G 2005 *Phys. Rev.* B **71** 014501
[38] Beck A, Froehlich O M, Koelle D, Gross R, Sato H and Naito M 1996 *Appl. Phys. Lett.* **68** 3341
[39] Zaitsev A G, Schneider R, Linker G, Ratzel F, Smithey R, Schweiss P, Geerk J, Schwab R and Heidinger R 2002 *Rev. Sci. Instrum.* **73** 335
[40] For exp. device3 and 4b, we find low-frequency excess noise up to the bandwidth of our readout electronics. Hence, we can only give an upper limit for the white thermal noise (flux noise and spin sensitivity) for these devices.
[41] Koelle D, Kleiner R, Ludwig F, Dantsker E and Clarke J 1999 *Rev. Mod. Phys.* **71** 631
[42] Wellstood F C, Urbina C and Clarke J 1987 *Appl. Phys. Lett.* **50** 772
[43] Choi S, Lee D-H, Louie S G and Clarke J 2009 *Phys. Rev. Lett.* **103** 197001
[44] Drung D, Beyer J, Storm J-H, Peters M and Schurig T 2011 *IEEE Trans. Appl. Supercond.* **21** 340

Publication 4

Low-Noise $YBa_2Cu_3O_7$ Nano-SQUIDs for Performing Magnetization-Reversal Measurements on Magnetic Nanoparticles

T. Schwarz,[1] R. Wölbing,[1] C. F. Reiche,[2] B. Müller,[1] M. J. Martínez-Pérez,[1] T. Mühl,[2] B. Büchner,[2] R. Kleiner,[1] and D. Koelle[1]

[1]*Physikalisches Institut-Experimentalphysik II and Center for Collective Quantum Phenomena in LISA$^+$, Universität Tübingen, Auf der Morgenstelle 14, D-72076 Tübingen, Germany*

[2]*Leibniz Institute for Solid State and Materials Research IFW Dresden, Helmholtzstrasse 20, 01069 Dresden, Germany*

(Received 1 October 2014; published 17 April 2015)

We fabricate $YBa_2Cu_3O_7$ (YBCO) direct-current nano- superconducting quantum-interference devices (nano-SQUIDs) based on grain-boundary Josephson junctions by focused-ion-beam patterning. Characterization of electric transport and noise properties at 4.2 K in a magnetically shielded environment yields a very small inductance L of a few pH for an optimized device geometry. This, in turn, results in very low values of flux noise $< 50\ n\Phi_0/Hz^{1/2}$ in the thermal white-noise limit, which yields spin sensitivities of a few $\mu_B/Hz^{1/2}$ (Φ_0 is the magnetic flux quantum, and μ_B is the Bohr magneton). We observe frequency-dependent excess noise up to 7 MHz, which can be eliminated only partially by bias reversal readout. This behavior indicates the presence of fluctuators of unknown origin, possibly related to defect-induced spins in the $SrTiO_3$ substrate. We demonstrate the potential of using YBCO nano-SQUIDs for the investigation of small spin systems, by placing a 39-nm-diameter Fe nanowire encapsulated in a carbon nanotube on top of a nonoptimized YBCO nano-SQUID and by measuring the magnetization reversal of the Fe nanowire via the change of magnetic flux coupled to the nano-SQUID. The measured flux signals upon magnetization reversal of the Fe nanowire are in very good agreement with estimated values, and the determined switching fields indicate magnetization reversal of the nanowire via curling mode.

DOI: 10.1103/PhysRevApplied.3.044011

I. INTRODUCTION

Small spin systems or magnetic nanoparticles (MNPs), like single-molecular magnets, nanowires, or nanotubes behave very differently from magnetic bulk material, which makes them very interesting, both for basic research and applications ranging from spintronics and spin-based quantum-information processing to industrial use of ferrofluidic devices and biomedical applications [1–7]. Because of their nanoscale size, MNPs have very small magnetic moments, which does not allow one to use standard magnetic characterization techniques for the investigation of their properties. In one approach, which has been pioneered by Wernsdorfer [8], MNPs are placed very close to miniaturized superconducting quantum-interference devices (SQUIDs), often referred to as micro-SQUIDs or nano-SQUIDs [9–25], and the magnetization reversal of MNPs is measured directly via the change of stray magnetic flux coupled to the micro-SQUIDs or nano-SQUIDs. Major challenges for this application are the development of SQUIDs (i) with ultralow flux noise, which can be achieved via the reduction of the inductance L of the SQUID loop and (ii) which can be operated in very large magnetic fields (up to the tesla range), without significant degradation of their noise performance.

The most common approach for the realization of direct-current (dc) nano-SQUIDs uses two constriction-type Josephson junctions (CJJs) intersecting the SQUID loop [11,12,14,16,23,26,27]. In this case, optimum coupling between a MNP and the nano-SQUID is achieved by placing the particle directly on top of one of the CJJs. The use of CJJs offers the possibility to operate the SQUIDs in strong magnetic fields. However, if conventional metallic superconductors such as Pb or Nb are used, high-field operation is limited by the upper critical field of typically 1 T for thin films [28]. Still, it has been demonstrated that by using ultrathin films, this limitation can be overcome [29]. However, with ultrathin films the SQUID inductance L is dominated by a large kinetic inductance contribution, which yields large flux noise. To date, the most successful approach is the SQUID on tip (SOT) [26]. With the so far smallest Pb SOT with 46-nm effective loop diameter and 15-nm film thickness, ultralow flux noise down to $50\ n\Phi_0/Hz^{1/2}$ at 4.2 K has been demonstrated [28] (Φ_0 is the magnetic flux quantum). The inductance for a slightly larger device (56-nm effective diameter) was estimated as $L = 5.8$ pH. The SOT technology is extremely powerful for high-resolution scanning SQUID microscopy and provides a spin sensitivity below $1\ \mu_B/Hz^{1/2}$ for certain intervals of applied magnetic field up to about 1 T (μ_B is the Bohr magneton) estimated for a pointlike MNP with 10 nm distance to the SOT. However, maintaining the optimum flux bias point in a variable

magnetic field is not possible; i.e., the flux noise and spin sensitivity strongly depend on the applied field, which makes such devices less interesting for the investigation of the magnetization reversal of MNPs.

An alternative approach is the use of $YBa_2Cu_3O_7$ (YBCO) dc nano-SQUIDs with grain-boundary Josephson junctions (GBJJs) for operation at temperature $T = 4.2$ K and below [30]. Magnetization reversal of a MNP can be detected by applying an in-plane magnetic field perpendicular to the grain boundary, i.e., without significant suppression of the GBJJ critical currents. The huge upper critical field of YBCO in the range of tens of teslas offers the possibility for operation in strong fields up to the tesla range, without using ultrathin films [31]. Hence, very low inductance devices with potentially ultralow flux noise can be realized.

Very recently, we performed an optimization study for the design of YBCO nano-SQUIDs [32]. This work is based on the calculation of the coupling factor ϕ_μ, i.e., the amount of magnetic flux coupled to the SQUID per magnetic moment of a pointlike MNP placed on top of a narrow constriction inserted into the SQUID loop. This additional constriction allows for the optimization of ϕ_μ (via constriction geometry) without affecting the junctions. In addition, we performed numerical simulations to calculate the SQUID inductance and root-mean-square (rms) spectral density of flux noise $S_{\Phi,w}^{1/2}$ in the thermal white-noise limit. This approach enabled us to predict the spin sensitivity in the thermal white-noise limit $S_{\mu,w}^{1/2} = S_{\Phi,w}^{1/2}/\phi_\mu$ for our devices as a function of all relevant device parameters. This optimization study predicts optimum performance for a YBCO film thickness $d \approx 120$ nm, which allows us to realize nano-SQUIDs with very small L of a few pH. For optimized devices, we predict $S_{\Phi,w}^{1/2}$ of several tens of $n\Phi_0/Hz^{1/2}$ and $\phi_\mu \sim 10$–$20\ n\Phi_0/\mu_B$ (for a MNP placed 10 nm above the YBCO film on top of the constriction) yielding a spin sensitivity $S_{\mu,w}^{1/2}$ of a few $\mu_B/Hz^{1/2}$.

Here, we report on the realization of optimized YBCO nano-SQUIDs based on GBJJs and on the experimental determination of their electric transport and noise properties in a magnetically shielded environment at $T = 4.2$ K. To demonstrate the suitability of our YBCO nano-SQUIDs for the detection of small spin systems, we present the measurement of the magnetization reversal (up to approximately 200 mT at $T = 4.2$ K) of an Fe nanowire with diameter $d_{Fe} = 39$ nm, which is positioned close the SQUID loop.

II. DEVICE FABRICATION AND EXPERIMENT SETUP

The fabrication of the devices is carried out according to Refs. [30,31]. A *c*-axis-oriented YBCO thin film of thickness d is grown epitaxially by pulsed laser deposition on a $SrTiO_3$ (STO) [001] bicrystal substrate with a 24° grain-boundary misorientation angle. An *in situ* evaporated Au layer of thickness d_{Au} serves as shunt resistance to provide nonhysteretic current-voltage characteristics (IVCs). SQUIDs with smallest line widths down to 50 nm are patterned by focused-ion-beam (FIB) milling with 30-keV Ga ions. The Au layer also minimizes Ga implantation into the YBCO film during FIB milling.

For characterization of the device properties, electric transport and noise measurements are performed in an electrically and magnetically shielded environment at $T = 4.2$ K, i.e., with the samples immersed into liquid He. By applying a modulation current I_{mod} across the constriction, the magnetic flux coupled to the SQUID can be modulated. This scheme allows flux biasing at the optimum working point and operation in a flux-locked loop (FLL) mode [33]. In FLL mode, a deviation from the voltage at the optimum working point (due to any flux signal), is amplified and then fed back via a feedback resistor as a feedback current through the constriction. The feedback current produces a feedback flux canceling the applied flux signal; i.e., the SQUID is always operated at its optimum working point, and the voltage across the feedback resistor (proportional to the flux signal) serves as the output signal. The readout in FLL mode is limited by the bandwidth of the feedback circuit. If the signals applied to the SQUID are small enough, one can also operate the SQUID in open-loop mode; i.e., the voltage across the SQUID is amplified without feedback, and the amplified voltage serves as the output signal. In this case, the readout is limited by the bandwidth of the voltage amplifier, which is typically larger than the FLL bandwidth. To determine the spectral density of flux noise S_Φ vs frequency f of the devices, we use a Magnicon SEL-1 SQUID electronics [34] in direct readout mode [35], which is either operated in open-loop mode (maximum bandwidth of approximately 7 MHz) or in FLL mode (maximum bandwidth of approximately 500–800 kHz). The SEL electronics allows for SQUID operation either with constant bias current (dc bias) or with a bias reversal readout scheme [maximum bias

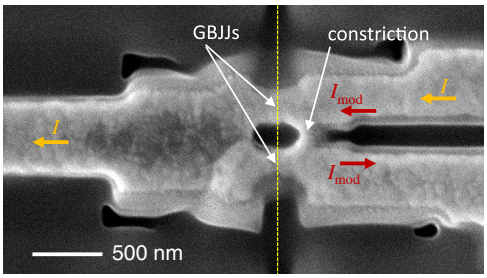

FIG. 1. SEM image of YBCO nano-SQUID-1. Vertical dashed line indicates position of the grain boundary intersecting the two SQUID arms. Horizontal arrows indicate paths for modulation current I_{mod} across the constriction and bias current I across the grain-boundary Josephson junctions.

TABLE I. Parameters of optimized SQUID-1 and -2 and of SQUID-3 used for measurements on Fe nanowire. Values for V_ϕ correspond to working points of noise measurements. Values in brackets for $S_{\Phi,w}^{1/2}$ and $S_{\mu,w}^{1/2}$ of SQUID-1 are based on the fitted noise spectrum. All devices have $d_{Au} = 70$ nm. SQUID-1 and -3 are measured at 4.2 K; SQUID-2 is measured at 5.3 K.

	d (nm)	l_c (nm)	l_J (nm)	w_c (nm)	w_{J1} (nm)	w_{J2} (nm)	β_L	L (pH)	I_c (μA)	R_N (Ω)	I_cR_N (mV)	V_Φ (mV/Φ_0)	$S_{\Phi,w}^{1/2}$ (nΦ_0/Hz$^{1/2}$)	ϕ_μ (nΦ_0/μ_B)	$S_{\mu,w}^{1/2}$ (μ_B/Hz$^{1/2}$)
SQUID-1	120	190	350	85	210	160	1.8	3.9	960	2.0	1.92	4.4	<50 (45)	13	<3.7 (3.4)
SQUID-2	120	230	370	100	180	230	0.94	6.3	311	2.5	0.78	1.7	<83	12	<6.7
SQUID-3	75	190	340	100	270	340	0.95	28	69	2.3	0.16	0.65	<1450	15	<98

reversal (BR) frequency $f_{BR} = 260$ kHz], to reduce $1/f$ noise caused by fluctuations of the critical currents $I_{0,1}$ and $I_{0,2}$ of the Josephson junctions 1 and 2, respectively [33].

Below we present the data of our best device, SQUID-1, with a $d = 120$-nm-thick YBCO film. Figure 1 shows a scanning electron microscope (SEM) image of SQUID-1. The loop size 350×190 nm^2 is given by the length l_J of the bridges straddling the grain boundary and by the length l_c of the constriction. SQUID-1 has junction widths $w_{J1} = 210$ nm and $w_{J2} = 160$ nm and a constriction width $w_c = 85$ nm. The parameters for SQUID-1 are summarized in Table I. For comparison, we also include parameters for a similar device, SQUID-2, which has the same YBCO film thickness, however, slightly larger inductance $L = 6.3$ pH, and about a factor of 2.5 smaller characteristic voltage $V_c \equiv I_cR_N$. I_c is the maximum critical current, and R_N is the asymptotic normal-state resistance of the SQUID. Details on electric transport and noise characteristics of SQUID-2 are presented in Sec. I of the Supplemental Material [36]. Those also include noise data taken from 6 to 65 K in a different setup with a temperature stability of approximately 1 mK [37]. Table I also includes parameters for SQUID-3, which is used for measurements on an Fe nanowire in a high-field setup, as discussed further below.

III. SQUID-1: ELECTRIC TRANSPORT AND NOISE

A. SQUID-1: Dc characteristics

Figure 2 shows the dc characteristics of SQUID-1. Figure 2(a) shows IVCs for $I_{mod} = 0$ and two values of I_{mod} corresponding to the maximum and minimum critical current. The IVCs are slightly hysteretic with maximum critical current $I_c = 960$ μA and $R_N = 2.0$ Ω, which yields $V_c = 1.92$ mV. The inset of Fig. 2(a) shows the modulation of the critical current $I_c(I_{mod})$. From the modulation period, we find for the magnetic flux Φ coupled to the SQUID by I_{mod} the mutual inductance $M = \Phi/I_{mod} = 0.44\Phi_0/\text{mA} = 0.91$ pH. We perform numerical simulations based on the resistively and capacitively shunted junction model to solve the coupled Langevin equations which include thermal fluctuations of the junction resistances [38]. From simulations of the $I_c(I_{mod})$ characteristics [cf. inset of Fig. 2(a)], we obtain for the screening parameter $\beta_L = 2I_0L/\Phi_0 = 1.8$ [with $I_0 = (I_{0,1} + I_{0,2})/2$], which yields a SQUID inductance $L = 3.9$ pH. We do find good agreement between the measured and simulated $I_c(I_{mod})$ characteristics if we include an inductance asymmetry $\alpha_L \equiv (L_2 - L_1)/(L_2 + L_1) = 0.20$ (L_1 and L_2

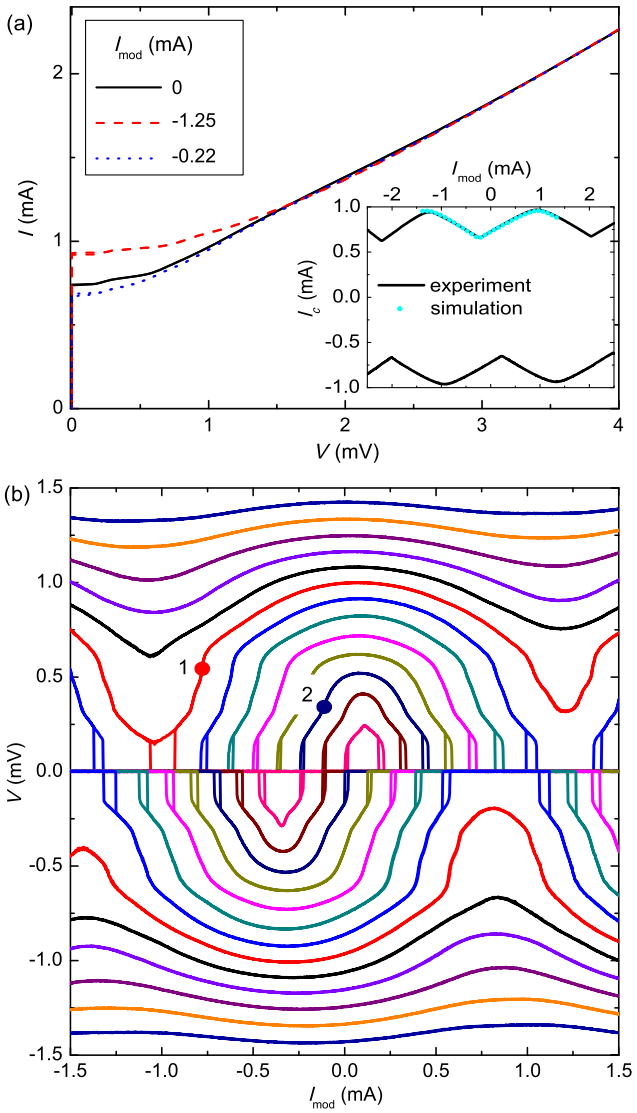

FIG. 2. SQUID-1 dc transport characteristics. (a) Measured IVCs for three different values of I_{mod}, including flux bias (I_{mod}) values which yield maximum and minimum critical current. Inset: Measured $I_c(I_{mod})$ for positive and negative current bias (solid lines) and numerical simulations (dots). (b) Measured $V(I_{mod})$ for bias currents $|I| = 0.64$–1.12 mA (in 40-μA steps). Points 1 and 2 are bias points with $V_\Phi = 12$ and 4.5 mV/Φ_0, respectively.

are the inductances of the two SQUID arms) and a critical current asymmetry $\alpha_I \equiv (I_{0,2} - I_{0,1})/(I_{0,2} + I_{0,1}) = 0.27$. These asymmetries are caused by asymmetric biasing of the SQUID and by asymmetries of the device itself.

$V(I_{\mathrm{mod}})$ is plotted in Fig. 2(b) for different bias currents. The transfer function, i.e., the maximum value of $\partial V/\partial\Phi$, in the nonhysteretic regime is $V_\Phi \approx 12$ mV/Φ_0 [at $I = 0.92$ mA; cf. point 1 in Fig. 2(b)].

B. SQUID-1: Noise data

1. Open-loop mode

Figure 3(a) shows the rms spectral density of flux noise $S_\Phi^{1/2}(f)$ of SQUID-1 measured in open-loop mode to reach the highest possible bandwidth of the readout electronics. Because of the limitation in the maximum bias current of the readout electronics, noise spectra are taken at $I = 0.72$ mA with a transfer function $V_\Phi = 4.5$ mV/Φ_0 [cf. point 2 in Fig. 2(b)]. Up to the cutoff frequency $f_{3\,\mathrm{dB}} = 7$ MHz, there is no white flux noise observable. Instead, the flux noise scales roughly as $S_\Phi \propto 1/f$, with $S_\Phi^{1/2} \approx 10\ \mu\Phi_0/\mathrm{Hz}^{1/2}$ at $f = 100$ Hz and $1\ \mu\Phi_0/\mathrm{Hz}^{1/2}$ at 10 kHz. This level of low-frequency excess noise is quite typical for YBCO GBJJ SQUIDs (also at $T = 77$ K) and has been ascribed to critical current fluctuations in the GBJJs [39]. However, due to the limitation by thermal white noise, typically between 1 and 10 $\mu\Phi_0/\mathrm{Hz}^{1/2}$ for low-noise YBCO SQUIDs, this f-dependent excess noise has not been observed so far up to the megahertz range. We note that for YBCO nano-SQUIDs implementing CJJs [27], a frequency-dependent $(1/f)$-like excess noise at $T = 8$ K of almost the same level as that for SQUID-1 was reported very recently and was also attributed to critical current fluctuations. For frequencies above 10 kHz, the flux noise of the YBCO nano-SQUID in Ref. [27] was limited by amplifier background noise.

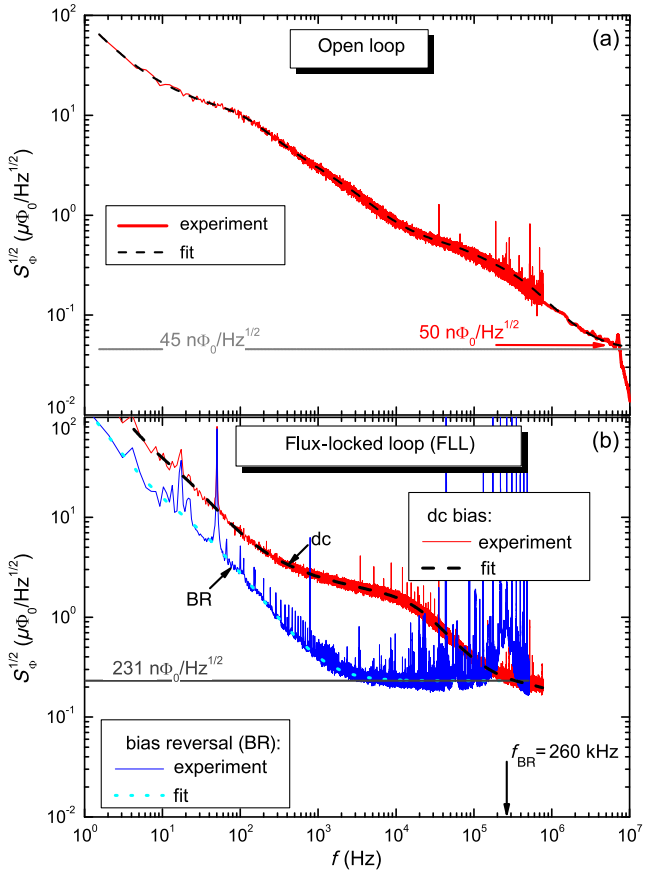

FIG. 3. Rms flux noise of SQUID-1. (a) Measured in open-loop mode at bias point 2 ($I = 0.72$ mA) in Fig. 2(b). Dashed line is a fit to the measured spectrum with white noise as indicated by the horizontal line. (b) Measured in FLL mode with dc bias and bias reversal ($|I| = 0.43$ mA, $V_\Phi = 4.4$ mV/Φ_0). Vertical arrow indicates bias reversal frequency f_{BR}. Dashed and dotted lines are fits to the spectra; horizontal lines indicate fitted white noise.

For a more detailed analysis of the measured flux noise $S_\Phi(f)$, we apply an algorithm [40] to decompose the noise spectra into a sum of Lorentzians $F_i(f) = F_{0,i}/[1 + (f/f_{c,i})^2]$ plus a white-noise contribution F_w. The noise spectrum measured for SQUID-1 in open loop can be very well fitted by $F_{\mathrm{op}}(f) = F_{w,\mathrm{op}} + F_{s,\mathrm{op}} + \sum_{i=1}^{16} F_{\mathrm{op},i}(f)$, i.e., the superposition of a white-noise contribution with $F_{w,\mathrm{op}}^{1/2} = 45\ \mathrm{n}\Phi_0/\mathrm{Hz}^{1/2}$ plus a $1/f^2$ spectrum $F_{s,\mathrm{op}}$ (i.e., one or more Lorentzians with characteristic frequencies f_c well below 1 Hz) with $F_{s,\mathrm{op}}^{1/2}(1\ \mathrm{Hz}) = 84\ \mu\Phi_0/\mathrm{Hz}^{1/2}$ plus 16 Lorentzians, with $f_{c,i}$ ranging from 2.6 Hz to 2.6 MHz. For more details, see Sec. III of the Supplemental Material [36]. Hence, the decomposition of the spectrum into Lorentzians yields an estimate of the white rms flux noise $S_{\Phi,w}^{1/2} \approx 45\ \mathrm{n}\Phi_0/\mathrm{Hz}^{1/2}$ for SQUID-1. We note that this value for $S_{\Phi,w}^{1/2}$ is only a factor of 1.8 above the value, which we obtain from numerical simulations of the coupled Langevin equations [38] at $T = 4.2$ K for the parameters of SQUID-1.

Taking the measured flux noise at 7 MHz as an upper limit for $S_{\Phi,w}^{1/2}$, we still obtain a very low white rms flux noise, i.e., $S_{\Phi,w}^{1/2} < 50\ \mathrm{n}\Phi_0/\mathrm{Hz}^{1/2}$. This more conservative estimate for the white rms flux noise level is an improvement by more than an order of magnitude compared to our nonoptimized devices operated at 4.2 K and compared to the lowest value reported so far for a YBCO SQUID (at 8 K) very recently [27]. Furthermore, this value is the same as the lowest value reported for a Pb SOT operated at 4.2 K [28] and among the lowest flux noise levels ever achieved for a SQUID [9,41,42].

For the geometry of SQUID-1, we calculate [32] a coupling factor $\phi_\mu = 13.4\ \mathrm{n}\Phi_0/\mu_{\mathrm{B}}$ (10 nm above the YBCO film). With $S_{\Phi,w}^{1/2} < 50\ \mathrm{n}\Phi_0/\mathrm{Hz}^{1/2}$, we can determine an upper limit for the spin sensitivity (white-noise limit) of $S_{\mu,w}^{1/2} < 3.7\ \mu_B/\mathrm{Hz}^{1/2}$. If we take the fitted white

flux noise of 45 $n\Phi_0/Hz^{1/2}$, we obtain $S_{\mu,w}^{1/2} = 3.4\,\mu_B/Hz^{1/2}$. Hence, the achieved performance matches very well the predictions of our recent optimization study [32].

2. FLL mode: Dc bias vs bias reversal

Although the achieved low level of white flux noise for SQUID-1 is encouraging, one certainly will like to extend such a low-noise performance down to much lower frequencies. Therefore, we also perform noise measurements in FLL mode (with approximately 700-kHz bandwidth) and compare measurements with dc bias and bias reversal (with $f_{BR} = 260$ kHz). We note that the measurements in FLL mode are performed within a different cooling cycle, after SQUID-1 already shows a slight degradation in I_c [43]. Still, we are able to find a working point (at $|I| = 0.43$ mA) which yields almost the same transfer function, 4.4 mV/Φ_0, as for the measurement before degradation in open-loop mode.

Figure 3(b) shows rms flux noise spectra taken with dc bias and bias reversal. Comparing first the FLL dc bias measurement with the open-loop data, we note that the noise levels at f_{BR} coincide. For $f < f_{BR}$, the noise levels of the open-loop and FLL dc bias data are similar; however, the shape of the spectra differ, which we attribute to the above-mentioned degradation and variations between different cooling cycles. The dashed line in Fig. 3(b) is a fit to the measured spectral density of flux noise by $F_{dc}(f) = F_{w,dc} + \sum_{i=1}^{15} F_{dc,i}(f)$, i.e., the superposition of 15 Lorentzians, with $f_{c,i}$ ranging from 0.8 Hz to 6.8 MHz, plus a white-noise contribution $F_{w,dc}^{1/2} = 41$ $n\Phi_0/Hz^{1/2}$, which we fix to a value similar to the white-noise level determined for the open-loop measurement. For more details, see Sec. III of the Supplemental Material [36].

Applying bias reversal, one expects a suppression of the contributions due to in-phase and out-of-phase critical current fluctuations of the GBJJs [39]. If the f-dependent excess noise below f_{BR} arises solely from I_0 fluctuations, one expects in bias reversal mode a frequency-independent noise for frequencies below the peak at f_{BR}, at a level which is given by the noise measured at f_{BR} in dc bias mode. This behavior can be observed for frequencies down to a few kilohertz, with an f-independent noise $F_{w,BR}^{1/2} = 231$ $n\Phi_0/Hz^{1/2}$. For lower frequencies, however, we still find a strong f-dependent excess noise in bias reversal mode, which, hence cannot be attributed to I_0 fluctuations.

The spectral density of flux noise measured in bias reversal mode can be well approximated [cf. dotted line in Fig. 3(b)] by $F_{BR}(f) = F_{w,BR} + F_{s,BR} + \sum_{i=1}^{6} F_{BR,i}(f)$, with $F_{s,BR}^{1/2}(1\text{ Hz}) = 128$ $\mu\Phi_0/Hz^{1/2}$ and $f_{c,i}$ of the six Lorentzians ranging from 21 Hz to 5 kHz. For more details, see Sec. III of the Supplemental Material [36].

Obviously, below a few kilohertz, the low-frequency excess noise is dominated by slow fluctuators, which cannot be attributed to I_0 fluctuations. For different working points (I and I_{mod}) and also for other devices, the observation of low-f excess noise in bias reversal mode is reproducible [cf. flux noise data of SQUID-2 (from $T = 6$ K up to 65 K) and of SQUID-3 (at $T = 4.2$ K) in Secs. I and II, respectively, of the Supplemental Material [36]].

Considering the narrow linewidths of the SQUID structures, we estimate a threshold field for trapping of Abrikosov vortices [44] to be well above 1 mT. Since the measurements are performed in a magnetically shielded environment well below 100 nT, the presence of Abrikosov vortices as the source of the observed low-f fluctuators is very unlikely.

Low-frequency excess noise, which neither arises from I_0 nor from vortex fluctuations, has been reported during the last decades for SQUIDs based on conventional superconductors like Nb, Pb, PbIn, and Al, in particular, at temperatures well below 1 K [45]. This issue has recently been revived due to the increasing interest in the development of flux qubits and SQUIDs for ultra-low-temperature applications [46]. Various models have been suggested to describe the origin of such low-f excess noise, e.g., based on the coupling of magnetic moments associated with trapped electrons [47] or surface states [48,49], although the microscopic nature of defects as sources of excess "spin noise" still remains unclear.

For YBCO SQUIDs, excess low-f spin noise has not been addressed so far. However, it seems quite likely that defects are also a source of magnetic fluctuators in SQUIDs based on cuprates or any other oxide superconductors. Such defects can be present either in the thin-film SQUID structures themselves or in the substrates onto which the thin films are grown or at the interface between the thin film and the substrate.

The emergence and modification of magnetism at interfaces and surfaces of oxides, which are diamagnetic in the bulk, is currently an intensive field of research [50–52]. For STO, oxygen-vacancy-induced magnetism has been predicted [53], and experimental studies suggest ferromagnetic ordering up to room temperature [54], e.g., for defects induced by ion irradiation of single crystalline STO [55]. Furthermore, defect-induced magnetism in oxide grain boundaries and related defects have been suggested to be the intrinsic origin of ferromagnetism in oxides [56].

Obviously, further investigations on the impact and nature of such defects in our devices are needed and will be the subject of further studies. Such studies will include detailed noise measurements (dc vs bias reversal, variable flux bias, temperature, and magnetic field) to characterize and understand the f-dependent noise sources and, hopefully, eliminate them. Furthermore, readout with bias reversal at higher frequency up to the megahertz range in FLL mode has to be implemented in order to maintain the achieved ultralow white flux noise level down to lower frequencies. And finally, for applications of our nano-SQUIDs, it will be important to avoid

degradation in time, which shall be achieved by adding a suitable passivation layer, however, without introducing f-dependent excess noise.

IV. SQUID-3: MAGNETIZATION REVERSAL OF FE NANOWIRE

As a proof of principle, we demonstrate nano-SQUID measurements on the magnetization reversal of an Fe nanowire which is encapsulated in a carbon nanotube (CNT) [57]. Such iron-filled CNTs (Fe CNTs) are of fundamental interest with respect to studies on nanomagnetism. Furthermore, they are attractive for various applications, e.g., as tips in magnetic-force microscopy [58,59]. The Fe nanowire, which contains mainly single crystalline (ferromagnetic) α-Fe, has a diameter $d_{\mathrm{Fe}} = 39$ nm and length $l_{\mathrm{Fe}} = 13.8$ μm. The CNT has a diameter of approximately 130 nm. We note that this section is not directly related to the previous section in a sense to demonstrate the ultimate sensitivity of our devices on a magnetic nanoparticle with the smallest yet still detectable signals and operation in the strongest possible magnetic fields. Rather, we want to show an example of the feasibility of using our YBCO nano-SQUIDs for practical applications. As shown within this section, we can demonstrate signal-to-noise ratios which are clearly superior to micro-Hall measurements on similar nanowires.

The Fe CNT is positioned by a Kleindiek three-axis manipulator inside a FIB SEM combination onto SQUID-3, such that the distance between the left end of the Fe nanowire and the SQUID loop is approximately 300 nm (cf. Fig. 4). We note that for optimum coupling of the stray field of the Fe nanowire into the SQUID, it is preferable to place the end of the Fe nanowire close to the edge of the SQUID loop opposite the constriction. At this location, the coupling factor is slightly smaller than directly on top of the constriction; however, it does not fall off very rapidly upon moving farther away from the loop, as it is the case near the constriction [31]. The Fe nanowire axis (its easy axis) is aligned as close as possible with the substrate plane (x-y plane), with an inclination angle $\theta \approx 4°$ and perpendicular to the grain boundary, which is oriented along the y axis. The inclination of the Fe wire axis with respect to the x axis is $<1°$. The vertical distance (along the z axis) between the nanowire axis (at its left end) and the surface of the YBCO film is approximately 300 nm.

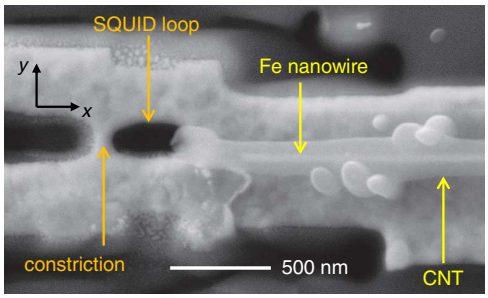

FIG. 4. SEM image of SQUID-3 with an Fe-wire-filled carbon nanotube positioned close to the SQUID loop.

The measurements on the Fe nanowire are performed with the nonoptimized SQUID-3. This device has a significantly larger inductance (due to its smaller film thickness) and much smaller characteristic voltage, resulting in a much smaller transfer function $V_\Phi = 0.65$ mV/Φ_0, as compared to SQUID-1 and -2. Magnetization-reversal measurements on the Fe CNT are performed with SQUID-3 operated in FLL dc bias mode up to $f = 190$ kHz. At this frequency, the noise is limited by the readout electronics, which yields for SQUID-3 an upper limit of the white rms flux noise $S_{\Phi,w}^{1/2} \leq 1.45\ \mu\Phi_0/\mathrm{Hz}^{1/2}$. Below approximately 40 kHz, SQUID-3 shows f-dependent excess noise with $S_\Phi^{1/2} \approx 8\ \mu\Phi_0/\mathrm{Hz}^{1/2}$ at $f = 100$ Hz and $S_\Phi^{1/2} \approx 20\ \mu\Phi_0/\mathrm{Hz}^{1/2}$ at $f = 10$ Hz, with an approximately $1/f^2$ increase of S_Φ below 10 Hz. Some experimentally determined parameters of SQUID-3 are listed in Table I. Details on low-field electric transport and noise characteristics of SQUID-3 are presented in Sec. II of the Supplemental Material [36].

For magnetization-reversal measurements of the Fe nanowire on top of SQUID-3, the sample is mounted in a high-field setup, which allows us to apply magnetic fields up to $\mu_0 H = 7$ T [31]. To minimize coupling of the external magnetic field H into the SQUID, the SQUID loop (in the x-y plane) is aligned parallel to the field. To minimize coupling of the external field into the GBJJs, the grain boundary (along the y axis) is aligned perpendicular to the applied field. The alignment of the SQUID with respect to the applied field direction is performed by an Attocube system including two goniometers with perpendicular tilt axes and one rotator. In this configuration, the external field H is applied along the x axis (cf. Fig. 4), and the angle between H and the Fe nanowire axis is given by θ.

Figure 5 shows the flux signal $\Phi(H)$ detected by SQUID-3, while sweeping H, at a rate $\mu_0 \partial H/\partial t \approx 1$ mT/s. At the fields $\pm\mu_0 H_n = \pm 101$ mT, abrupt changes by $\Delta\Phi \approx 150$ mΦ_0 clearly indicate magnetization reversal of the Fe nanowire. The shape of the $\Phi(H)$ curve indicates magnetization reversal of a single-domain particle. The slope of the curve in the interval $-H_n \leq H \leq H_n$ depends strongly on the alignment of the SQUID with respect to the applied field. Hence, this slope can be attributed, at least partially, to the coupling of the external field to the SQUID loop. The hysteresis in the signals for $|H| \gtrsim 100$ mT is typically observed also for our SQUIDs measured in the high-field setup without MNPs coupled to them. Hence, this hysteresis is attributed to a spurious magnetization signal from our setup or from the above-mentioned magnetic defects close to the nano-SQUID, rather than being generated by the nanowire.

In order to convert from magnetic flux detected by the SQUID to magnetization of the Fe nanowire, we follow the

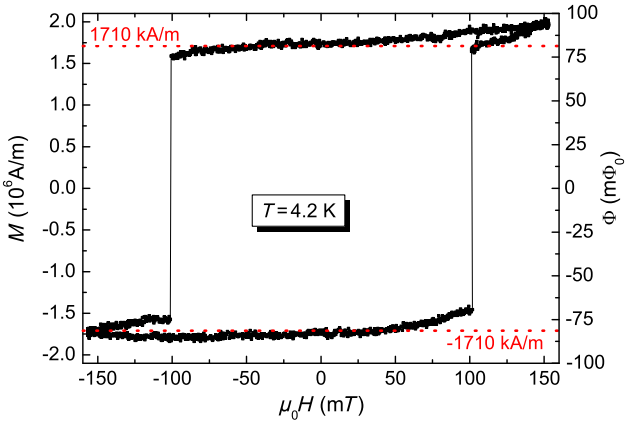

FIG. 5. Hysteresis loop $\Phi(H)$ of the Fe nanowire detected with SQUID-3 (operated in FLL dc bias mode with cutoff frequency approximately 190 kHz, at optimum working point with $V_\Phi = 0.65\ \mathrm{mV}/\Phi_0$). Switching of the magnetization occurs at $\pm\mu_0 H_n = \pm 101$ mT. The residual field $\mu_0 H_{\mathrm{res}} = 4.0$ mT is subtracted. Left axis indicates corresponding magnetization $M = \Phi/\phi_M$; the dashed lines indicate the literature's value of the saturation magnetization $\pm M_s$.

approach described in Ref. [60]. We numerically calculate the coupling factor $\phi_\mu(\hat{e}_\mu, \vec{r}_p)$ for a pointlike MNP with orientation $\hat{e}_\mu$ of its magnetic moment at position $\vec{r}_p$ in the 3D space above the SQUID [32]. These simulations take explicitly into account the geometry of SQUID-3 and are based on London theory [61]. We then assume that the Fe nanowire is in its fully saturated state, with saturation magnetization M_s, with all moments oriented along the wire axis. The corresponding saturation flux coupled to the SQUID is denoted as Φ_s. The ratio Φ_s/M_s is obtained by integration of the coupling factor ϕ_μ over the volume V_{Fe} of the Fe wire, at its given position, determined from SEM images. This integration yields

$$\phi_M \equiv \frac{\Phi_s}{M_s} = \int_{V_{\mathrm{Fe}}} \phi_\mu(\vec{r}_p)dV = 47.6\,\frac{\mathrm{n}\Phi_0}{\mathrm{Am}^{-1}}. \qquad (1)$$

From this result, we calculate $\Phi_s = M_s\phi_M = 81.4\ \mathrm{m}\Phi_0$, with $M_s = 1710$ kA/m taken from the literature [62]. The comparison with the measured flux signals $\pm 82.5\ \mathrm{m}\Phi_0$ at $H = 0$ shows very good agreement. The left axis in Fig. 5 shows the magnetization axis scaled as $M = \Phi/\phi_M$ with the horizontal dotted lines indicating the literature's value $M_s = \pm 1710$ kA/m. Hence, the measured flux signals are also in quantitative agreement with the assumption that the Fe nanowire switches to a fully saturated single-domain state.

In Ref. [58], it was shown for a similar Fe CNT that the nucleation field H_n changes with θ in a way which is typical for nucleation of magnetization reversal via the curling mode [63] in ferromagnetic nanowires as opposed to uniform rotation of the magnetic moments in small enough MNPs as described by the Stoner-Wolfarth model [64]. For switching via curling mode, one obtains for $\theta = 0$ the simple relation $H_n = M_s a/2$, with a negligible increase well below 1% with $\theta = 4°$ [65]. Here, $a = 1.08(2\lambda_{\mathrm{ex}}/d_{\mathrm{Fe}})^2$, with the exchange length $\lambda_{\mathrm{ex}} = \sqrt{4\pi A/(\mu_0 M_s^2)}$ and the exchange constant A [62]. For $d_{\mathrm{Fe}} = 39$ nm and with $\lambda_{\mathrm{ex}} = 5.8$ nm [62], we obtain $a = 0.0955$, and with $M_s = 1710$ kA/m, we obtain an estimate of the nucleation field $H_n = 103$ mT, which is in very good agreement with the experimentally observed value.

Finally, we note that the SQUID measurement yields a noise amplitude of approximately 1 $\mathrm{m}\Phi_0$, which is 2 orders of magnitude smaller than the detected signal upon magnetization reversal. For comparison, measurements on a similar Fe nanowire by micro-Hall magnetometry yield a noise amplitude which was about 1 order of magnitude below the switching signal [58]. Hence, the use of our nano-SQUID improves the signal-to-noise ratio by about 1 order of magnitude.

V. CONCLUSIONS

In conclusion, we fabricate and investigate optimized YBCO nano-SQUIDs based on grain-boundary Josephson junctions. For our best device, an upper limit for the white flux noise level $S_\Phi^{1/2} < 50\ \mathrm{n}\Phi_0/\mathrm{Hz}^{1/2}$ in magnetically shielded environment can be determined, which corresponds to a spin sensitivity $S_\mu^{1/2} \equiv S_\Phi^{1/2}/\phi_\mu = 3.7\ \mu_B/\mathrm{Hz}^{1/2}$ for a magnetic nanoparticle located 10 nm above the constriction in the SQUID loop. Here, the coupling factor ϕ_μ is determined by numerical simulations based on London theory, which takes the device geometry into account. An obvious drawback of YBCO grain-boundary junction nano-SQUIDs is the frequency-dependent excess noise, which extends up to the megahertz range for optimized devices with ultralow flux noise in the white-noise limit. To eliminate $1/f$ noise, a bias reversal scheme is applied, which reduces only the frequency-dependent excess noise partially. Hence, in addition to critical current fluctuations, spin noise which is possibly due to fluctuations of defect-induced magnetic moments in the $SrTiO_3$ substrate is a major issue, which has to be studied in more detail for further improvement of the nano-SQUID performance at low frequencies. Nevertheless, we demonstrate the suitability of the YBCO nano-SQUIDs as detectors for magnetic nanoparticles in moderate magnetic fields by measuring the magnetization reversal of an iron nanowire that is placed close to the SQUID loop. Switching of the magnetization is detected at $\mu_0 H \approx \pm 100$ mT, which is in very good agreement with nucleation of magnetization reversal via curling mode.

ACKNOWLEDGMENTS

T. S. acknowledges support by the Carl-Zeiss-Stiftung. M. J. M.-P. acknowledges support by the Alexander von

Humboldt Foundation. We gratefully acknowledge fruitful discussions with D. Drung (Physikalisch-Technische Bundesanstalt Berlin) and technical support by M. Turad and R. Löffler [instrument scientists of the core facility Center for Light-Matter Interaction, Sensors & Analytics (LISA$^+$)]. This work is supported by the Nachwuchswissenschaftlerprogramm of the Universität Tübingen, by the Deutsche Forschungsgemeinschaft (DFG) via Projects No. KO 1303/13-1, No. MU 1794/3-2, and No. SFB/TRR 21 C2 and by the EU-FP6-COST Action MP1201.

[1] *Molecular Magnets: Physics and Applications*, edited by Juan Bartolomé, Fernando Luis, and Julio F. Fernández (Springer, Heidelberg, 2014).

[2] Lapo Bogani and Wolfgang Wernsdorfer, Molecular spintronics using single-molecule magnets, Nat. Mater. **7**, 179 (2008).

[3] Michael N. Leuenberger and Daniel Loss, Quantum computing in molecular magnets, Nature (London) **410**, 789 (2001).

[4] S. Odenbach, Ferrofluids and their applications, MRS Bull. **38**, 921 (2013).

[5] Andreas Jordan, Regina Scholz, Peter Wust, Horst Fähling, and Roland Felix, Magnetic fluid hyperthermia (MFH): Cancer treatment with AC magnetic field induced excitation of biocompatible superparamagnetic nanoparticles, J. Magn. Magn. Mater. **201**, 413 (1999).

[6] R. C. Semelka and T. K. G. Helmberger, State of the art: Contrast agents for MR imaging of the liver, Radiology **218**, 27 (2001).

[7] R. Klingeler, S. Hampel, and B. Büchner, Carbon nanotube based biomedical agents for heating, temperature sensoring and drug delivery, International Journal of Hyperthermia **24**, 496 (2008).

[8] W. Wernsdorfer, Classical and quantum magnetization reversal studied in nanometersized particles and clusters, Adv. Chem. Phys. **118**, 99 (2001).

[9] D. D. Awschalom, J. R. Rozen, M. B. Ketchen, W. J. Gallagher, A. W. Kleinsasser, R. L. Sandstrom, and B. Bumble, Low-noise modular microsusceptometer using nearly quantum limited dc SQUIDs, Appl. Phys. Lett. **53**, 2108 (1988).

[10] M. Ketchen, D. Awschalom, W. Gallagher, A. Kleinsasser, R. Sandstrom, J. Rozen, and B. Bumble, Design, fabrication, and performance of integrated miniature SQUID susceptometers, IEEE Trans. Magn. **25**, 1212 (1989).

[11] K. Hasselbach, D. Mailly, and J. R. Kirtley, Micro-superconducting quantum interference device characteristic, J. Appl. Phys. **91**, 4432 (2002).

[12] S. K. H. Lam and D. L. Tilbrook, Development of a niobium nanosuperconducting quantum interference device for the detection of small spin populations, Appl. Phys. Lett. **82**, 1078 (2003).

[13] J.-P. Cleuziou, W. Wernsdorfer, V. Bouchiat, T. Ondarçuhu, and M. Monthioux, Carbon nanotube superconducting quantum interference device, Nat. Nanotechnol. **1**, 53 (2006).

[14] Aico G. P. Troeman, Hendrie Derking, Bert Borger, Johannes Pleikies, Dick Veldhuis, and Hans Hilgenkamp, NanoSQUIDs based on niobium constrictions, Nano Lett. **7**, 2152 (2007).

[15] Nicholas C. Koshnick, Martin E. Huber, Julie A. Bert, Clifford W. Hicks, Jeff Large, Hal Edwards, and Kathryn A. Moler, A terraced scanning super conducting quantum interference device susceptometer with submicron pickup loops, Appl. Phys. Lett. **93**, 243101 (2008).

[16] L. Hao, J. C. Macfarlane, J. C. Gallop, D. Cox, J. Beyer, D. Drung, and T. Schurig, Measurement and noise performance of nano-superconducting-quantum-interference devices fabricated by focused ion beam, Appl. Phys. Lett. **92**, 192507 (2008).

[17] C. P. Foley and H. Hilgenkamp, Why NanoSQUIDs are important: An introduction to the focus issue, Supercond. Sci. Technol. **22**, 064001 (2009).

[18] V. Bouchiat, Detection of magnetic moments using a nano-squid: Limits of resolution and sensitivity in near-field squid magnetometry, Supercond. Sci. Technol. **22**, 064002 (2009).

[19] W. Wernsdorfer, From micro- to nano-SQUIDs: Applications to nanomagnetism, Supercond. Sci. Technol. **22**, 064013 (2009).

[20] Francesco Giazotto, Joonas T. Peltonen, Matthias Meschke, and Jukka P. Pekola, Superconducting quantum interference proximity transistor, Nat. Phys. **6**, 254 (2010).

[21] M. J. Martínez-Pérez, E. Bellido, R. de Miguel, J. Sesé, A. Lostao, C. Gómez-Moreno, D. Drung, T. Schurig, D. Ruiz-Molina, and F. Luis, Alternating current magnetic susceptibility of a molecular magnet submonolayer directly patterned onto a micro superconducting quantum interference device, Appl. Phys. Lett. **99**, 032504 (2011).

[22] E. J. Romans, S. Rozhko, L. Young, A. Blois, L. Hao, D. Cox, and J. C. Gallop, Noise performance of niobium nano-SQUIDs in applied magnetic fields, IEEE Trans. Appl. Supercond. **21**, 404 (2011).

[23] R. Russo, C. Granata, E. Esposito, D. Peddis, C. Cannas, and A. Vettoliere, Nanoparticle magnetization measurements by a high sensitive nano-superconducting quantum interference device, Appl. Phys. Lett. **101**, 122601 (2012).

[24] Carmine Granata, Antonio Vettoliere, Roberto Russo, Matteo Fretto, Natascia De Leo, and Vincenzo Lacquaniti, Three-dimensional spin nanosensor based on reliable tunnel Josephson nano-junctions for nanomagnetism investigations, Appl. Phys. Lett. **103**, 102602 (2013).

[25] D. Drung, J.-H. Storm, F. Ruede, A. Kirste, M. Regin, T. Schurig, A. M. Repollés, J. Sesé, and F. Luis, Thin-film microsusceptometer with integrated nanoloop, IEEE Trans. Appl. Supercond. **24**, 1600206 (2014).

[26] Amit Finkler, Yehonathan Segev, Yuri Myasoedov, Michael L. Rappaport, Lior Ne'eman, Denis Vasyukov, Eli Zeldov, Martin E. Huber, Jens Martin, and Amir Yacoby, Self-aligned nanoscale SQUID on a tip, Nano Lett. **10**, 1046 (2010).

[27] R. Arpaia, M. Arzeo, S. Nawaz, S. Charpentier, F. Lombardi, and T. Bauch, Ultra low noise $YBa_2Cu_3O_{7-\delta}$

nano superconducting quantum interference devices implementing nanowires, Appl. Phys. Lett. **104**, 072603 (2014).
[28] Denis Vasyukov, Yonathan Anahory, Lior Embon, Dorri Halbertal, Jo Cuppens, Lior Ne'eman, Amit Finkler, Yehonathan Segev, Yuri Myasoedov, Michael L. Rappaport, Martin E. Huber, and Eli Zeldov, A scanning superconducting quantum interference device with single electron spin sensitivity, Nat. Nanotechnol. **8**, 639 (2013).
[29] Lei Chen, Wolfgang Wernsdorfer, Christos Lampropoulos, George Christou, and Irinel Chiorescu, On-chip SQUID measurements in the presence of high magnetic fields, Nanotechnology **21**, 405504 (2010).
[30] J. Nagel, K. B. Konovalenko, M. Kemmler, M. Turad, R. Werner, E. Kleisz, S. Menzel, R. Klingeler, B. Büchner, R. Kleiner, and D. Koelle, Resistively shunted $YBa_2Cu_3O_7$ grain boundary junctions and low-noise SQUIDs patterned by a focused ion beam down to 80 nm linewidth, Supercond. Sci. Technol. **24**, 015015 (2011).
[31] T. Schwarz, J. Nagel, R. Wölbing, M. Kemmler, R. Kleiner, and D. Koelle, Low-noise nano superconducting quantum interference device operating in tesla magnetic fields, ACS Nano **7**, 844 (2013).
[32] R. Wölbing, T. Schwarz, B. Müller, J. Nagel, M. Kemmler, R. Kleiner, and D. Koelle, Optimizing the spin sensitivity of grain boundary junction nanoSQUIDs–Towards detection of small spin systems with single-spin resolution, Supercond. Sci. Technol. **27**, 125007 (2014).
[33] D. Drung and M. Mück, in *The SQUID Handbook*, edited by John Clarke and Alex I. Braginski, Fundamentals and Technology of SQUIDs and SQUID Systems Vol. 1 (Wiley-VCH, Weinheim, 2004), Chap. 4, pp. 127–170.
[34] SQUID electronics SEL-1, http://www.magnicon.com.
[35] D. Drung, High-t_c and low-t_c dc SQUID electronics, Supercond. Sci. Technol. **16**, 1320 (2003).
[36] See the Supplemental Material at http://link.aps.org/supplemental/10.1103/PhysRevApplied.3.044011 for additional data and analysis of SQUID-1, -2 and -3.
[37] M. Kemmler, D. Bothner, K. Ilin, M. Siegel, R. Kleiner, and D. Koelle, Suppression of dissipation in Nb thin films with triangular antidot arrays by random removal of pinning sites, Phys. Rev. B **79**, 184509 (2009).
[38] B. Chesca, R. Kleiner, and D. Koelle, in *The SQUID Handbook*, edited by John Clarke and Alex I. Braginski, Fundamentals and Technology of SQUIDs and SQUID systems Vol. 1 (Wiley-VCH, Weinheim, 2004), Chap. 2, pp. 29–92.
[39] D. Koelle, R. Kleiner, F. Ludwig, E. Dantsker, and John Clarke, High-transition-temperature superconducting quantum interference devices, Rev. Mod. Phys. **71**, 631 (1999).
[40] E. Sassier, R. Kleiner, and D. Koelle, A spectroscopic method for excess-noise spectrum analysis (unpublished).
[41] D. J. Van Harlingen, Roger H. Koch, and John Clarke, Superconducting quantum interference device with very low magnetic flux noise energy, Appl. Phys. Lett. **41**, 197 (1982).
[42] E. M. Levenson-Falk, R. Vijay, N. Antler, and I. Siddiqi, A dispersive nanoSQUID magnetometer for ultra-low noise, high bandwidth flux detection, Supercond. Sci. Technol. **26**, 055015 (2013).
[43] From measurements on a similar device, we find an almost linear decrease in I_c with time, with an approximately 20% reduction in I_c after 40 days. This rate of degradation is typical for most of our devices. A possible explanation of this effect is outdiffusion of oxygen from the submicron GBJJs along the *a-b* plane of the YBCO thin film.
[44] G. Stan, S. B. Field, and J. M. Martinis, Critical Field for Complete Vortex Expulsion from Narrow Superconducting Strips, Phys. Rev. Lett. **92**, 097003 (2004).
[45] Frederick C. Wellstood, Cristian Urbina, and John Clarke, Low-frequency noise in dc superconducting quantum interference devices below 1 K, Appl. Phys. Lett. **50**, 772 (1987).
[46] D. Drung, J. Beyer, J.-H. Storm, M. Peters, and T. Schurig, Investigation of low-frequency excess flux noise in dc SQUIDs at mK temperatures, IEEE Trans. Appl. Supercond. **21**, 340 (2011).
[47] Roger H. Koch, David P. DiVincenzo, and John Clarke, Model for $1/f$ Flux Noise in SQUIDs and Qubits, Phys. Rev. Lett. **98**, 267003 (2007).
[48] Rogerio de Sousa, Dangling-bond spin relaxation and magnetic $1/f$ noise from the amorphous-semiconductor/oxide interface: Theory, Phys. Rev. B **76**, 245306 (2007).
[49] S. Sendelbach, D. Hover, A. Kittel, M. Mück, John M. Martinis, and R. McDermott, Magnetism in SQUIDs at Millikelvin Temperatures, Phys. Rev. Lett. **100**, 227006 (2008).
[50] M. Venkatesan, C. B. Fitzgerald, and J. M. D. Coey, Thin films: Unexpected magnetism in a dielectric oxide, Nature (London) **430**, 630 (2004).
[51] N. Pavlenko, T. Kopp, E. Y. Tsymbal, J. Mannhart, and G. A. Sawatzky, Oxygen vacancies at titanate interfaces: Two-dimensional magnetism and orbital reconstruction, Phys. Rev. B **86**, 064431 (2012).
[52] J. M. D. Coey, Ariando, and W. E. Pickett, Magnetism at the edge: New phenomena at oxide interfaces, MRS Bull. **38**, 1040 (2013).
[53] I. R. Shein and A. L. Ivanosvkii, First principle prediction of vacancy-induced magnetism in non-magnetic Perovskite $SrTiO_3$, Phys. Lett. A **371**, 155 (2007).
[54] M. Khalid, A. Setzer, M. Ziese, P. Esquinazi, D. Spemann, A. Pöppl, and E. Goering, Ubiquity of ferromagnetic signals in common diamagnetic oxide crystals, Phys. Rev. B **81**, 214414 (2010).
[55] K. Potzger, J. Osten, A. A. Levin, A. Shalimov, G. Talut, H. Reuther, S. Arpaci, D. Bürger, H. Schmidt, T. Nestler, and D. C. Meyer, Defect-induced ferromagnetism in crystalline $SrTiO_3$, J. Magn. Magn. Mater. **323**, 1551 (2011).
[56] Boris B. Straumal, Andrei A. Mazilkin, Svetlana G. Protasova, Ata A. Myatiev, Petr B. Straumal, Gisela Schütz, Peter A. van Aken, Eberhard Goering, and Brigitte Baretzky, Magnetization study of nanograined pure and Mn-doped ZnO films: Formation of a ferromagnetic grain-boundary foam, Phys. Rev. B **79**, 205206 (2009).
[57] A. Leonhardt, S. Hampel, C. Müller, I. Mönch, R. Koseva, M. Ritschel, D. Elefant, K. Biedermann, and B. Büchner, Synthesis, properties, and applications of ferromagnetic-filled carbon nanotubes, Chem. Vap. Deposition **12**, 380 (2006).

[58] K. Lipert, S. Bahr, F. Wolny, P. Atkinson, U. Weißker, T. Mühl, O. G. Schmidt, B. Büchner, and R. Klingeler, An individual iron nanowire-filled carbon nanotube probed by micro-Hall magnetometry, Appl. Phys. Lett. **97**, 212503 (2010).

[59] T. Mühl, J. Körner, S. Philippi, C. F. Reiche, A. Leonhardt, and B. Büchner, Magnetic force microscopy sensors providing in-plane and perpendicular sensitivity, Appl. Phys. Lett. **101**, 112401 (2012).

[60] J. Nagel, A. Buchter, F. Xue, O. F. Kieler, T. Weimann, J. Kohlmann, A. B. Zorin, D. Rüffer, E. Russo-Averchi, R. Huber, P. Berberich, A. Fontcubertai Morral, D. Grundler, R. Kleiner, D. Koelle, M. Poggio, and M. Kemmler, Nanoscale multifunctional sensor formed by a Ni nanotube and a scanning Nb nanoSQUID, Phys. Rev. B **88**, 064425 (2013).

[61] M. Khapaev, M. Kupriyanov, E. Goldobin, and M. Siegel, Current distribution simulation for superconducting multilayered structures, Supercond. Sci. Technol. **16**, 24 (2003).

[62] Manfred E. Schabes, Micromagnetic theory of non-uniform magnetization processes in magnetic recording particles, J. Magn. Magn. Mater. **95**, 249 (1991).

[63] A. Aharoni, Magnetization curling, Phys. Status Solidi **16**, 3 (1966).

[64] R. Skomski, *Simple Models of Magnetism* (Oxford University Press, New York, 2008).

[65] Amikam Aharoni, Angular dependence of nucleation by curling in a prolate spheroid, J. Appl. Phys. **82**, 1281 (1997).

Supplementary Information for Low-Noise $YBa_2Cu_3O_7$ NanoSQUIDs for Performing Magnetization-Reversal Measurements on Magnetic Nanoparticles

T. Schwarz,[1] R. Wölbing,[1] C. F. Reiche,[2] B. Müller,[1]
M. J. Martínez-Pérez,[1] T. Mühl,[2] B. Büchner,[2] R. Kleiner,[1] and D. Koelle[1]

[1] *Physikalisches Institut – Experimentalphysik II and Center for Collective Quantum Phenomena in LISA$^+$, Universität Tübingen, Auf der Morgenstelle 14, D-72076 Tübingen, Germany*

[2] *Leibniz Institute for Solid State and Materials Research IFW Dresden, Helmholtzstr. 20, 01069 Dresden, Germany*

(Dated: March 23, 2015)

I. CHARACTERIZATION OF SQUID-2

SQUID-2 was characterized in an electrically and magnetically shielded setup, with the sample mounted in vacuum (or in He gas) on a temperature-controlled cryostage. This enabled us to characterize electric transport and noise properties at variable temperature T, with a T stability of $\sim 1\,\mathrm{mK}$ [1].

Figure 1 shows data of electric transport properties and flux noise of SQUID-2, measured at $T = 5.3\,\mathrm{K}$. Figure 1(a) shows current-voltage-characteristics (IVCs) for modulation current $I_{\mathrm{mod}} = 0$ and two values of I_{mod}, corresponding to maximum and minimum critical current. The IVCs are slightly hysteretic with maximum critical current $I_{\mathrm{c}} = 311\,\mu\mathrm{A}$ and normal state resistance $R_{\mathrm{N}} = 2.5\,\Omega$, which yields a characteristic voltage $V_{\mathrm{c}} \equiv I_{\mathrm{c}}R_{\mathrm{N}} = 0.78\,\mathrm{mV}$. The inset of Fig. 1(a) shows the modulation of the critical current $I_{\mathrm{c}}(I_{\mathrm{mod}})$. From the modulation period, we find for the magnetic flux Φ coupled to the SQUID by I_{mod} the mutual inductance $M = \Phi/I_{\mathrm{mod}} = 0.8\,\Phi_0/\mathrm{mA} = 1.66\,\mathrm{pH}$. From resistively and capacitively shunted junction (RCSJ) simulations [2] of the $I_{\mathrm{c}}(I_{\mathrm{mod}})$ characteristics [cf. inset of Fig. 1(a)] we obtain for the screening parameter $\beta_L = 2I_0L/\Phi_0 = 0.94$ (with $I_0 = I_{\mathrm{c}}/2$), which yields a SQUID inductance $L = 6.3\,\mathrm{pH}$. We do find good agreement between the measured and simulated $I_{\mathrm{c}}(I_{\mathrm{mod}})$ characteristics if we include an inductance asymmetry $\alpha_L \equiv (L_2 - L_1)/(L_2 + L_1) = 0.83$ (L_1 and L_2 are the inductances of the two SQUID arms) and a critical current asymmetry $\alpha_I \equiv (I_{0,2} - I_{0,1})/(I_{0,2} + I_{0,1}) = 0.30$; $I_{0,1}$ and $I_{0,2}$ are the critical currents of the Josephson junctions 1 and 2, respectively, intersecting the SQUID loop. These asymmetries are caused by asymmetric biasing of the SQUID and by asymmetries of the device itself.

$V(I_{\mathrm{mod}})$ is plotted in Fig. 1(b) for different bias currents. The transfer function, i.e. the maximum value of $\partial V/\partial\Phi$, in the non-hysteretic regime is $V_\Phi \approx 1.7\,\mathrm{mV}/\Phi_0$.

Fig. 1(c) shows the rms spectral density of flux noise $S_\Phi^{1/2}(f)$ of SQUID-2. This measurement was performed open loop (in dc bias mode) with a Nb dc SQUID (at $T = 4.2\,K$) as a voltage preamplifier, i.e. in 2-stage configuration, with a $\sim 700\,\mathrm{kHz}$ bandwidth. As for SQUID-1 (see main text), we find dominating f-dependent noise, with a noise power which scales very roughly as $S_\Phi \propto 1/f$.

Figure 2 shows rms flux noise spectra of SQUID-2 mea-

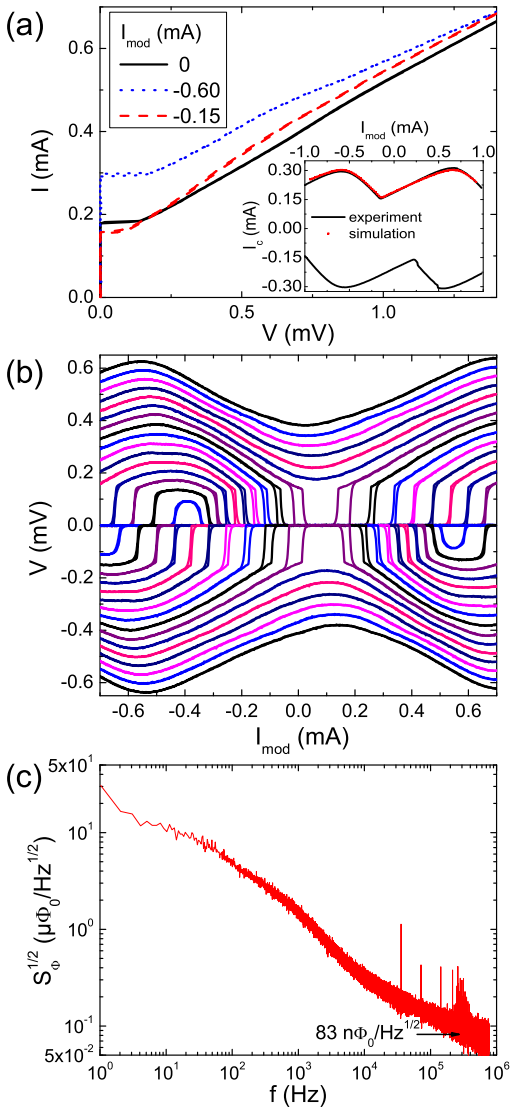

FIG. 1. Characteristics of SQUID-2 at $T = 5.3\,\mathrm{K}$. (a) IVCs for three different values of I_{mod}, including flux bias (I_{mod}) values which yield maximum and minimum critical current. Inset: measured $I_{\mathrm{c}}(I_{\mathrm{mod}})$ together with numerical simulation results. (b) $V(I_{\mathrm{mod}})$ for bias currents $|I| = 175\ldots400\,\mu\mathrm{A}$ (in $15\,\mu\mathrm{A}$ steps). (c) rms spectral density of flux noise, measured open loop (dc bias) in 2-stage configuration. Arrow indicates upper limit for measured white noise at $\sim 700\,\mathrm{kHz}$.

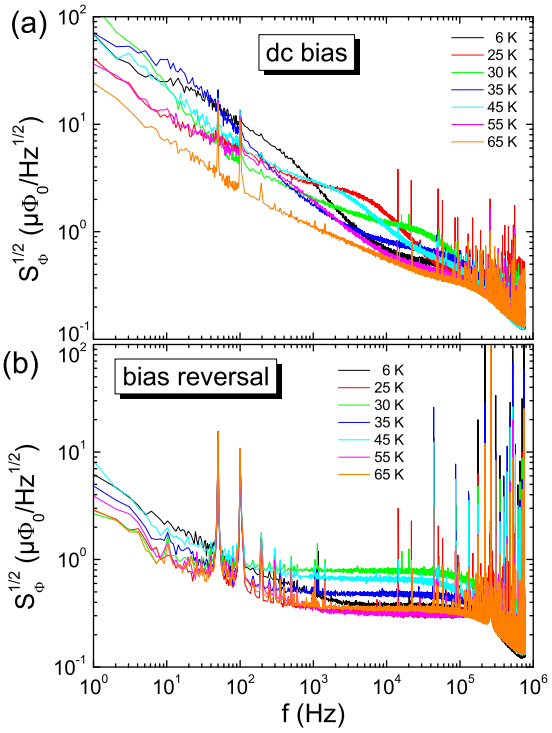

FIG. 2. rms spectral density of flux noise for SQUID-2, measured in FLL mode at different temperatures from 6 K to 65 K. (a) dc bias mode (b) bias reversal mode ($f_{\rm br} = 260\,$kHz).

sured with direct readout in flux locked loop (FLL), with $\sim 500\,$kHz bandwidth, in dc bias and bias reversal mode [3] for temperatures T ranging from 6 K to 65 K. For all data measured with dc bias [cf. Fig. 2(a)], we find f-dependent excess noise up to the cutoff frequency of the readout electronics. The flux noise S_Φ scales roughly as $1/f$, and for different T, the rms flux noise does not differ by more than about a factor of five, and does not show any systematic T-dependence.

Similar to SQUID-1 (cf. main text), in bias reversal mode [cf. Fig. 2(b)] the f-dependent excess noise above $\sim 1\,$kHz is suppressed. The remaining low-f excess flux noise observed in bias reversal mode roughly scales as $S_\Phi \propto 1/f$ for all values of T, again without any systematic T-dependence.

II. CHARACTERIZATION OF SQUID-3

Figure 3 shows electric transport and flux noise data for SQUID-3, taken in the magnetically and electrically shielded low-field setup at $T = 4.2\,$K, as described in the main text. The IVC shown in Fig. 3(a) is non-hysteretic, with $I_{\rm c} = 69\,\mu$A and $R_{\rm N} = 2.3\,\Omega$, which yields $V_{\rm c} = 0.16\,$mV. The inset shows $I_{\rm c}(I_{\rm mod})$, from which we obtain the mutual inductance $M = \Phi/I_{\rm mod} = 3.3\,\Phi_0/$mA. From the modulation depth of $I_{\rm c}(I_{\rm mod})$ we determine $\beta_L = 0.95$. With the measured $I_{\rm c}$, this yields a SQUID inductance $L = 28\,$pH. The bumps in the IVC at $V_{\rm res} \approx \pm 0.28\,$mV, can be attributed to an LC resonance. From the relation $V_{\rm res}/I_{\rm c}R_{\rm N} = (\frac{\pi}{2}\beta_C\beta_L)^{-1/2}$ [2] we determine the Stewart-McCumber parameter for the GBJJs as $\beta_C \approx 0.22$.

Figure 3(b) shows $V(I_{\rm mod})$ curves for different bias currents, yielding a transfer function $V_\Phi = 0.65\,$mV$/\Phi_0$ at the optimum bias point, at which noise spectra have been taken ($I = 54\,\mu$A). Figure 3(c) shows the rms spectral density of flux noise $S_\Phi^{1/2}(f)$ for SQUID-3, measured in direct readout FLL mode up to $f = 100\,$kHz. For comparison, the bottom trace shows the background noise

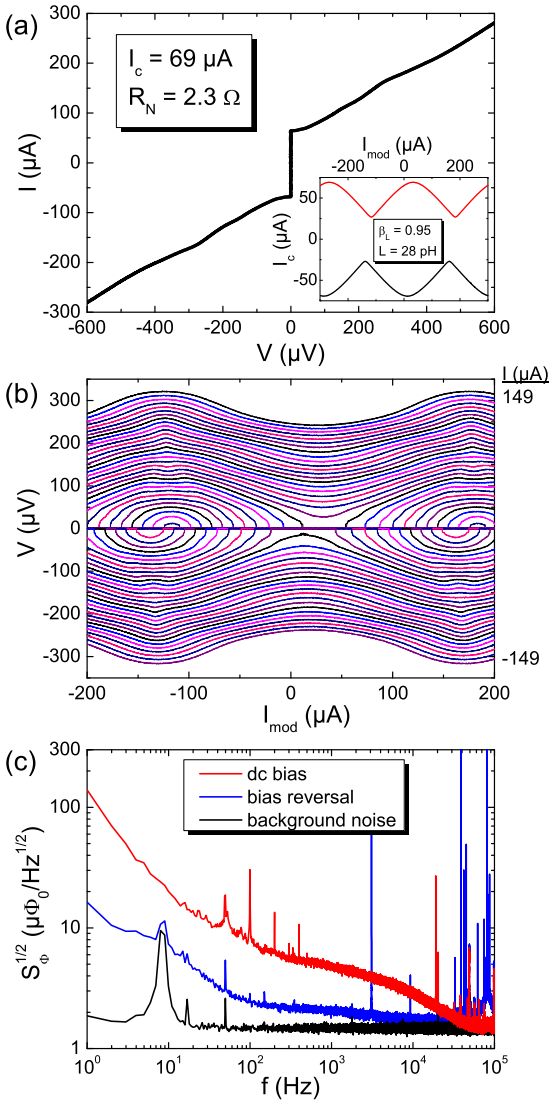

FIG. 3. Electric transport and noise characteristics of SQUID-3. (a) IVC of SQUID-3 for flux bias ($I_{\rm mod}$) which yields maximum critical current. Inset shows $I_{\rm c}(I_{\rm mod})$ curves for positive and negative current bias. (b) Voltage V vs modulation current $I_{\rm mod}$ for bias currents between $I = \pm 149\,\mu$A (step width $\Delta I \approx 4\,\mu$A). (c) Rms spectral density of flux noise measured in FLL with dc bias and bias reversal mode ($f_{\rm br} = 260\,$kHz). The lower trace shows the background noise of the readout electronics.

from the readout electronics $S_\Phi^{1/2} \approx 1.45\,\mu\Phi_0/\mathrm{Hz}^{1/2}$. For $f \lesssim 40\,\mathrm{kHz}$, we find f-dependent flux noise. For larger f, the noise is limited by the electronics background noise. Hence, we can only give an upper limit of the white rms flux noise of SQUID-3 as $S_{\Phi,\mathrm{w}}^{1/2} < 1.45\,\mu\Phi_0/\mathrm{Hz}^{1/2}$. With bias reversal (at $f_\mathrm{br} = 81\,\mathrm{kHz}$), the f-dependent excess noise is clearly reduced. Still, we obtain with decreasing f a slight increase in rms flux noise up to $\sim 2.4\,\mu\Phi_0/\mathrm{Hz}^{1/2}$ at 100 Hz. Below 100 Hz SQUID-3 shows approximately $1/f$ noise, i.e. an increase in $S_\Phi^{1/2}$ to $\sim 16\,\mu\Phi_0/\mathrm{Hz}^{1/2}$ at 1 Hz.

III. ANALYSIS OF NOISE SPECTRA OF SQUID-1

For a more detailed analysis of the measured spectral density of equivalent flux noise power $S_\Phi(f)$ for SQUID-1, we applied an algorithm [4] to decompose the noise spectra into a sum of Lorentzians $F_i(f) = F_{0,i}/[1 + (f/f_{\mathrm{c},i})^2]$ plus a $1/f^2$ spectrum $F_\mathrm{s}(f) = F_\mathrm{s}(1\,\mathrm{Hz})/(f^2/\mathrm{Hz}^2)$ (i.e. one or more Lorentzians with characteristic frequencies f_c well below 1 Hz) plus a white noise contribution F_w. This means, the measured spectra are fitted by $F(f) = F_\mathrm{w} + F_\mathrm{s} + \sum_i F_i$.

Figure 4 shows the fit $F_\mathrm{op}^{1/2}(f)$ to the spectrum measured open loop (dc bias) [cf. Fig. 3(a) in the main text]. This yields an rms white noise level $F_{\mathrm{w,op}}^{1/2} = 45\,\mathrm{n}\Phi_0/\mathrm{Hz}^{1/2}$, a 1 Hz noise $F_{\mathrm{s,op}}^{1/2} = 84\,\mu\Phi_0/\mathrm{Hz}^{1/2}$ from $F_\mathrm{s,op}$ plus 16 Lorentzians with characteristic frequencies $f_{\mathrm{c},i}$, ranging from 2.6 Hz to 2.6 MHz, and amplitudes $F_{0,i}^{1/2}$ as listed in Tab. I(a).

For comparison of the fluctuation strengths of the different fluctuators with different $f_{\mathrm{c},i}$, in Tab. I we also list $\Delta\Phi_i = F_{0,i}^{1/2} \cdot \sqrt{2\pi f_{\mathrm{c},i}}$, which yields values in the range $\sim 30 \ldots 350\,\mu\Phi_0$.

Figure 5(a) and (b) shows the fits $F_\mathrm{dc}^{1/2}(f)$ and $F_\mathrm{br}^{1/2}(f)$ to the spectra measured in FLL with dc bias and bias reversal, respectively [cf. Fig. 3(b) in the main text]. Here, we fixed the white noise contribution in dc bias mode to $F_{\mathrm{w,dc}}^{1/2} = 41\,\mathrm{n}\Phi_0/\mathrm{Hz}^{1/2}$, i.e. a value close to the one obtained for the measurement in open loop mode. The white noise contribution in bias reversal mode is determined by the noise level achieved in dc bias mode at the bias reversal frequency f_br, which yields $F_{\mathrm{w,br}}^{1/2} = 231\,\mathrm{n}\Phi_0/\mathrm{Hz}^{1/2}$. The spectrum fitted to the dc bias measurement is decomposed into 15 Lorentzians, while for the bias reversal measurement, fitting with 6 Lorentzians is sufficient. The rms noise at 1 Hz for the bias reversal spectrum is by a factor ~ 1.8 lower than the one for the dc bias spectrum. Characteristic frequencies $f_{\mathrm{c},i}$, and amplitudes of the Lorentzians are listed in Tab. I(b) for the dc bias spectrum and in Tab. I(c) for the bias reversal spectrum.

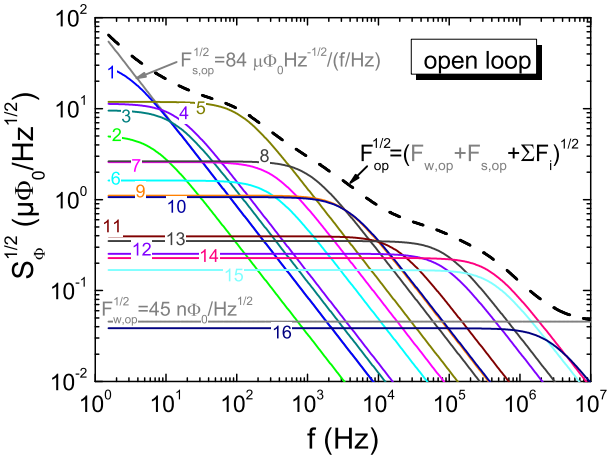

FIG. 4. Analysis of flux noise of SQUID-1: The dashed line is the fit to the noise spectrum, measured open loop (dc bias). This spectrum is the sum of the shown Lorentzians (labeled as $i = 1 \ldots 16$) plus a white noise contribution plus a $F_s \propto 1/f^2$ contribution.

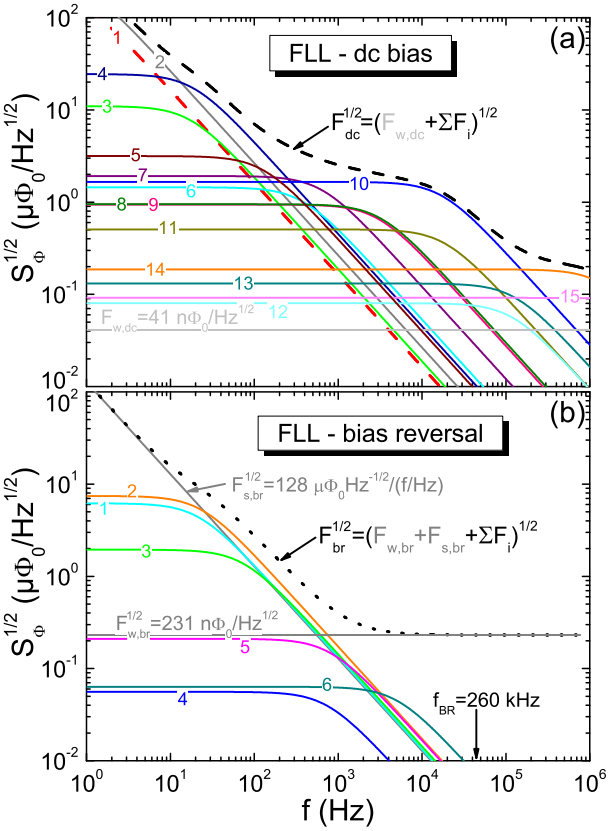

FIG. 5. Analysis of flux noise of SQUID-1: The dashed line in (a) and the dotted line in (b) are fits to the noise spectra, measured in FLL (a) with dc bias and (b) with bias reversal. Those spectra are superpositions of the shown Lorentzians [labeled as $i = 1 \ldots 11$ in (a) and $i = 1 \ldots 6$ in (b)] plus a white noise contribution plus a $F_s \propto 1/f^2$ contribution.

TABLE I. Characteristic frequencies $f_{c,i}$, rms amplitudes $F_{0,i}^{1/2}$ and flux amplitudes $\Delta\Phi_i$ of Lorentzians F_i calculated to approximate the flux noise spectra of SQUID-1, measured (a) in open loop (dc bias) [cf. Fig. 4], (b) in FLL dc bias [cf. Fig. 5(a)], and (c) in FLL bias reversal mode [cf. Fig. 5(b)].

(a) open loop

i	1	2	3	4	5	6	7	8	9	10	11	12	13	14	15	16
$f_{c,i}$ (Hz)	2.6	6.5	13	14	111	301	325	1.0 k	3.3 k	3.5 k	18 k	82 k	88 k	380 k	410 k	2.6 M
$F_{0,i}^{1/2}$ ($\mu\Phi_0/\mathrm{Hz}^{1/2}$)	33	5.1	9.6	11	12	1.6	2.6	2.6	1.1	1.1	0.40	0.25	0.35	0.23	0.17	0.038
$\Delta\Phi_i$ ($\mu\Phi_0$)	131	32	87	106	314	71	119	211	158	158	131	182	261	352	269	155

(b) FLL – dc bias

i	1	2	3	4	5	6	7	8	9	10	11	12	13	14	15
$f_{c,i}$ (Hz)	0.8	1	17	18	126	369	631	2.9 k	3.2 k	17.1 k	18.5 k	117 k	126 k	1.4 M	6.8 M
$F_{0,i}^{1/2}$ ($\mu\Phi_0/\mathrm{Hz}^{1/2}$)	206	265	11.0	24.5	3.2	1.4	1.9	0.94	0.95	1.7	0.51	0.08	0.13	0.19	0.09
$\Delta\Phi_i$ ($\mu\Phi_0$)	461	665	114	264	89	70	121	128	134	544	173	69	117	546	600

(c) FLL – bias reversal

i	1	2	3	4	5	6
$f_{c,i}$ (Hz)	21	23	74	736	794	5 k
$F_{0,i}^{1/2}$ ($\mu\Phi_0/\mathrm{Hz}^{1/2}$)	6.2	7.4	1.9	0.056	0.21	0.063
$\Delta\Phi_i$ ($\mu\Phi_0$)	72	90	42	3.8	15	11

[1] M. Kemmler, D. Bothner, K. Ilin, M. Siegel, R. Kleiner, and D. Koelle, "Suppression of dissipation in Nb thin films with triangular antidot arrays by random removal of pinning sites," Phys. Rev. B **79**, 184509 (2009).

[2] B. Chesca, R. Kleiner, and D. Koelle, "SQUID Theory," in The SQUD Handbook, Vol. 1: Fundamentals and Technology of SQUIDs and SQUID systems, edited by John Clarke and Alex I. Braginski (Wiley-VCH, Weinheim, 2004) Chap. 2, pp. 29–92.

[3] D. Drung and M. Mück, "SQUID Electronics," in The SQUD Handbook, Vol. 1: Fundamentals and Technology of SQUIDs and SQUID systems, edited by John Clarke and Alex I. Braginski (Wiley-VCH, Weinheim, 2004) Chap. 4, pp. 127–170.

[4] E. Sassier, R. Kleiner, and D. Koelle, "A spectroscopic method for excess-noise spectrum analysis," Unpublished.